Coherent Combining of Optical Pulses in Spatial, Spectral and Time Domains

by

Tong Zhou

A dissertation submitted in partial fulfillment
of the requirements for the degree of
Doctor of Philosophy
(Electrical Engineering)
in the University of Michigan
2015

Doctoral Committee:

Professor Almantas Galvanauskas, Chair
Professor Karl M. Krushelnick
Associate Research Scientist John A. Nees
Professor Herbert G. Winful

Dedicated to my parents.

ACKNOWLEDGMENTS

I would like to thank all the people who have been giving me support and love during my Ph.D. study at the University of Michigan, Ann Arbor.

First of all, I would like to express my appreciation to my advisor Professor Almantas Galvanauskas. I feel very lucky to have such a brilliant, passionate, and knowledgeable professor as my advisor. From him I have learned not only vast academic knowledge and experience, but also critical, creative, and visionary thinking. He has been always guiding and supporting me, for which I am sincerely grateful.

I also want to thank my committee members, Professor Karl M. Krushelnick, Professor Herbert G. Winful, and Associate Research Scientist John A. Nees, for all the time and effort they spend on the evaluation and suggestion of my research work, and the participation in my dissertation proposal and final defense.

I would like to express my gratitude to my colleagues and former colleagues, John Ruppe, Cheng Zhu, I-Ning Hu, Michael Haines, Leo Siiman, Wei-Zung Chang, Paul Stanfield, and Xiuquan Ma, for their teamwork and friendships.

I would like to also thank Russell Wilcox and Wim Leemans from Lawrence Berkeley National Laboratory for their collaboration on the coherent pulse stacking amplification project.

Finally, I want to express my deep gratitude to my parents, for their unconditional love and support. None of my work would have been possible without them.

TABLE OF CONTENTS

LIST OF FIGURES

ABSTRACT

Petawatt-level laser pulses have many potential applications in science and industry, but will require three orders of magnitude increase in pulse repetition rate from existing solid-state laser technology. Fiber lasers can operate at such repetition rates, but are limited in pulse energy. To overcome the gap between current achievable fiber-laser pulse energies (~mJ) and required pulse energies for high-energy applications (up to 10J), this dissertation work explores four novel techniques: (1) Coherent beam combining in the spatial domain; (2) Coherent spectral combining in spatial and spectral domains; (3) Coherent pulse stacking amplification in the time domain; (4) N-squared coherent combining in spatial and time domains.

(1) We demonstrate coherent femtosecond pulse beam combining of up to four chirped-pulse fiber amplifier channels. Theoretical and experimental analysis of combining efficiency dependence on amplitude/phase noise shows the scalability to a large number of channels.

(2) We demonstrate coherent femtosecond pulse spectral synthesis by combining three parallel fiber chirped-pulse amplifiers, each amplifying different pulse spectra. This technique simultaneously overcomes individual-amplifier energy/power limitations, and spectral gain narrowing in a single fiber amplifier.

(3) We propose and demonstrate a new technique of coherent pulse stacking (CPS) amplification, which uses reflecting resonators to transform a sequence of

phase/amplitude modulated optical pulses into a single output pulse. Experimental validation with a single resonator is demonstrated. We show theoretically that the extension to stacking a large number of equal-amplitude pulses can be achieved using multiple reflecting resonators, which enables the extraction of all stored energy in large-core fiber amplifiers.

(4) We propose and demonstrate N-squared coherent combining using resonant optical cavities, a novel pulse combining technique based on both spatial combining and temporal stacking. Its unique feature is in an N-channel system the combined pulse energy is enhanced by N-squared times.

This dissertation work provides the initial experimental and theoretical validations of several novel approaches that use coherent pulse synthesis/combining to achieve power and energy scaling using multiple small-aperture lasers, and serves as an initial step on the path towards future high average-power and petawatt peak-power laser technologies.

Chapter 1

Introduction

1.1 Background and motivation

Energetic ultrashort pulse lasers have become very powerful tools in both scientific research and industrial applications, such as eye surgery, X-ray generation, extreme ultraviolet (EUV) lithography, material processing, and particle acceleration [1,2,3,4]. Currently high-energy ultrashort optical pulses are mostly generated from conventional bulk solid-state lasers, particularly Ti:Sapphire and Nd:Glass laser systems, using the chirped pulse amplification (CPA) technique, where ultrashort optical pulses are stretched by a huge factor prior to amplification to avoid nonlinear effects, and compressed afterwards [5]. While the solid-state CPA laser systems have demonstrated extremely short (down to a few fs) pulse durations and very high pulse energies (up to kJ), their practical use is limited by the following drawbacks. First, the power scalability of these bulk solid-state lasers is significantly limited. Ti:Sapphire laser systems, for instance, even with sophisticated cryogenic-cooling systems, are limited to tens of Watts due to thermal aberrations and damage thresholds. In addition, the complexity and alignment sensitivity of the solid-state CPA laser systems hinder their practical use in situations where compact and robust ultrashort pulse lasers are needed.

Recently high power fiber lasers have emerged as a next-generation laser technology due to their advantages of power scalability, compactness, robustness, high efficiency, and excellent beam quality. While solid-state laser systems suffer from thermal-optical problems, fiber lasers exhibit excellent thermal management properties due to the large surface-to-active-volume ratio of fibers [6]. Fiber lasers are also highly efficient. For instance, Yb-doped fiber amplifiers can achieve an optical-to-optical efficiency of up to 80%. Thus high pulse energies and high average powers can be simultaneously achieved in ultrashort pulse fiber lasers. In addition, due to their alignment-free waveguide nature, fiber lasers are robust and exhibit excellent beam quality.

While high power fiber lasers have recently been demonstrated at >10 kW of average power (IPG Photonics), the achievable short pulse (sub-nanosecond regime) energies are limited to the millijoule level [7]. When pulse durations are shorter than ~10 ns, the achievable pulse energies from fiber laser amplifiers are practically limited by nonlinear effects, such as stimulated Raman scattering (SRS), stimulated Brillouin Scattering (SBS), four-wave-mixing (FWM), and self-phase modulation (SPM). This is because the mode-field-diameters (MFD) of high power fibers are on the order of a few tens of microns, and the amplifier fiber lengths are on the order of meters, which results in high-peak-intensity pulses propagating over large distances, causing the build up of nonlinear effects. However, a wide variety of energetic ultrashort pulse applications require very high pulse energies, especially in the relativistic regime. For instance, laser-driven plasma-wave electron accelerators require pulse energies on the order of 10 J in the sub-picosecond regime [4]. To overcome the big gap between the current achievable fiber laser pulse energies (millijoule level) and the required pulse energies for high energy applications

(up to tens of J), multiple amplified ultrashort optical pulses from fiber amplifiers have to be coherently synthesized. The combining of multiple amplified ultrashort pulses can be implemented in the spatial, spectral, and time domains.

1.2 Coherent beam combining in the spatial domain

In the spatial domain, the general approach to overcoming single fiber laser energy and power limitations is beam combining of an array of fiber lasers. Active coherent phasing appears best suited for combining large numbers of individual laser channels [8], and has been demonstrated with continuous-wave [9], pulsed [10], and ultrashort pulse [11] fiber lasers, with combined powers ranging from hundreds of Watts to kW and with up to millijoule energies for long and short pulses. A novel laser concept known as coherent amplification network (CAN) based on short-pulse fiber amplifiers was proposed a few years ago to achieve simultaneously extreme high pulse energies and high average powers [12,13].

In this dissertation we report on femtosecond pulse laser beam combining with up to four parallel chirped-pulse fiber amplifier channels [14,15]. Active phase locking is implemented using the LOCSET single detector feedback technique, resulting in 96.4%, 94.0%, and 93.9% relative combining efficiency with two, three, and four channels respectively. Theoretical and experimental analysis of the dependence of combining efficiency on amplitude and phase noise shows convergence to a fixed value with an increasing number of channels, indicating that multi-channel pulse combining with LOCSET feedback should be scalable to very large numbers of channels.

I was working with Leo Siiman and Wei-zung Chang on this work, and all three of us contributed equally. My work was focused more on the coherent phasing of the fiber CPA channels. Details of this coherent beam combining work are described in Chapter 2, which is based on our *Optics Express* paper "Coherent femtosecond pulse combining of multiple parallel chirped pulse fiber amplifiers" [14].

1.3 Coherent spectral combining in spatial and spectral domains

Another significant limitation on pulse energies and powers from fiber lasers is associated with spectral gain narrowing when amplifying broad band signals, such as ultrashort optical pulses. For example, although an Yb-doped fiber gain bandwidth can exceed 100 nm, chirped pulse amplification (CPA) of such a broad bandwidth pulse is not possible with a single Yb-doped fiber amplifier since gain narrowing limits the amplified spectrum to approximately 10-20 nm in high gain systems.

While in the spatial domain, individual-fiber pulse energy limitations can be overcome by combining multiple lasers or amplifiers, in the spectral domain gain spectra limitations of individual lasers can be overcome by combining two different laser gain media, as has been demonstrated by locking and coherent phasing of two individual mode-locked oscillators [16], or seeding two different gain media with a single mode-locked oscillator [17,18]. Although very short durations of only a few optical cycles have been produced, the coherent signal synthesis techniques involved in all these experiments are too cumbersome to be practical when combining more than two optical channels. Indeed, the approach in Ref. [16] requires repetition rate synchronization and phasing between individual mode-locked oscillators, the approach of Ref. [18] uses cross-correlation

between the two channels to determine phasing and delay errors, and the approach in Ref. [17] relies on a passive optical-length matching between the two channels.

In this dissertation, we demonstrate coherent spectral beam combining and femtosecond pulse spectral synthesis using three parallel fiber chirped pulse amplifiers, each amplifying different ultrashort-pulse spectra [19,20,21]. This proof-of-concept experiment opens a path to simultaneously overcome individual-amplifier energy and power limitations, as well as limitations on amplified pulse bandwidth due to the gain narrowing in a single fiber amplifier.

I was mainly working with Wei-zung Chang on this work, and both of us contributed equally. My work was focused more on the active phasing of the spectrally separated fiber CPA channels. Details of this coherent spectral combining work are described in Chapter 3, which is based on our *Optics Express* paper "Femtosecond pulse spectral synthesis in coherently-spectrally combined multi-channel fiber chirped pulse amplifiers" [19].

1.4 Coherent pulse stacking amplification in the time domain

Although the chirped pulse amplification (CPA) technique alleviates ultrashort pulse energy limitations imposed by detrimental nonlinear effects in fiber lasers by a factor of up to 10^3 - 10^4 times [5], the maximum stretched pulse duration is limited to approximately 1-2 ns by practical constraints on the compressor and stretcher grating size and cost. Thus pulse energies achievable by the CPA technique are yet much less than the stored pulse energies in fiber amplifiers [7]. For example, in Yb-doped fiber amplifiers the achievable pulse energy using CPA is smaller than the stored energy by about two

orders of magnitude using regular diffraction grating stretchers and compressors. Consequentially, achieving required pulse energies for extremely high energy applications, for instance, approximately 40 J per ultrashort pulse, as needed for a 10GeV laser-plasma acceleration stage [4], would require combining of up to 10^4 - 10^5 parallel amplification channels in a coherently phased fiber laser array. There is a significant room for improvement in achievable pulse energies per channel, provided that all stored energy in a fiber could be fully extracted.

To achieve pulse energies up to stored energies in short-pulse fiber amplifiers, one needs to amplify much longer pulses than are obtainable in a CPA approach. As a step in this direction a divided pulse amplification (DPA) technique has been proposed recently [22,23], which is based on pre-amplification spatial pulse-splitting and post-amplification pulse-recombining. However, since it requires delay lines whose lengths increase exponentially with the number of pulse division stages, DPA technique appears to be limited to a relatively small number of pulses (approximately 10). Coherent pulse stacking and dumping techniques have also been proposed recently, in which stored stacked pulses in a high-finesse resonant enhancement cavity are dumped out using an active cavity-dumping element, e.g. an acousto-optic modulator (AOM) [24], or a rotating-mirror [25]. However, this technique faces significant pulse energy limitations when an intra-cavity dumping is done with any available electro-optical or acousto-optical modulator technology, and has precision and stability constrains when the cavity dumping is to be performed using a mechanical rotating-mirror arrangement.

In this dissertation we demonstrate a new technique called coherent pulse stacking (CPS) amplification to overcome limits on achievable pulse energies from optical

amplifiers [26,27]. CPS uses reflecting resonators without active cavity-dumpers to transform a sequence of phase- and amplitude-modulated optical pulses into a single output pulse. Experimental validation with a single reflecting resonator demonstrates a near-theoretical stacked peak-power enhancement factor of ~2.5 with 92% and 97.4% efficiency for amplified nanosecond and femtosecond pulses. We also show theoretically that large numbers of equal-amplitude pulses can be stacked using sequences of multiple reflecting resonators, thus providing a new path for generating very high-energy pulses from ultrashort pulse fiber amplifier systems.

I was mainly working with John Ruppe on this work, and both of us contributed equally. Details of this coherent pulse stacking amplification work are described in Chapter 4, which is based on our *Optics Express* paper "Coherent pulse stacking amplification using low-finesse Gires-Tournois interferometers" [26].

1.5 N^2 coherent combining in spatial and time domains

As described in Section 1.4, the achievable pulse energies from short-pulse CPA fiber lasers are yet much less than the stored pulse energies in those fiber amplifiers. Thus achieving required pulse energies for extremely high energy applications would require coherent combining of a large number of parallel fiber laser amplification channels.

In this dissertation, we demonstrate a novel multidimensional pulse multiplexing technique of N^2 coherent combining that uses resonant cavity configurations to increase pulse energy extraction per each parallel amplification channel of a coherently combined array [28]. N^2 coherent combining achieves simultaneous spatial beam combining and time-domain pulse multiplexing/down-counting using traveling-wave Fabry-Perot type

resonators, thus enhancing both average power and pulse energy. Average power is increased proportionally to the number of channels N in an array, the same as in any other coherent or incoherent combining approaches. The unique aspect of N^2 combining is that it simultaneously reduces by N times pulse repetition rate in the combined beam at the system output, thus increasing the resulting energy per pulse proportionally to N^2. N^2 coherent combining enables achieving high pulse energies with relatively small number of parallel coherently-phased amplification channels, much smaller than would be required using conventional coherently combined arrays.

Details of this work are described in Chapter 5, which is based on our paper submitted to *European Physical Journal* "Resonant cavity based time-domain multiplexing techniques for coherently combined fiber laser systems" [28]. Chronologically this work was done before the work of coherent pulse stacking amplification introduced in Section 1.4.

1.6 Discussion

This dissertation work provides the initial experimental and theoretical validations of several novel approaches that use coherent pulse synthesis/combining to achieve power and energy scaling using multiple small-aperture lasers. These pulse combining techniques can be properly integrated together to further overcome current achievable pulse energy/power limitations in fiber laser systems. An example is that by combining the time-domain coherent pulse stacking technique and the spatial-domain coherent beam combining technique, extremely high energy pulses can be achieved even with a limited coherently-combined fiber amplifier array size. The coherent pulse stacking technique can enable the extraction of all stored pulse energy in a fiber amplifier, and the coherent

beam combining technique helps to further overcome single-amplifier energy limitations. The coherent stacking of a burst of <1000 pulses which are coherently combined from <100 parallel fiber amplifier channels can achieve a total pulse-energy enhancement of $<10^5$, thus enable achieving tens of J pulse energy. The integration of coherent spectral combining technique into this type of systems can further overcome the spectral gain narrowing effect.

This work serves as an initial step on the path towards future high average-power and petawatt peak-power laser technologies. While the scalabilities of all coherent pulse combining techniques in this dissertation are theoretically studied, the experimental demonstrations are carried out with only a few channels/pulses to be combined. These pulse combining techniques are not experimentally demonstrated with maximum single-laser pulse energies either. Thus, the future development of these pulse combining techniques can be carried out focusing on the experimental demonstrations with a large number of channels/pulses to be combined, and with maximum single-laser pulse energies.

1.7 References

1. Gerard A. Mourou, Toshiki Tajima, and Sergei V. Bulanov, "Optics in the relativistic regime," Rev. Mod. Phys., **78**(2), 309-371 (2006).

2. Simi A. George, Kai-Chung Hou, Kazutoshi Takenoshita, Almantas Galvanauskas, and Martin C. Richardson, "13.5 nm EUV generation from tin-doped droplets using a fiber laser," Opt. Express 15, 16348-16356 (2007).

3. Rafael R. Gattass and Eric Mazur, "Femtosecond laser micromachining in transparent materials," Nature Photonics **2**(4), 219-225 (2008).

4. Leemans, W.; Esarey, E. Laser-driven plasma-wave electron accelerators. Phys. Today 2009, 62(3), 44-49.

5. Strickland, D.; Mourou, G. Compression of amplified chirped optical pulses. Opt. Commun. 1985, 55(6), 447-449.

6. A. Tünnermann. High-power CW fiber lasers - present and future. Laser Technik Journal, 2(2), 54–56, 2005.

7. Arno Klenke, Steffen Hädrich, Tino Eidam, Jan Rothhardt, Marco Kienel, Stefan Demmler, Thomas Gottschall, Jens Limpert, and Andreas Tünnermann, "22 GW peak-power fiber chirped-pulse-amplification system," Opt. Lett. 39, 6875-6878 (2014)

8. G. D. Goodno, C. P. Asman, J. Anderegg, S. Brosnan, E. C. Cheung, D. Hammons, H. Injeyan, H. Komine, W. H. Long, M. McClellan, S. J. McNaught, S. Redmond, R. Simpson, J. Sollee, M. Weber, S. B. Weiss, and M. Wickham, "Brightness-scaling potential of actively phase-locked solid-state laser arrays," IEEE J. Sel. Top. Quantum Electron 13(3), 460–472 (2007).

9. J. Anderegg, S. Brosnan, M. Weber, H. Komine, and M. Wickham, "8-W coherently phased 4-element fiber array," Proc. SPIE, 4974, 1–6 (2003).

10. E. C. Cheung, M. Weber, and R. R. Rice, "Phase locking of a pulsed fiber amplifier," in Advanced Solid-State Photonics, OSA Technical Digest Series (CD) (Optical Society of America, 2008), paper WA2.

11. E. Seise, A. Klenke, J. Limpert, and A. Tünnermann, "Coherent addition of fiber-amplified ultrashort laser pulses," Opt. Express 18, 27827-27835 (2010).

12. G.A. Mourou, D. Hulin, and A. Galvanauskas, "The Road to High Peak Power and High Average Power Lasers: Coherent Amplification Network (CAN)," AIP Conf. Proc. 827, 152-163 (2006).

13. C. Labaune, D. Hulin, A. Galvanauskas, and G.A. Mourou, "On the feasibility of a fiber-based inertial fusion laser driver," Opt. Commun. 281, 4075-4080 (2008).

14. Leo A. Siiman, Wei-zung Chang, Tong Zhou, and Almantas Galvanauskas, "Coherent femtosecond pulse combining of multiple parallel chirped pulse fiber amplifiers," Opt. Express 20, 18097-18116 (2012).

15. L. Siiman, T. Zhou, W. Chang, and A. Galvanauskas, "Femtosecond pulses from coherently combined parallel chirped pulse fiber amplifiers," in CLEO:2011 - Laser Applications to Photonic Applications, OSA Technical Digest (CD) (Optical Society of America, 2011), paper CMD2.

16. R. K. Shelton, L. S. Ma, H. C. Kapteyn, M. M. Murnane, J. L. Hall, and J. Ye, "Phase-coherent optical pulse synthesis from separate femtosecond lasers," Science 293, 1286-1289 (2001).

17. G. Krauss, S. Lohss, T. Hanke, A. Sell, S. Eggert, R. Huber, and A. Leitenstorfer, “Synthesis of a single cycle of light with compact erbium-doped fibre technology,” Nature Photon. 4, 33-36 (2010).

18. S. W. Huang, G. Cirmi, J. Moses, K. H. Hong, S. Bhardwaj, J. R. Birge, L. J. Chen, E. Li, B. J. Eggleton, G. Cerullo, and F. X. Kartner, “High-energy pulse synthesis with sub-cycle waveform control for strong-field physics,” Nature Photon. 5, 475-479 (2011).

19. Wei-zung Chang, Tong Zhou, Leo A. Siiman, and Almantas Galvanauskas, "Femtosecond pulse spectral synthesis in coherently-spectrally combined multi-channel fiber chirped pulse amplifiers," Opt. Express 21, 3897-3910 (2013).

20. W. Chang, T. Zhou, L. Siiman, and A. Galvanauskas, "Femtosecond pulse spectral synthesis using coherently combined multi-channel fiber chirped pulse amplifiers," in Conference on Lasers and Electro-Optics 2012, OSA Technical Digest (online) (Optical Society of America, 2012), paper CW1D.4.

21. W. Chang, T. Zhou, L. Siiman, and A. Galvanauskas, "Femtosecond pulse coherent combining and spectral synthesis using four parallel chirped pulse fiber amplifiers," in Lasers, Sources, and Related Photonic Devices, OSA Technical Digest (CD) (Optical Society of America, 2012), paper AM4A.25.

22. M. Kienel, A. Klenke, T. Eidam, S. Hädrich, J. Limpert, and A. Tünnermann, “Energy scaling of femtosecond amplifiers using actively controlled divided-pulse amplification,” Opt. Lett. 39(4), 1049-1052 (2014).

23. Y. Zaouter, F. Guichard, L. Daniault, M. Hanna, F. Morin, C. Hönninger, E. Mottay, F. Druon, and P. Georges, "Femtosecond fiber chirped- and divided-pulse amplification system," Opt. Lett. 38(2), 106-108 (2013).

24. R. Jason Jones, and Jun Ye, "Femtosecond pulse amplification by coherent addition in a passive optical cavity," Opt. Lett. 27(20), 1848-1850 (2002).

25. S. Breitkopf, T. Eidam, A. Klenke, L. von Grafenstein, H. Carstens, S. Holzberger, ..., and J. Limpert, "A concept for multiterawatt fibre lasers based on coherent pulse stacking in passive cavities," Light: Science & Applications. 3(10), e211 (2014).

26. Tong Zhou, John Ruppe, Cheng Zhu, I-Ning Hu, John Nees, and Almantas Galvanauskas, "Coherent pulse stacking amplification using low-finesse Gires-Tournois interferometers," Opt. Express 23, 7442-7462 (2015).

27. T. Zhou, J. Ruppe, C. Zhu, I. Hu, J. Nees, and A. Galvanauskas, "Coherent Pulse Stacking Amplification of Nanosecond and Femtosecond Pulses," in Advanced Solid State Lasers, OSA Technical Digest (online) (Optical Society of America, 2014), paper AW4A.7.

28. Tong Zhou, John Ruppe, Paul Stanfield, John Nees, Russell Wilcox, and Almantas Galvanauskas, " Resonant cavity based time-domain multiplexing techniques for coherently combined fiber laser systems," submitted to European Physical Journal (2015).

Chapter 2

Coherent femtosecond pulse combining of multiple parallel chirped pulse fiber amplifiers (Spatial domain)

2.1 Introduction

Fiber lasers in general, and ultrashort pulse fiber lasers in particular, have demonstrated a remarkable increase in average power performance over the past decade [1, 2]. This is due to the fiber geometry, since a large surface area to volume ratio facilitates rapid heat dissipation and consequently allows for scalability to high average powers. But the tradeoff with the fiber geometry is that the optical signal is tightly confined to a relatively small transverse area over relatively long lengths. This sets limits on achieving high pulse energies in fibers because of saturation-fluence, optical damage, and nonlinear effects such as stimulated Raman scattering (SRS), stimulated Brillouin Scattering (SBS), four-wave-mixing (FWM), or self-phase modulation (SPM). Limitations on pulse energy are particularly severe for chirped-pulse amplification (CPA) of ultrashort pulses in fibers [3], where recompressed-pulse distortions caused by SPM occur at relatively low pulse energies, in the ~mJ range [4].

A general approach to overcoming single-laser energy and power limitations is to combine the outputs from an array of lasers [5]. Active coherent phasing appears best suited for combining large numbers of individual laser channels [6], and has been

demonstrated with cw [7], pulsed [8], and ultrashort pulse [9, 10] fiber lasers, with combined powers ranging from hundereds of Watts to kW and with up to millijoule energies for long and short pulses. The two key technical challenges associated with active coherent combining are (i) how to spatially combine multiple output beams, and (ii) how to temporally combine multiple beams, i.e. track and correct phasing errors in each individual channel. Multiple beams can be tiled spatially [11], thus combining only in the far-field, or can be combined into a single beam using a binary-tree type of arrangement based on either interferometric 50:50 beam splitters/combiners [12] or polarization beam splitters (PBS) [13]. A single diffraction-limited beam can also be obtained from a coherently-phased spatially-tiled beam array using diffractive-optics [14] or multi-mode interference effects in hollow-waveguides [15].

There are different strategies that can be used to track phasing errors in each individual channel. Applicability of a particular phasing approach, however, does depend on the beam combining method used. For example, one strategy is based on the spatial recognition of each channel phase in a tiled array output by using a detector array and heterodyne phase detection with respect to a reference channel [12, 16], which requires spatial monitoring of a tiled-array output. Another scheme, Hänsch-Couillaud detection, measuring deviation from linear polarization can be used to track relative phases between pairs of channels [9], but this strategy is only applicable to PBS combiners in a binary-tree type arrangement and requires a matching tree of detectors. Alternatively, each channel can be "tagged" by individual-frequency modulation which allows tracking relative phases of all the channels with a single detector [17, 18], the so-called LOCSET technique (Locking of Optical Coherence by Single-detector Electronic-frequency

Tagging). This strategy appears to be the most general approach, applicable to all spatial beam combining methods, and therefore might be the best path for phasing a large number of channels.

In this chapter we report on coherent combining of four parallel femtosecond pulse fiber amplifiers using the LOCSET phasing scheme and a binary-tree type of beam combining, and we explore the combining efficiency of such a system as a function of the number of parallel channels. Understanding the array-size scalability is crucial for the development of high power and high energy ultrashort pulse fiber laser arrays. Fundamentally, scalability of a combined-array size is determined by the effect of phase and amplitude noise on the combining efficiency. General statistical analysis indicates [19, 20] that if the phase-noise average is zero, then efficiency should converge to a fixed value at very large number of channels, but if this average is different from zero then the combining efficiency continuously degrades with increasing channel number [19]. Here we study the extrapolated performance of coherently combined systems with a very large number of parallel channels phased using LOCSET, by first developing a theoretical model, and then validating its accuracy through comparison of its predictions with the experimentally characterized performance of our combining system. Finally, we use this "calibrated" model to predict the combining performance with increasing number of channels in the presence of temporal amplitude and phase variations in each of the parallel-channel signal paths. We show that at very large number of combined channels using the LOCSET phasing arrangement, combining efficiency converges to a fixed value, determined only by the magnitude of the phase and amplitude errors.

Section 2.2 of this chapter describes the experimental system and the details of its operation. Measured performance of this coherently-combined fiber CPA array system is presented in Section 2.3. The theoretical model is given in Section 2.4, along with its experimental validation by comparing it to the measured characteristics of a coherently combined array. In Section 2.5 we analyze the coherent-combining efficiency of such an array with increasing number of channels and explore its dependence on the magnitude of phase and amplitude errors. Conclusions are given in Section 2.6.

2.2 Experiment

2.2.1 Fiber chirped pulse amplifier array

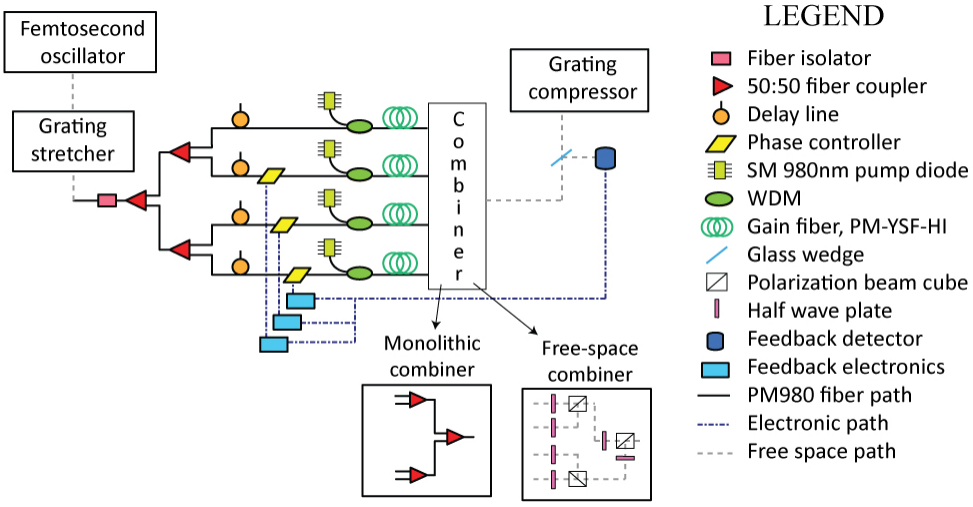

Fig. 2.1 Experimental setup for four channel monolithic fiber pulse combining.

To explore the coherent phasing of multiple parallel fiber CPA channels, we built an experimental coherently combined system based on an all-fiber, four-channel amplifier array. All fibers and fiber-optic components in the system were polarization preserving—resulting in the measured polarization extinction ratio at the output of the system to be ~20.5dB. The system layout is shown in Fig. 2.1. It consists of a mode-locked

femtosecond pulse fiber oscillator, a pulse stretcher, a parallel fiber amplifier array, a beam combiner and a pulse compressor. It also contains the control electronics for coherent phasing of the parallel fiber amplifiers.

The femtosecond oscillator is an All Normal Dispersion (ANDi) femtosecond fiber oscillator [21] producing 7 nm bandwidth pulses at 1050.5 nm central wavelength and 47 MHz repetition rate with an average output power of 30 mW. Since this is a stretched-pulse oscillator, the generated pulses are positively chirped with a pulse duration of ~15 psec. After de-chirping, the duration of these pulses is reduced to ~300 fsec. The seed pulses from the oscillator are stretched in a standard Martinez-type diffraction-grating pulse stretcher to ~900 psec. The pulse stretcher is arranged in a folded configuration (to reduce its length) and contains a single 10-cm wide grating with 1800 lines/mm groove density. The stretched pulses are coupled into single-mode polarization maintaining (PM) fiber, and then split with 50:50 single-mode fiber splitters, shown in Fig. 2.1, into four separate channels. Parallel amplification channels were built using standard single-mode PM fiber components (based on PM980 fiber for passive components), and all four channels consisted of identical components with identical fiber lengths to ensure that each optical path is of equal length and with equal amount of linear and higher-order dispersion. To achieve accurate optical-path matching each channel includes a compact adjustable delay line, described in more detail further in the text. For correcting the phase drift between the channels, three of the channels include fiber piezo-stretcher (PZT) based phase modulators. The one channel without the modulator had an equivalent length of identical passive fiber spliced into its path, to match that of a PZT stretcher. Amplification in each of the channels was implemented using standard in-core

pumped Yb-doped single-mode PM fibers (PM-YSF-HI from Nufern), WDM components for combining pump and signal paths and standard telecom-grade single-mode pump diodes. The total length of fiber in each individual channel was about 30 m.

Four parallel amplified signals at the output of the fiber array are beam combined using a binary-tree type of arrangement. In a series of experiments, we interchangeably used both bulk-component and all-fiber based beam combiners. For the bulk combiner, we used a PBS-tree arrangement to implement polarization combining [13]. The all-fiber beam combiner used a 50:50 single-mode PM fiber arrangement, which is essentially a "reverse" of the signal splitter at the array input. It is clear, however, that an all-fiber beam combiner is incompatible with high power combining or high pulse energies. The reason this monolithic arrangement was used was to achieve an accurate measurement of array-phasing performance. Indeed, in this all-fiber beam combiner, complete beam overlap between all combined signals is automatically ensured. Therefore, all the effects on the combining efficiency associated with a non-perfect spatial beam overlap [22] are eliminated, and the combining efficiency is determined solely by interferometric addition of errors between different channels, allowing very accurate measurement of the phasing effects.

A combined beam of stretched and amplified pulses was launched into a standard Treacy-type diffraction grating compressor. Just like the stretcher, the compressor was arranged in a folded configuration, and therefore, uses only a single diffraction grating, identical in specifications to the one used in the stretcher. Compressor throughput efficiency was approximately 65%. A small fraction of the output power is "sampled" by either a glass wedge placed prior to the compressor, or alternatively, by zero-order

reflection from the compressor grating. The “sampled” beam is directed onto a single detector to provide a feedback signal for active phase locking. Without phase locking (i.e. free running operation / open control loop) the relative phases between channels drift, resulting in random output power fluctuations after the combiner. This is of course expected, since without phase control, time-varying random constructive or destructive interference occurs between the channels. Using a feedback loop set to maximize the output power forces the channels to interfere constructively. The feedback signal contains the phase error information for each of the three of the channels with PZT modulators (the phase error is with respect to the fourth, i.e. reference, channel). The phase error signals are individually extracted with three separate feedback electronic signal processing units and the appropriate error canceling signals sent to the phase controllers, using the so-called LOCSET scheme, described in more detail further in the text.

2.2.2 Equalization of parallel-channel optical paths

Coherent combining of ultrashort optical pulses requires not only robust phasing, but also accurate matching of the group delays between parallel channels, so that the combined pulses are exactly overlapped in time. Errors in timing cause both pulse distortions and a loss in combining efficiency. In practice, acceptable group-delay errors should be much smaller than the pulse duration, and for femtosecond pulses should be on the order of few micrometers. Achieving such fiber-length accuracy by simply cutting the fiber is not practical. Instead, an arrangement for adjustable fiber length control should be used. Implementing adjustable length control in an array consisting of a large number of parallel channels has to be compact and cost-effective to manufacture. With this practical constraint in mind, we demonstrate an adjustable and compact delay line built using

standard single-mode fiber based micro-optical components. The schematic of this arrangement and its 3D rendering is shown in Fig. 2.2. The adjustable delay line exploits the non-reciprocal nature of a fiber circulator. An input pulse is sent into port 1 of a fiber circulator, it then travels out of port 2 with a spliced-on fiber collimator, and in free space propagates over a variable length (i.e. the delay) before being retro-reflected back into port 2 with a micro-optic mirror. Adjustment of the double-pass delay in this arrangement has been achieved with a compact micro-optical linear translation stage. After coupling back through the collimator into the single-mode fiber of port 2 the delayed pulse passes the circulator the second time and due to the circulator non-reciprocity is directed out of port 3. This configuration was selected since it minimizes the number of free-space degrees of freedom need for signal back-coupling adjustment—only two angular adjustments of only the reflecting mirror are needed. The insertion loss of this delay line is approximately 6 dB.

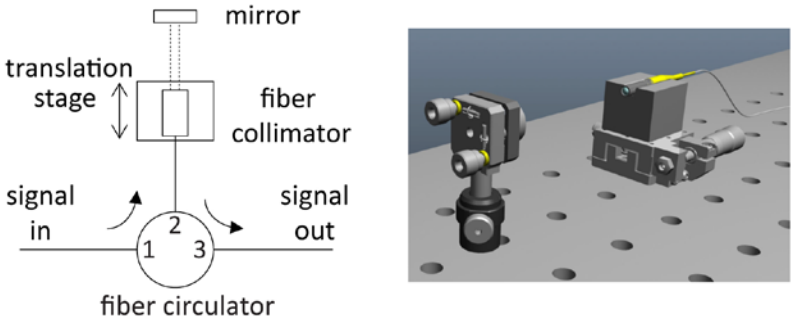

Fig. 2.2 Schematic and 3D rendering of the micro-optic delay line.

During combining experiments, we observed that it was very important to match dispersions of the parallel channels. A four-channel array needs only three adjustable delay lines to achieve complete equalization between all four channels. Therefore, in an early implementation of our four channel combining setup we did not include a fiber

circulator delay line in one of the channels (reference channel four). But each circulator introduces significant dispersion, which led to the unbalanced dispersion in the reference channel, and subsequently, inefficient combining of this channel with the other three. This inefficiency was completely eliminated after an identical circulator-based delay line was incorporated in the reference channel to equalize the dispersions between all four channels.

2.2.3 Channel active-phasing control system

As stated earlier, the four-channel fiber CPA array setup was actively phased using a LOCSET approach. The optical phase in three of the channels was controlled using fiber piezo-stretchers. The fourth channel was left as a reference for the phase controlled channels to match. The piezo-stretcher gives a π phase shift per 2.6 V of drive voltage. The maximum voltage range of the device is ±500 V and therefore supports up to 384π of continuous phase control. The feedback-control electronics was limited to an output of ±5 V and a high-voltage amplifier chips was used at its output to reach at least ±100 V (76π) driving voltages. Using only the limited ±5 V (3.8π) range would result in temporary, on average once every ~30 sec, instances of unlocked operation lasting less than ~200 msec before the system relocked to a modulo 2π phase. The extended phase control range with the 100V high voltage amplifiers eliminated these temporary unlocks and resulted in robust locking that we tested from several minutes to one hour.

In the self-referenced LOCSET technique for active coherent beam combining, a single detector is used to supply a feedback signal to each of the feedback electronic units [18]. The principle of this technique is to modulate each phase controlled channel with a unique radio frequency (RF) value. One channel remains unmodulated. The modulated

channels are then phase controlled to track the phase of the unmodulated channel. A single detector measures a photocurrent that includes a superposition of all the interference effects between the channels. Demodulation of this photocurrent by feedback electronic signal processing units is performed for each modulated channel. Since the channels have different RF modulations the demodulation can be tuned to isolate the error signal for just a particular channel. The result of the LOCSET scheme is an RF phase locked loop that stabilizes the phases of the modulated channels with respect to the unmodulated channel.

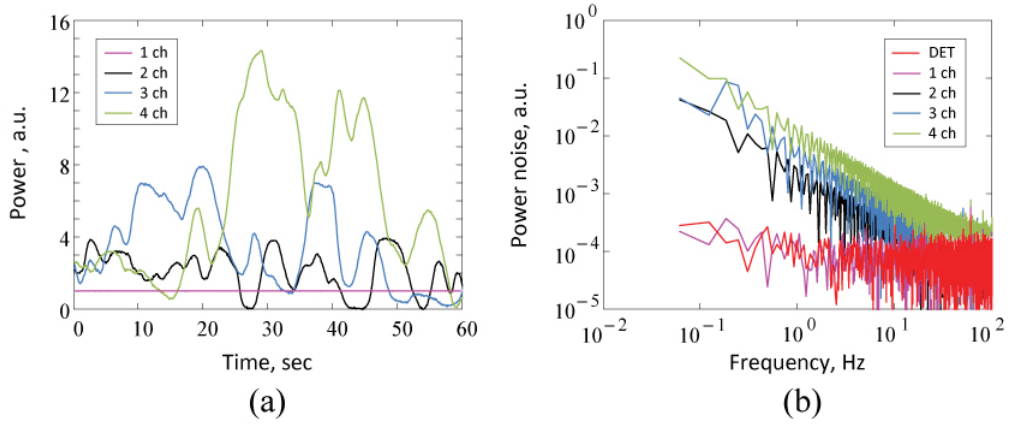

Fig. 2.3 Power noise in the unlocked state for one, two, three, and four channels: (a) time domain, (b) frequency domain. The DET data indicates our detector noise floor.

The choice of values for RF modulation depends on how quickly the phase of a channel fluctuates. To determine the appropriate RF values, we first monitored the interferometric power fluctuations from the channels without feedback control (i.e. in the free running state, open control loop). In this case, the interference varies randomly over time and gives an indication of the phase noise. Figure 2.3 shows measurements of the fluctuating power in both the time (a) and frequency (b) domains. The frequency domain data was obtained by taking a ten second interval of data at 1 kHz sampling rate,

subtracting out the mean, and then performing a Fast Fourier Transform. The DET data shows the measured detector noise when there is no optical power on the detector.

Fig. 2.3 (a) shows that without phase-locking parallel-channel outputs would interfere randomly, producing random power drifts and fluctuations, corresponding to the sources of noise associated with acoustic vibrations and temperature drifts. Experiments with cw fiber laser combining also confirm that noise is dominated by frequencies below 100 Hz [23, 24]. We determined that RF modulation frequencies in the kilohertz range are sufficiently within the low-noise regime of our environment. In our multi-channel experiments, the modulation frequencies were set to 5 kHz, 6 kHz, and 7.5 kHz. The integration time of the feedback electronics was set to 50 msec. This allowed the phase control loop to cancel phase disturbances up to 20 Hz in frequency. Detailed circuit diagrams and the values of circuit components are shown in Appendix C.

2.3 Measured performance of the coherently-combined fiber CPA array

2.3.1 Combined pulses

An important performance metric for a multi-channel ultrashort-pulse combining system is the combined-pulse quality, compared to individual-channel pulses. The measured spectra and autocorrelation traces of the combined and individual channel pulses are shown in Fig. 2.4. In this figure both spectral and autocorrelation traces from individual channels and of the combined signal overlap with each other very accurately, clearly indicating the complete absence of spectral and temporal distortions due to the coherent phasing. For reference, a calculated bandwidth-limited pulse autocorrelation trace is

shown as a dashed line in Fig. 2.4(b) (it was calculated by taking Fourier-transform of the spectra in Fig. 2.4(a)). Autocorrelation-trace wings of the measured pulses that are appearing relative to the "ideal" bandwidth-limited trace, indicate the presence of some residual third-order dispersion in the system, most likely due to imperfect alignment between the diffraction-grating stretcher and compressor. Deconvolving the measured autocorrelation traces of the four channel combined pulse with a calculated pulse shape factor gives a pulse duration of 524 fsec. This is slightly longer than the bandwidth-limited 410 fsec duration. A deconvolution factor of ~1.4 for relating the measured autocorrelation trace to the actual pulse duration was estimated by calculating the bandwidth-limited pulse and its autocorrelation from the measured pulse spectrum. We should remark that when the system is unlocked the autocorrelation trace of the combined signal fluctuates in magnitude but not in shape.

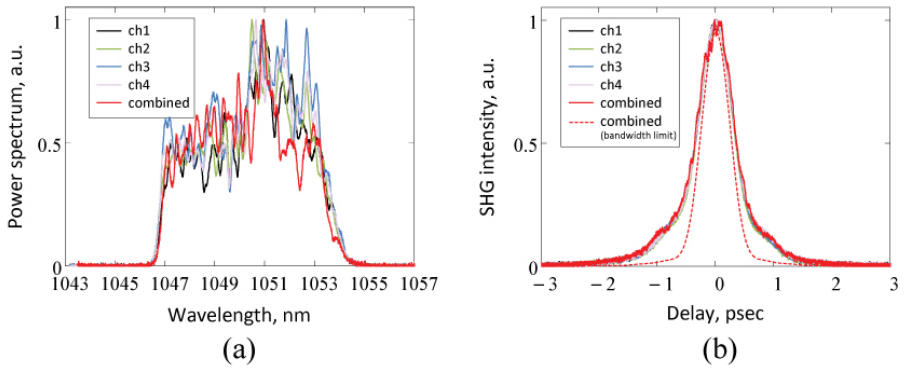

Fig. 2.4 Pulse quality results: (a) normalized spectrum of individual channels and all four channels combined, (b) normalized autocorrelation traces of individual channels and all four channels combined – the dashed line shows the calculated (from the spectral measurement) bandwidth limited autocorrelation of the combined pulse.

2.3.2 Combining efficiency

Since the primary reason for using laser beam combining is power scaling, combining efficiency is one of the key performance metrics when characterizing coherently

combined laser arrays. Our objective here was to perform very accurate efficiency measurements with the experimental 4-channel fiber CPA array and then to use these results to extrapolate performance for very large arrays. In this regard it is very useful to distinguish between "internal" effects on combining efficiency associated with a variety of laser-array signal errors such as phase errors, power fluctuations, incorrect balance between different-channel output powers, etc., and the "external" effect directly associated with the beam-combiner loss. The latter depends on a specific type, design and quality of a beam-combining element used in the system and does not depend on the performance of the fiber-laser array itself. Here we are primarily concerned with the "intrinsic" effects that characterize fundamental limitations on array combining efficiency. In order to distinguish between these "internal" and "external" effects experimentally, we used the notion of *absolute* and *relative* combining efficiencies, η_{abs} and $\eta_{relative}$ respectively, as well as the *combiner* efficiency $\eta_{combiner}$. Absolute combining efficiency is simply a ratio between the combined output power and the sum of all the individual powers from all the channels at the input of the combining element. Combiner efficiency characterizes cumulative power transmission/loss from all the channels in the combining element, and "internal" effects are characterized by the relative combining efficiency $\eta_{relative}$. All three different efficiencies are related through $\eta_{abs} = \eta_{combiner} \cdot \eta_{relative}$.

While it is straightforward to measure absolute combining efficiency, the question arises of how to measure the relative efficiency, particularly in an all-integrated system. As it turns out a convenient and rigorous measurement procedure exists to determine the magnitude of $\eta_{relative}$ accurately. Mathematical derivation of this procedure for a general

case of N signals combined with a binary-tree beam type combiner is given in Appendix A. This procedure requires measurement of the power only at the output of the system, and does not require any measurements *before* the beam combiner. The procedure consists of measuring the coherently-combined power P^{comb} when all the channels are seeded and pumped and phase-locking is turned-on, and then measuring each power P_k^{out} transmitted through the combiner from each k-th channel individually, when signals from all other channels $m \neq k$ are blocked (e.g. by turning-off the pump diodes and blocking signal paths in the corresponding delay lines for all channels $m \neq k$). Then a relative combining efficiency of N coherently-phased channels is given by (Appendix A).

$$\eta_{relative} = \frac{P^{comb}}{\left(\sum_{k=1,N}\sqrt{P_k^{out}}\right)^2}. \tag{1}$$

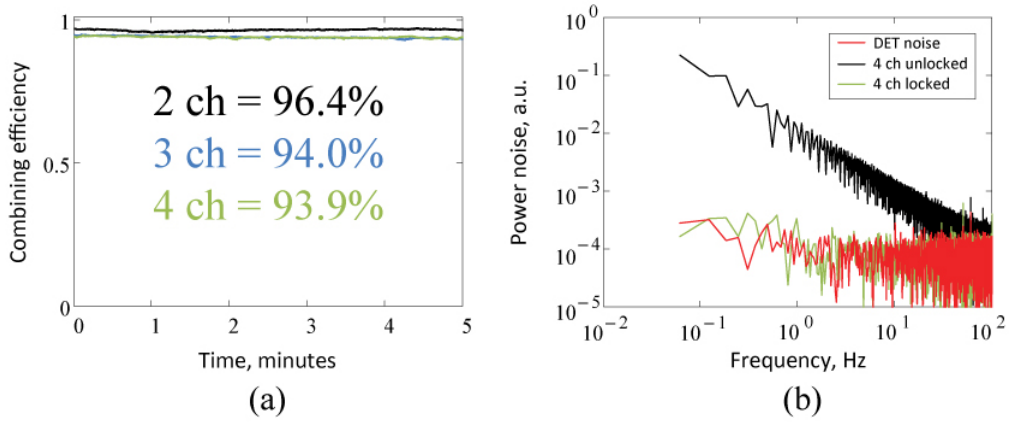

Fig. 2.5 Combining efficiency and power noise: (a) combining efficiency for two, three, and four channel locking over a five minute time period, (b) four channel locked and unlocked noise.

Figure 2.5(a) shows the relative combining efficiency for two, three, and four channels with monolithic 50:50 PM fiber coupler combiners over a time period of five minutes. The mean efficiency is 96.4%, 94.0%, and 93.9% for two, three, and four channel

combining respectively. Even though different combinations of channels can be used for two and three channel combining, the results are within 1% of each other.

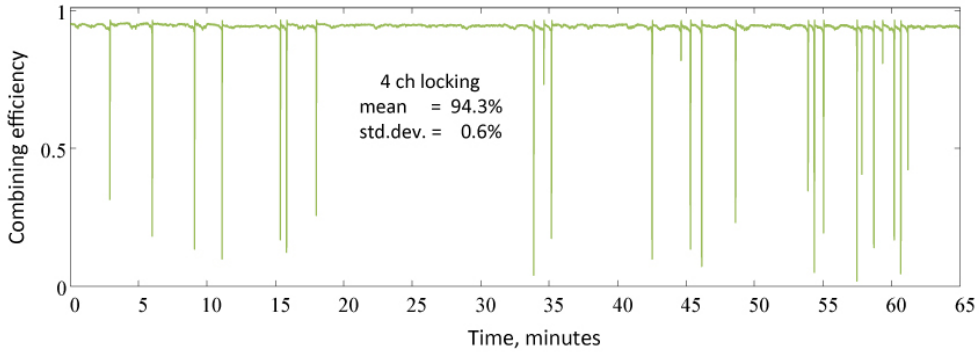

Fig. 2.6 Four channel combining efficiency with feedback blocks. The momentary drop-outs in the combined signal are due to intentional interruptions to demonstrate system robustness and its reaction to abrupt external interruptions in system operation.

Measured output powers for two, three, and four channel combining were 15.2 mW, 33.2 mW, and 58.6 mW respectively. We note that the output power from the combining system was kept safely below the 300 mW damage threshold of the 50:50 PM fiber couplers. We also note that each fiber coupler has an insertion loss of -1.2 dB, resulting in -1.2 dB combiner loss for the two-channel system and -2.4 dB loss in the three-channel and four-channel systems (two stages of 50:50 couplers). The combiner loss contributes to reducing the absolute combining efficiency. In separate experiments with free-space PBS based combiners instead of monolithic combiners, absolute efficiency in the four-channel system was 85%. Observing the electronic error signals on an oscilloscope indicated that the channel phase errors drifted over a range of less than 20π over time. Figure 2.5(b) compares the power noise of the locked four channel result with the previous, Fig. 2.3(b), unlocked four channel measurement. We see that at the frequencies measured, the locked result is within the measurement floor of our detector. Fig. 2.6 shows that the four channel combining is robust over a longer period of time, even when

we occasionally block the signal to the feedback detector. Without feedback the system drifts, but immediately recovers when the feedback signal is restored. These intentional feedback 'blocks' lasted for less than one second and show that the combining efficiency re-stabilizes due to electronic feedback system.

2.4 Experimental validation of the theoretical combining-efficiency model

In the LOCSET method of active phase control, a small phase modulation is purposely applied to each of the phase controlled channels. The electric field of a phase controlled channel varies as $\cos(\omega_L t + \phi + \beta \sin(\omega_{RF} t))$, where ω_L is the laser frequency, ϕ is an initial phase, ω_{RF} is an RF modulation frequency, and β is the phase modulation amplitude. From this expression it is apparent that this phase modulation should affect combining efficiency similarly to the random variation of the signal phase ϕ. Consequently, this allows validating experimentally the theoretical prediction of the combining efficiency as a function of the phase-variation magnitude, by measuring combining efficiency as a function of the phase modulation amplitude β. Additionally, this analysis allows to determine the effect of the finite amplitude β in the LOCSET scheme on the overall combining efficiency at large channel numbers.

Analytically, the LOCSET scheme combining efficiency as a function of modulation amplitude β is (see Appendix B)

$$\eta_{relative}(\beta) = \frac{\sum_{k=1}^{N} P_k^{out} + \sum_{k=2}^{N} 2\sqrt{P_1^{out} P_k^{out}}\, J_0(\beta) + \sum_{k=2}^{N} \sum_{\substack{m=2, \\ m \neq k}}^{N} \sqrt{P_m^{out} P_k^{out}}\, J_0{}^2(\beta)}{\left(\sum_{k=1}^{N} \sqrt{P_k^{out}} \right)^2}, \qquad (2)$$

where J_0 is a Bessel function of order zero of the first kind and P_i^{out} is the individual output power from channel i. Fig. 2.7(a) compares the theoretical combining efficiency given by Eq. (2) to experimentally measured values of combining efficiency at different phase modulation amplitudes. Results are given for two, three, and four channel combining. We see that the experimental efficiency follows the theoretical prediction quite closely, thus providing with the experimental validation of the combining-efficiency calculation. Additionally, this result indicates that, since it is therefore desirable to operate at the smallest phase modulation amplitude that supports stable locking, in our system the minimum usable modulation appears to be $\beta \approx 0.25$. Other electronic implementations of LOCSET feedback control have demonstrated stable locking of cw fiber lasers at $\beta = 0.10$ [17].

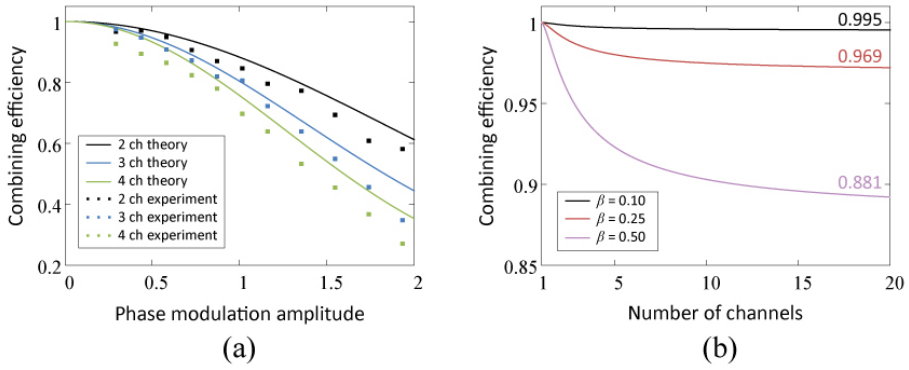

Fig. 2.7 Effect of phase modulation on the combining efficiency: (a) experimental and theoretical combining efficiency as a function of phase modulation amplitude, (b) theoretical combining efficiency as a function of number of channels for different values of phase modulation amplitude.

For a fixed β value, the theoretical combining efficiency given by Eq. (2) is plotted in Fig. 2.7(b) as a function of the number of channels under the assumption that all individual channel powers are equal. Fig. 2.7(b) shows the dependence on channel number for three different β values. What is noteworthy is that the efficiency converges

to a stable value as the number of channels is increased. In fact, by taking the limit of Eq. (2) as N goes to ∞ we get $\eta_{relative}(\beta) = J_0^{\,2}(\beta)$. At $\beta = 0.25$ the theoretical efficiency converges to 96.9%. This result indicates that the effect of the LOCSET phase modulation on the overall combining efficiency can be negligibly small.

2.5 Coherent combining of large fiber arrays

Since the experimental validation given above shows a good agreement between the measured and calculated combining efficiency as a function of phase-modulation magnitude, one can use this to extrapolate this result to larger numbers of combined channels and to evaluate achievable combining efficiencies at large combined array sizes. For this it is necessary to generalize Eq. (2) to the case of unequal phases between different channels. The combining efficiency then is given by

$$\eta_{relative} = \frac{\sum_{k=1}^{N} P_k^{out} + \sum_{k=2}^{N} 2\sqrt{P_1^{out} P_k^{out}}\cos(\phi_k - \phi_1)\, J_0(\beta) + \sum_{k=2}^{N}\sum_{\substack{m=2,\\ m\neq k}}^{N}\sqrt{P_m^{out} P_k^{out}}\cos(\phi_k - \phi_m)\, J_0^{\,2}(\beta)}{\left(\sum_{k=1}^{N}\sqrt{P_k^{out}}\right)^2}. \quad (3)$$

To analyze Eq. (3) statistically, we make the assumption that the channel powers P_i^{out} are independent Gaussian random variables with mean P_{avg}^{out} and standard deviation σ_P, and that the phases ϕ_i are independent Gaussian random variables with zero mean and standard deviation σ_ϕ. For these random variables, the following expressions for expected value are useful in simplifying Eq (3): $E\{\cos(\phi_i - \phi_j)\} = \exp(-\sigma_\phi^{\,2})$ and $E\{\sqrt{P_i^{out} P_j^{out}}\} \cong P_{avg}^{out}[\,1 - \frac{1}{8}(\sigma_P / P_{avg}^{out})^2 - \frac{3}{16}(\sigma_P / P_{avg}^{out})^4\,]^2$. The expected value of Eq (3) is

$$< \eta_{relative} > = \frac{N + \left[1 - \frac{1}{8}\left(\frac{\sigma_P}{P_{avg}^{out}}\right)^2 - \frac{3}{16}\left(\frac{\sigma_P}{P_{avg}^{out}}\right)^4\right]^2 e^{-\sigma_\phi^2} J_0(\beta)\left[2(N-1) + (N-1)(N-2)\,J_0(\beta)\right]}{N^2}. \quad (4)$$

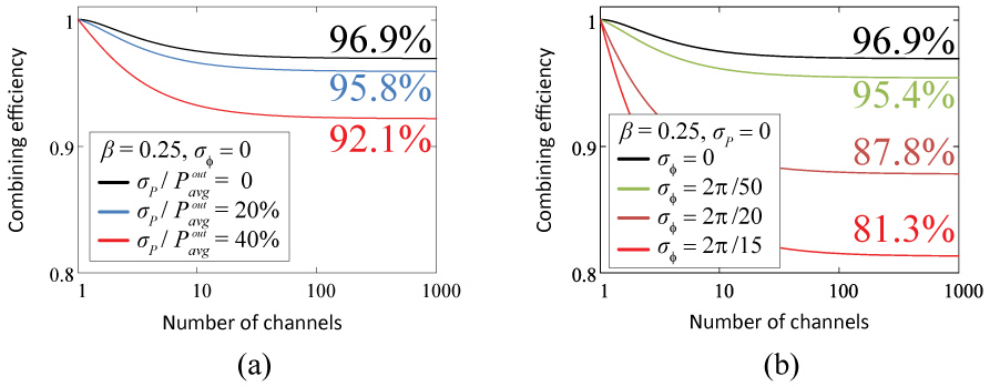

Fig. 2.8 Scalability of a multi-channel combining system with LOCSET locking at β = 0.25 and different magnitudes of errors: (a) only power variation errors, (b) only temporal phase errors.

With Eq. (4) we have a formula for combining efficiency in terms of the variables N, σ_P / P_{avg}^{out}, σ_ϕ, and β. For calculations, we assume that locking occurs at $\beta = 0.25$ (the value we currently are able to achieve stable locking). Fig. 2.8 plots Eq. (4) versus number of channels for different power variations σ_P and different phase errors σ_ϕ. The important result is that in both cases the efficiency converges to a fixed value for very large number of channels, thus indicating that LOCSET based coherently combined systems should scale gracefully with array size. The efficiency value towards which the large array converges depends on the magnitude of the phase and amplitude noise amplitudes. Results in Fig. 2.8(b) indicate that for phase-errors smaller than ~λ/20 the combining efficiency should exceed 90%. Fig. 2.8(a) indicates that combining efficiency is quite insensitive to amplitude noise in the channels. Indeed, even for large amplitude noise of ~20% the predicted combining efficiency exceeds 95%. Explanation of such convergence

of combining efficiency at large channel numbers should be generally associated with the fact that combined power increases linearly with the number of channels, while the total noise increases only proportionally to the square-root of the number of channels, thus leading to decrease in single-to-noise ratio with increasing array size.

We also explored how this convergence-efficiency depends on the magnitude of the phase and amplitude errors assuming very large combined array sizes (i.e. when $N \rightarrow \infty$). Results are plotted in Fig. 2.9. Fig. 2.9(a) indicates again that efficiency dependence on the amplitude noise is relatively weak, compared to the phase noise effect, which is plotted in Fig. 2.9(b). From the latter figure one can conclude that, remarkably, achieving combining efficiency of >90% requires relatively modest phasing accuracy of > λ/20. Note also that when combining efficiency degrades to zero for large phasing errors in Fig. 2.9(b), the array-output power simply is dissipated through all the intermediate binary-tree output ports, not the single combined-output port.

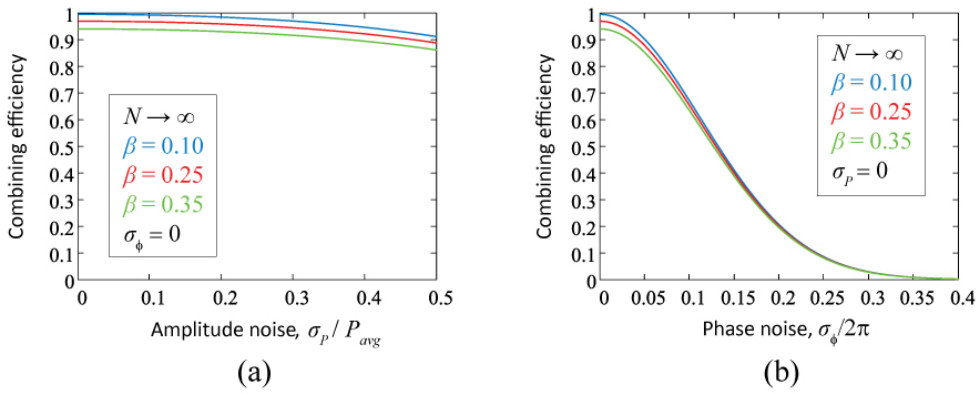

Fig. 2.9 Combining efficiency for very large arrays as a function of power and phase noise magnitude: (a) combining efficiency as a function of amplitude noise only, and (b) of phase noise only.

It is also important to note that this scalability analysis is limited to zeroth-order phase errors in the time domain (recall that the electric field in Eq. (B1) is written only with

time as a variable). For our monolithically integrated combining system it is appropriate to neglect spatial errors since the waveguide geometry automatically overlaps Gaussian spatial modes of different channels. But high power systems must use free-space combining arrangements. For a filled-aperture architecture, the possibilities include using polarization beam splitters [13], a diffractive optical element [14], or a hollow-core waveguide [15]. In these cases, spatial errors, particularly wavefront errors, might have a dominant effect on reducing the combining efficiency [22].

2.6 Conclusion

We have demonstrated a multi-channel fiber femtosecond pulse combining system with 96.4%, 94.0%, and 93.9% relative combining efficiencies for two, three, and four channels respectively. The combined and compressed ~500fs pulses have identical shape to the compressed pulses from individual channels, indicating that pulse quality is preserved in a multi-channel pulse combining system. Furthermore, we established convenient experimental and theoretical metrics for characterizing combined system performance due to phase and amplitude errors in the parallel-channel array. It is based on a notion of relative combining efficiency, which can be experimentally determined using a straightforward measurement procedure. Inherent advantage of this "figure of merit" is that it directly relates to the efficiency of the combined array, and can be easily calculated and measured. Although this metric was rigorously developed for a binary-tree type of combiner, it should be directly applicable to other types of beam combiners (e.g. holographic beam combiners).

Our analysis of combining efficiency dependence on amplitude and phase errors shows that LOCSET feedback based combining systems should scale gracefully to very large

numbers of channels. Although our interest here was primarily associated with ultrashort-pulse combining, these conclusions are of general nature and could be equally well applied to cw and pulsed systems. Of course, a full description of ultrashort-pulse combining scalability should also include consideration of pulse-dispersion effects. However, our experiment indicates if all the channels are identical these dispersion effects can be cancelled out, at least in the low-nonlinearity case. For analysis quantifying specific short pulse-related effects on coherent combining efficiency see [25] for a theoretical approach and [26] for an experimental approach. Coherent combining of femtosecond pulses in multi-channel parallel fiber CPA systems offers a possible path towards simultaneously generating high energy and high average power ultrashort laser pulses.

2.7 Appendix A: Coherent-combining efficiency using binary-tree type combiners

First let's consider combining efficiency with a single two-port combiner. Combining efficiency in general depends on

1) Relationship between combiner splitting ratio X and the ratio between input beam powers (or powers) X'.

2) Combiner loss for each of the two inputs η_1 (for input P_1^{in}) and η_2 (for input P_2^{in}).

3) Phase difference $\Delta\varphi$ between the two beams.

If there is only a single input beam into the combiner then each input beam P_1^{in} and P_2^{in} will be partially transmitted and partially reflected, as shown in Fig. 2.10, i.e. beam combiner acts as a beam splitter. We can always choose one direction as a combiner

output, for example as selected in the Fig. 2.10. Then P_1^{out} and P_2^{out} denotes beam splitter output powers when only either P_1^{in} or P_2^{in} input beam is present, respectively.

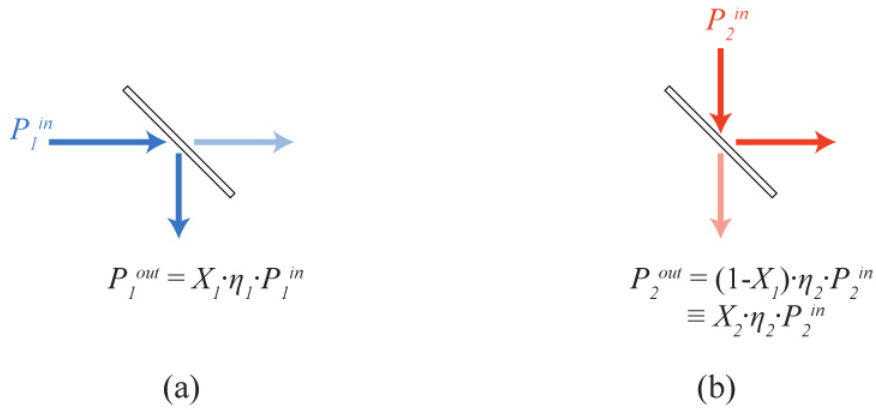

Fig. 2.10 Beam splitter: (a) when only beam P1 is present, (b) when only beam P2 is present.

When both input beams P_1^{in} and P_2^{in} are present and their relative phases are fixed (i.e. they are phased with each other) the same device acts as an interferometric beam-combiner, as shown in Fig. 2.11. Combined power P^{comb} is found by direct calculation:

$$\begin{aligned} P^{comb} &= c\varepsilon_0 nA \cdot \left\langle \left(E_1^{out} \cdot \cos(\omega t + \phi_1) + E_2^{out} \cdot \cos(\omega t + \phi_2) \right)^2 \right\rangle \\ &= P_1^{out} + P_2^{out} + 2\sqrt{P_1^{out} \cdot P_2^{out}} \cdot \cos\Delta\phi. \end{aligned} \tag{A1}$$

Here brackets $\langle ... \rangle$ denotes time average, and output power is related to the corresponding field amplitude as $P_i^{out} = c\varepsilon_0 nA \cdot \left(E_i^{out}\right)^2 / 2$, where A is beam area. The maximum constructive interference occurs when both beams are in phase, i.e. $\Delta\phi = (\phi_1 - \phi_2) = 0$, producing the in-phase combined power:

$$P^{comb\_in-phase} = P_1^{out} + P_2^{out} + 2\sqrt{P_1^{out} \cdot P_2^{out}} = \left(\sqrt{P_1^{out}} + \sqrt{P_2^{out}} \right)^2. \tag{A2}$$

Let's denote $P_1' = \eta_1 \cdot P_1^{in}$, $P_2' = \eta_2 \cdot P_2^{in}$, and $P_{tot}' = P_1' + P_2'$. It can be shown that the maximum combining efficiency is achieved when

$$P_1^{/} = X_1 \cdot P_{tot}^{/}. \tag{A3}$$

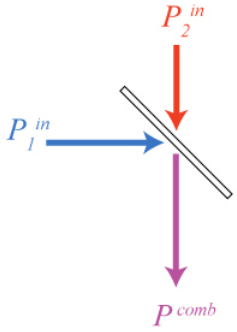

Fig. 2.11 Beam combiner

It is straightforward to show that in this case it is also $P_2^{/} = X_2 \cdot P_{tot}^{/} = (1 - X_1) \cdot P_{tot}^{/}$. It is more convenient to express this condition for achieving the maximum combining efficiency as

$$\frac{P_1^{in}}{P_2^{in}} = \frac{X_1 \cdot \eta_2}{X_2 \cdot \eta_1} = \frac{X_1 \cdot \eta_2}{(1 - X_1) \cdot \eta_1}. \tag{A4}$$

Since $P_1^{out} = X_1 \cdot P_1^{/}$ and $P_2^{out} = X_2 \cdot P_2^{/} = (1 - X_1) \cdot P_2^{/}$ then substituting the condition for the maximum combining efficiency into Eq. (A2) leads to the expression for the maximum achievable combined power:

$$\begin{aligned} P^{comb\_MAX} &= \left(\sqrt{P_1^{out}} + \sqrt{P_2^{out}} \right)^2 \\ &= \left(X_1 \cdot \sqrt{P_{tot}^{/}} + (1 - X_1) \cdot \sqrt{P_{tot}^{/}} \right)^2 \\ &= P_{tot}^{/} = \eta_1 \cdot P_1^{in} + \eta_2 \cdot P_2^{in}. \end{aligned} \tag{A5}$$

This combining efficiency is achieved when both inputs are perfectly in-phase with respect to each other, are in the correct ratio (described by Eq. (A4)) with respect to each other, and the only factor reducing the combined efficiency is each-beam losses in the combiner.

Based on this analysis we can define absolute and relative combining efficiencies denoted by η_{abs} and $\eta_{relative}$ respectively, as well as the combiner efficiency $\eta_{combiner}$:

$$\eta_{abs} = \frac{P^{comb}}{P_1^{in} + P_2^{in}};\ \ \eta_{relative} = \frac{P^{comb}}{P^{comb\_MAX}};\ \ \eta_{combiner} = \frac{P^{comb\_MAX}}{P_1^{in} + P_2^{in}} = \frac{\eta_1 P_1^{in} + \eta_2 P_2^{in}}{P_1^{in} + P_2^{in}}. \tag{A6}$$

Then

$$\eta_{abs} = \eta_{combiner} \cdot \eta_{relative}. \tag{A7}$$

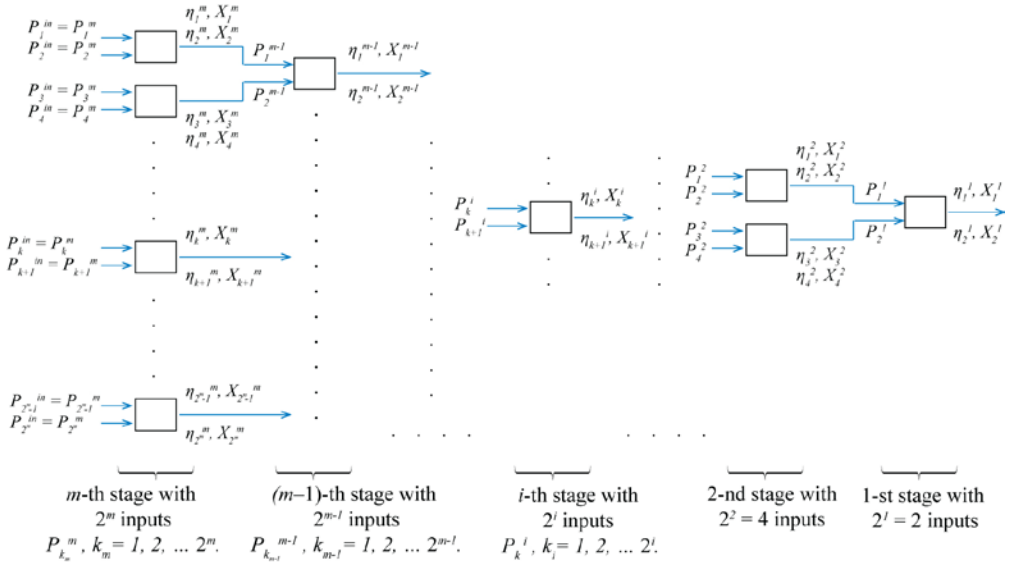

Fig. 2.12 Schematic of a general N→1 binary-tree beam combiner

Now let's generalize this to the case of arbitrarily-large binary-tree combiner, which combines *N* inputs into one output. Fig. 2.12 depicts a general binary-tree configuration consisting of *m* stages. The 1-st stage (output stage) consists of one combiner with $2^1 = 2$ internal inputs, the 2nd stage consists of two combiners and $2^2 = 4$ internal inputs, and so on until the last *m*-th stage (actual input stage) which consists of *m* combiners with $N = 2^m$ inputs, which are also the actual external inputs into this binary-tree combining arrangement. Total number of individual combining elements in this arrangement is

$$K = 2^{m-1} + 2^{m-2} + ... + 2^0 = 2^m - 1 = N - 1. \tag{A8}$$

This figure also introduces a system for labeling all the internal-stage inputs $P_{k_i}^{i}$ into each combining element by the stage number *i* and the corresponding internal-input number k_i , here k_i = 1, 2, ..., 2^i , as well as combining-element efficiencies $\eta_{k_i}^{i}$ and splitting ratios $X_{k_i}^{i}$ for each corresponding input at each combining element in each binary-tree stage. The $N = 2^m$ inputs $P_{k_m}^{m}$ into the *m-th* stage can also be denoted as external inputs $P_{k_m}^{\text{in}}$ into the complete binary-tree arrangement. Each internal or external input field is characterized by complex amplitude $\tilde{E}_{k_i}^{i} = E_{k_i}^{i} \cdot e^{i\phi_{ki}^{i}}$, and power is related to field amplitude through $P_{k_i}^{i} = c\varepsilon_0 nA \cdot \left(E_{k_i}^{i}\right)^2 / 2$.

Each combining element in the *i*-th stage of this binary tree combines two internal input signals $E_{k_i}^{i}$ and $E_{k_i+1}^{i}$, and k_i in this pair should be an odd-integer number and k_i +1 should be an even-integer number. Based on that splitting ratio for each of the two input beams into a combining element is $X_{k_i}^{i}$ if k_i is an odd-integer, and $X_{k_i+1}^{i} = 1 - X_{k_i}^{i}$ if k_i +1 is an even-integer.

Each individual binary-tree input $I_{k_m}^{\text{in}\,/}$ travels an individual path from the tree input stage to the common combined output. This path can be identified by a particular sequence of combining-element inputs the signal passes, expressed as a sequence of the corresponding stage-label values

$$k_m^{/} \Rightarrow k_m^{/}, k_{m-1}^{/}, ..., k_i^{/}, ..., k_2^{/}, k_1^{/} . \tag{A9}$$

Where symbol $\Rightarrow$ indicates that each individual path corresponds uniquely to an external input with a label $k_m^{/}$. Obviously, there are *N* different individual paths.

Using this notation we can express the output of this binary-tree combiner $P_{k_m}^{out}$ when only one input signal $P_{k_m}^{in}$ present at the input of the binary tree (i.e. no coherent combining) as

$$P_{k_m}^{out} = \eta_{k_m}^{m} \cdot X_{k_m}^{m} \cdot ... \cdot \eta_{k_i}^{i} \cdot X_{k_i}^{i} \cdot ... \cdot \eta_{k_1}^{1} \cdot X_{k_1}^{1} \cdot P_{k_m}^{in}, \tag{A10}$$

where $k_m = 1, ..., N$.

Here all the efficiencies and splitting ratios correspond to a particular and unique path that the input signal $P_{k_m}^{in}$ takes when propagating from the tree input to its common output.

In order to describe the coherently-combined output from the tree with all input signals present let's first consider the combining in the 1-st stage (the output stage), expressed in terms of amplitudes $E_{1,2}^{1}$ and phases $\phi_{1,2}^{1}$ of the signals at this stage input:

$$\widetilde{E}^{comb} = \left(\sqrt{\eta_1^1 X_1^1} E_1^1 \cdot e^{i\phi_1^1} + \sqrt{\eta_2^1 X_2^1} E_2^1 \cdot e^{i\phi_2^1} \right). \tag{A11}$$

Each of the two input amplitudes in this expression can be expressed through individual amplitudes $E_{1,2,3,4}^{2}$ and phases $\phi_{1,2,3,4}^{2}$ of inputs into the second stage:

$$\begin{aligned} E_1^1 &= \left(\sqrt{\eta_1^2 X_1^2} E_1^2 \cdot e^{i\phi_1^2} + \sqrt{\eta_2^2 X_2^2} E_2^2 \cdot e^{i\phi_2^2} \right), \\ E_2^1 &= \left(\sqrt{\eta_3^2 X_3^2} E_3^2 \cdot e^{i\phi_3^2} + \sqrt{\eta_4^2 X_4^2} E_4^2 \cdot e^{i\phi_4^2} \right). \end{aligned} \tag{A12}$$

This should be continued all the way until the *m*-th stage (input). It is straightforward to see that the overall result could be expressed as follows:

$$\widetilde{E}^{comb} = \sum_{k_m = 1, N} \sqrt{\eta_{k_m}^{m} \cdot X_{k_m}^{m} \cdot ... \cdot \eta_{k_1}^{1} \cdot X_{k_1}^{1}} \cdot E_{k_m}^{in} \cdot e^{i\left(\omega t + \phi_{km}^{m} + ... + \phi_{k1}^{1}\right)}. \tag{A13}$$

Here summation over $k_m = 1, N$ implies the convention of Eq. (A9), where each particular value of k_m identifies a particular sequence of all other indices of all the η-s, *X*-s and φ-s

in each term of the summation sequence, thus identifying the path this input signal passes in the binary tree.

Since the binary tree consists of two-port combiners described earlier, it is easy to see that coherent combining efficiency in general depends on relationships between each combining-element splitting ratio X_i and the ratio between powers X_i' of the signals at the input of this combining element, combining element losses corresponding to each of the two inputs into each combiner η'_i and η'_{i+1}, relative phase difference $\Delta\varphi$ between the inputs into each combining element.

This means that in order to achieve maximum combining efficiency for a given binary-combiner tree (with fixed losses in each of the combining elements) it is necessary to have K degrees of freedom in controlling all internal-input amplitudes $E^i_{k_i}$ and K degrees of freedom in controlling all internal-input phases $\phi^i_{k_i}$ in the binary-tree combiner. It is straightforward to show that since there are $N = K + 1$ external-input signals, this control can be achieved at any total power by controlling N external-input signal amplitudes and N external-input signal phases. With this consideration Eq. (A13) could be rewritten slightly differently:

$$\widetilde{E}^{comb} = \sum_{k_m=1,N} \sqrt{\eta^m_{k_m} \cdot X^m_{k_m} \cdot \ldots \cdot \eta^1_{k_1} \cdot X^1_{k_1}} \cdot E^{in}_{k_m} \cdot e^{i\left(\omega t + \phi^{out}_{km}\right)}. \qquad \text{(A14)}$$

Here we replaced the sum of all the inter-stage phases $\phi^m_{km} + \ldots + \phi^1_{k1}$ by a "cumulative" phase ϕ^{out}_{km} at the tree output, corresponding to an external input labeled by k_m. Note that implicitly this also includes any phases that signals might acquire when propagating between individual combining elements, since all these additional phase contributions can also be compensated by controlling the phases of the N external-input signals.

Combined output power can be calculated from Eq. (A14):

$$\begin{aligned} P^{comb} &= c\varepsilon_0 nA \cdot \left\langle \left(\frac{1}{2} \sum_{k_m=1,N} \sqrt{\eta_{k_m}^m \cdot X_{k_m}^m \cdot \ldots \cdot \eta_{k_1}^1 \cdot X_{k_1}^1} \cdot E_{k_m}^{in} \cdot e^{i\left(\omega t + \phi_{km}^{out}\right)} + \frac{1}{2} c.c. \right)^2 \right\rangle \\ &= \frac{c\varepsilon_0 nA}{2} \sum_{k_n=1,N} \sum_{k_m=1,N} \sqrt{\eta_{k_n}^n \cdot X_{k_n}^n \cdot \ldots \cdot \eta_{k_1}^1 \cdot X_{k_1}^1} \sqrt{\eta_{k_m}^m \cdot X_{k_m}^m \cdot \ldots \cdot \eta_{k_1}^1 \cdot X_{k_1}^1} \cdot \\ &\quad \times E_{k_n}^{in} \cdot E_{k_m}^{in} \cdot \cos(\phi_{km}^{out} - \phi_{kn}^{out}) \\ &= \sum_{i=1,N} P_i^{out} + \sum_{\substack{j=1,N \\ j \neq i}} \sum_{i=1,N} \sqrt{P_j^{out} \cdot P_i^{out}} \cdot \cos \Delta\phi_{ji} . \end{aligned} \quad . \qquad \text{(A15)}$$

Here brackets $\langle ... \rangle$ denote time average, $\Delta\phi_{ij} = \left(\phi_j - \phi_i\right)$ is the phase difference between a pair of corresponding output signals *i* and *j*, and each output power is defined by Eq. (A10).

The maximum constructive interference occurs when all $\Delta\phi_{ij} = \left(\phi_j - \phi_i\right) = 0$, i.e. there are no phase errors, producing the maximum achievable combined power:

$$P^{comb\_MAX} = \left(\sum_{i=1,N} \sqrt{P_i^{out}} \right)^2 . \qquad \text{(A16)}$$

Let's denote $P_{k_m}^{/} = \eta_{k_m}^m \cdot \ldots \cdot \eta_{k_i}^i \cdot \ldots \cdot \eta_{k_1}^1 \cdot P_{k_m}^{in}$ and $P_{tot}^{/} = \sum_{k_m=1,N} P_{k_m}^{/}$. (A17)

According to Eq. (A10)

$$P_{k_m}^{out} = \eta_{k_m}^m \cdot X_{k_m}^m \cdot \ldots \cdot \eta_{k_i}^i \cdot X_{k_i}^i \cdot \ldots \cdot \eta_{k_1}^1 \cdot X_{k_1}^1 \cdot P_{k_m}^{in} = X_{k_m}^m \cdot \ldots \cdot X_{k_i}^i \cdot \ldots \cdot X_{k_1}^1 \cdot P_{k_m}^{/} . \qquad \text{(A18)}$$

It can be shown that the maximum in-phase combining efficiency occurs when external-input powers are:

$$P_{k_m}^{/} = X_{k_m}^m \cdot \ldots \cdot X_{k_i}^i \cdot \ldots \cdot X_{k_1}^1 \cdot P_{tot}^{/} . \qquad \text{(A19)}$$

In this case, substitute Eq. (A19) and Eq. (A18) into Eq. (A16), and we get:

$$P^{comb\_MAX} = P_{tot}^{/}\left(\sum_{k_m=1,N}\left(X_{k_m}^{m}\cdot\ldots\cdot X_{k_i}^{i}\cdot\ldots\cdot X_{k_1}^{1}\right)\right)^2. \tag{A20}$$

Here the same summation convention as in Eq. (A13) applies. Since as it was noted earlier, for each binary-tree combining component splitting ratios between two inputs are related by $X_{k_i+1}^{i}=1-X_{k_i}^{i}$ if ki is an odd-integer, it is straightforward to show that

$$\sum_{k_m=1,N}\left(X_{k_m}^{m}\cdot\ldots\cdot X_{k_i}^{i}\cdot\ldots\cdot X_{k_1}^{1}\right)=1. \tag{A21}$$

Consequently we can obtain an alternative expression to the Eq. (A16) of the maximum achievable combining power

$$P^{comb\_MAX} = P_{tot}^{/} = \sum_{k_m=1,N}P_{k_m}^{/} = \sum_{k_m=1,N}\left(\eta_{k_m}^{m}\cdot\ldots\cdot\eta_{k_i}^{i}\cdot\ldots\cdot\eta_{k_1}^{1}\cdot P_{k_m}^{in}\right). \tag{A22}$$

Based on this analysis we can define absolute and relative combining efficiencies denoted by η_{abs} and $\eta_{relative}$ respectively, as well as the combiner efficiency $\eta_{combiner}$:

$$\eta_{abs} = \frac{P^{comb}}{\sum_{k_m=1,N}P_{k_m}^{in}}, \tag{A23}$$

$$\eta_{relative} = \frac{P^{comb}}{P^{comb\_MAX}} = \frac{P^{comb}}{\left(\sum_{k_m=1,N}\sqrt{P_{k_m}^{out}}\right)^2} = \frac{P^{comb}}{\sum_{k_m=1,N}\left(\eta_{k_m}^{m}\cdot\ldots\cdot\eta_{k_i}^{i}\cdot\ldots\cdot\eta_{k_1}^{1}\cdot P_{k_m}^{in}\right)}, \tag{A24}$$

and

$$\eta_{combiner} = \frac{P^{comb\_MAX}}{\sum_{k_m=1,N}P_{k_m}^{in}} = \frac{\left(\sum_{k_m=1,N}\sqrt{P_{k_m}^{out}}\right)^2}{\sum_{k_m=1,N}P_{k_m}^{in}} = \frac{\sum_{k_m=1,N}\left(\eta_{k_m}^{m}\cdot\ldots\cdot\eta_{k_i}^{i}\cdot\ldots\cdot\eta_{k_1}^{1}\cdot P_{k_m}^{in}\right)}{\sum_{k_m=1,N}P_{k_m}^{in}}. \tag{A25}$$

Then

$$\eta_{abs} = \eta_{combiner}\cdot\eta_{relative}. \tag{A26}$$

2.8 Appendix B: LOCSET combining efficiency as a function of phase-modulation amplitude

Here we show how the analytical expression for combining efficiency in the LOCSET scheme as a function of phase modulation amplitude, Eq. (2), is derived. The combined electric field in the time domain from a system employing the self-referenced LOCSET technique [17] can be written as

$$E^{comb}(t) = E_1^{out}\cos(\omega_L t + \phi_1) + \sum_{k=2}^{N} E_k^{out}\cos(\omega_L t + \phi_k + \beta_k \sin(\omega_k t)), \tag{B1}$$

where N is the total number of elements, E_1^{out} and E_k^{out} are the field amplitudes for the unmodulated and k^{th} phase modulated elements, ϕ_1 and ϕ_k are optical phases, ω_L is the laser frequency, ω_k is an RF modulation frequency, and β_k is a phase modulation amplitude.

For calculations we assume the phase locked condition and set ϕ_1 and ϕ_k equal to zero. The phase modulation amplitudes are all set to the same value β. The combined power P^{comb} is equal to the total field squared (to within a proportionality constant) and when averaged over a time T that is larger than the optical period ($2\pi/\omega_L$) but smaller than any of the modulation periods ($2\pi/\omega_k$) gives

$$\begin{aligned} P^{comb}(t,\beta) &= \frac{c\varepsilon_0 nA}{T}\int_{t-\frac{1}{2}T}^{t+\frac{1}{2}T}\left|E^{comb}(\tau)\right|^2 d\tau \\ &= c\varepsilon_0 nA\cdot\left[\frac{1}{2}\sum_{k=1}^{N}E_k^{out}E_k^{out} + \sum_{k=2}^{N}E_1^{out}E_k^{out}\cos(\beta\sin(\omega_k t))\right. \\ &\quad + \frac{1}{2}\sum_{k=2}^{N}\sum_{\substack{m=2,\\ m\neq k}}^{N}E_m^{out}E_k^{out}\left[\cos(\beta\sin(\omega_k t))\cos(\beta\sin(\omega_m t))\right. \\ &\quad \left.\left. + \sin(\beta\sin(\omega_k t))\sin(\beta\sin(\omega_m t))\right]\right]. \end{aligned} \tag{B2}$$

As seen in Eq. (B2) the combined power is still time dependent and depends on the phase modulation amplitude β. Our feedback detector does indeed measure the time dependent combined power (this is necessary because the feedback electronics have to demodulate the individual RF modulations), but when measuring combining efficiencies we used a slower detector that did not respond to the modulation time dependence. Therefore the measured time averaged power is given by

$$P^{comb}(\beta) = \frac{1}{T_2}\int_0^{T_2} P^{comb}(t,\beta)\,dt, \tag{B3}$$

where T_2 (the response time of the slow detector) is several times greater than $2\pi/|\omega_k - \omega_m|$ for any possible k and m values. The theoretical maximum combined power occurs in the limit of β equal to zero and is given by

$$P_{\max}^{comb} = \frac{c\varepsilon_0 nA}{2}\left(\sum_{k=1}^{N} E_k^{out}\right)^2. \tag{B4}$$

The combining efficiency as a function of β becomes

$$\eta_{relative}(\beta) = P^{comb}(\beta)\big/P_{\max}^{comb}. \tag{B5}$$

Using the Fourier series expansions

$$\begin{aligned}\cos(\beta\sin(\omega_k t)) &= J_0(\beta) + 2\sum_{m=1}^{\infty} J_{2m}(\beta)\cos(2m\omega_k t),\\ \sin(\beta\sin(\omega_k t)) &= 2\sum_{n=1}^{\infty} J_{2n-1}(\beta)\sin((2n-1)\omega_k t),\end{aligned} \tag{B6}$$

where J_m is a Bessel function of order m of the first kind to rewrite the terms in Eq. (B2), we substitute Eq. (B2) into Eq. (B3), take the asymptotic limit for large T_2, and calculate the combining efficiency from Eq. (B5) to give

$$\eta_{relative}(\beta) = \frac{\sum_{k=1}^{N} {E_k^{out}}^2 + \sum_{k=2}^{N} 2E_1^{out} E_k^{out} J_0(\beta) + \sum_{k=2}^{N} \sum_{\substack{m=2, \\ m \neq k}}^{N} E_m^{out} E_k^{out} {J_0}^2(\beta)}{\left(\sum_{k=1}^{N} E_k^{out} \right)^2}. \quad \text{(B7)}$$

Eq. (B7) is equivalent to the desired result, Eq. (2), when written in terms of powers rather than electric field amplitudes.

2.9 Appendix C: Circuit design of the LOCSET phase-locking module

Fig. 2.13 shows the circuit schematics of the LOCSET phase-locking feedback module, while Fig. 2.14 to Fig. 2.17 show the detailed diagrams of the four parts (Part A to Part D) of the phase-locking module as marked in Fig. 2.13. Fig. 18 shows a photo of the real phase-locking feedback module. Table 2.1 shows the values of the circuit components.

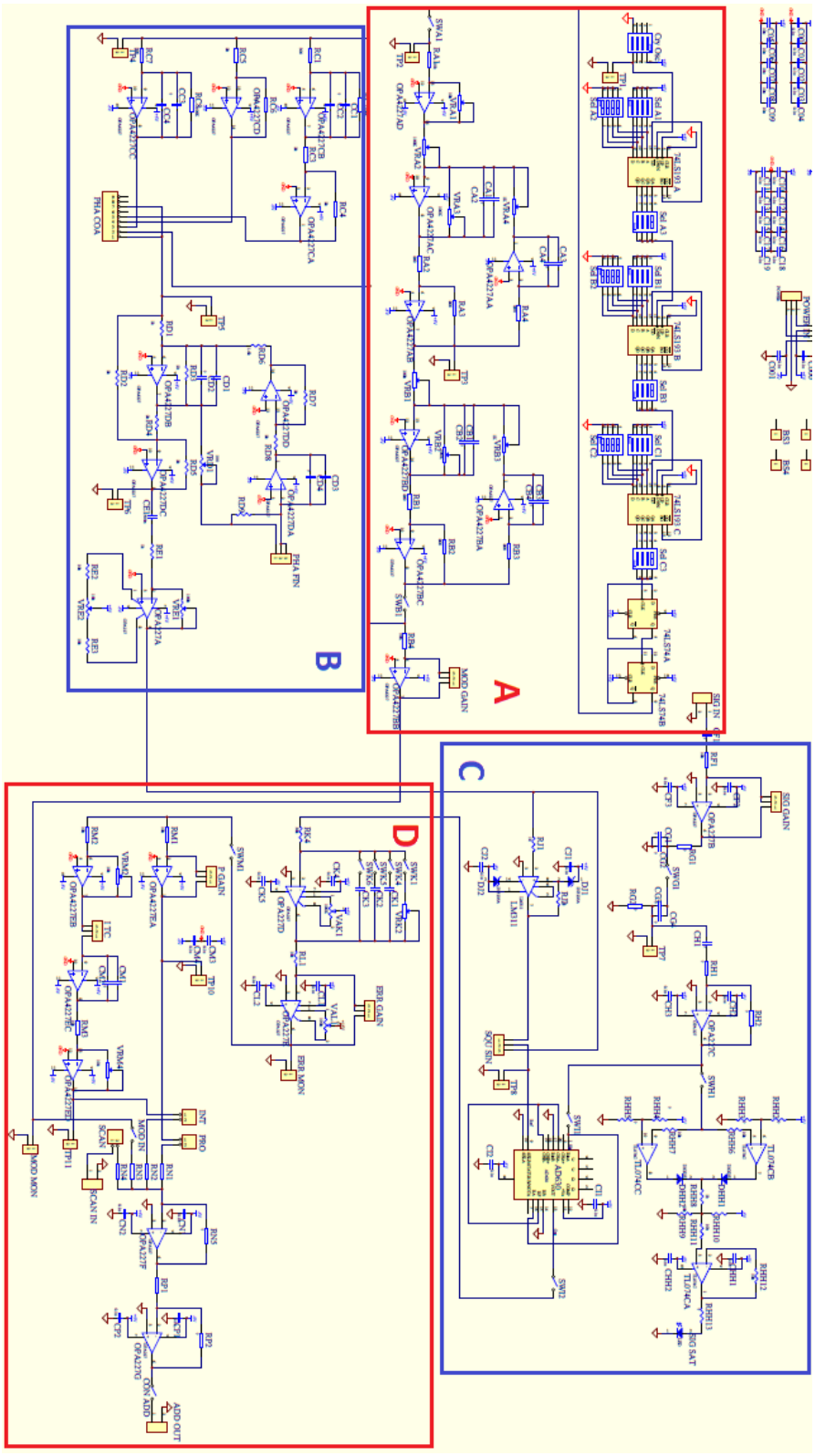

Fig. 2.13 The circuit schematics of the phase-locking feedback module. Details of the four parts (Part A to Part D) are shown in Fig. 2.14 to Fig. 2.17.

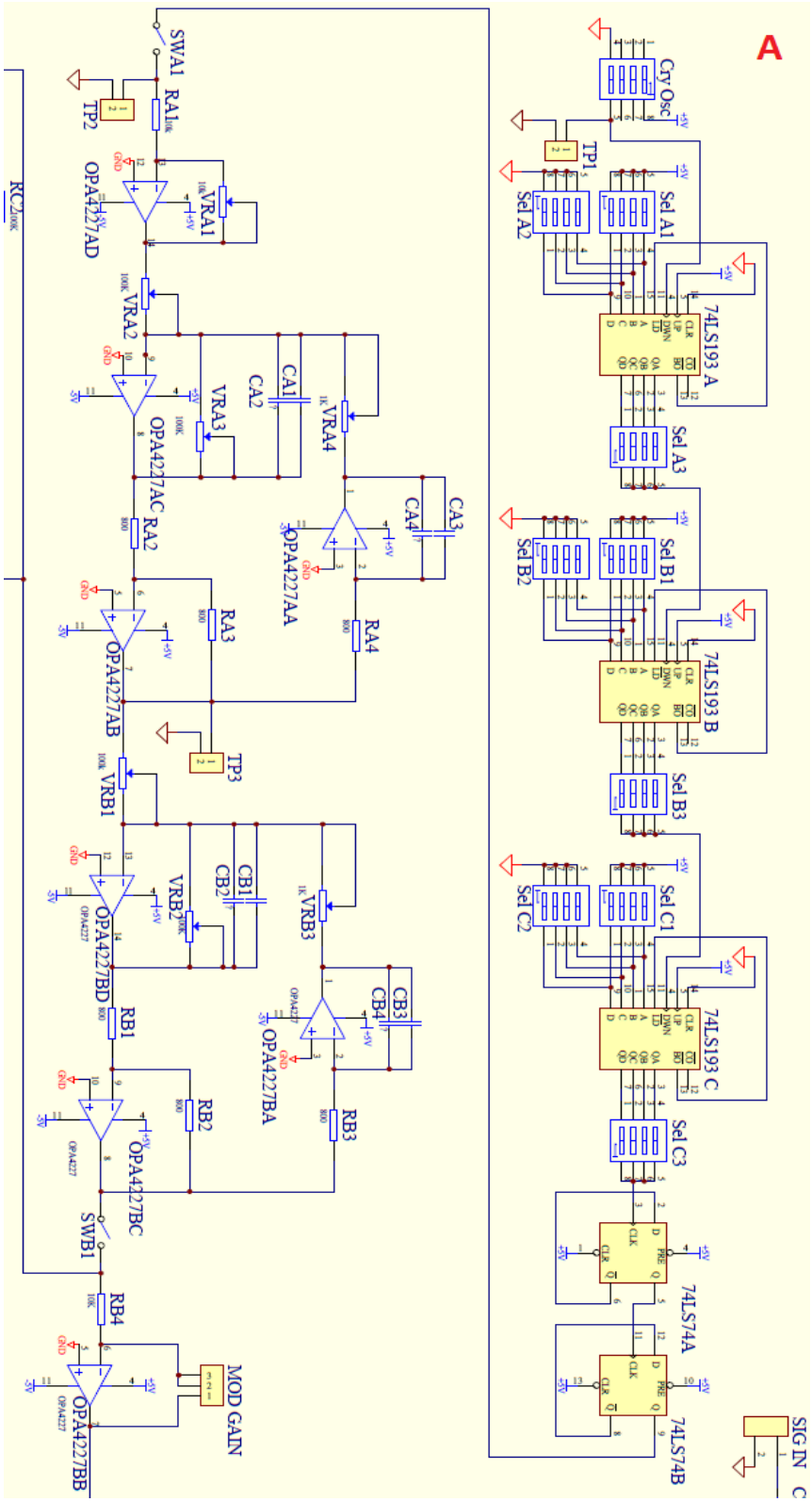

Fig. 2.14 The circuit diagram of Part A (marked in Fig. 2.13) of the phase-locking feedback module.

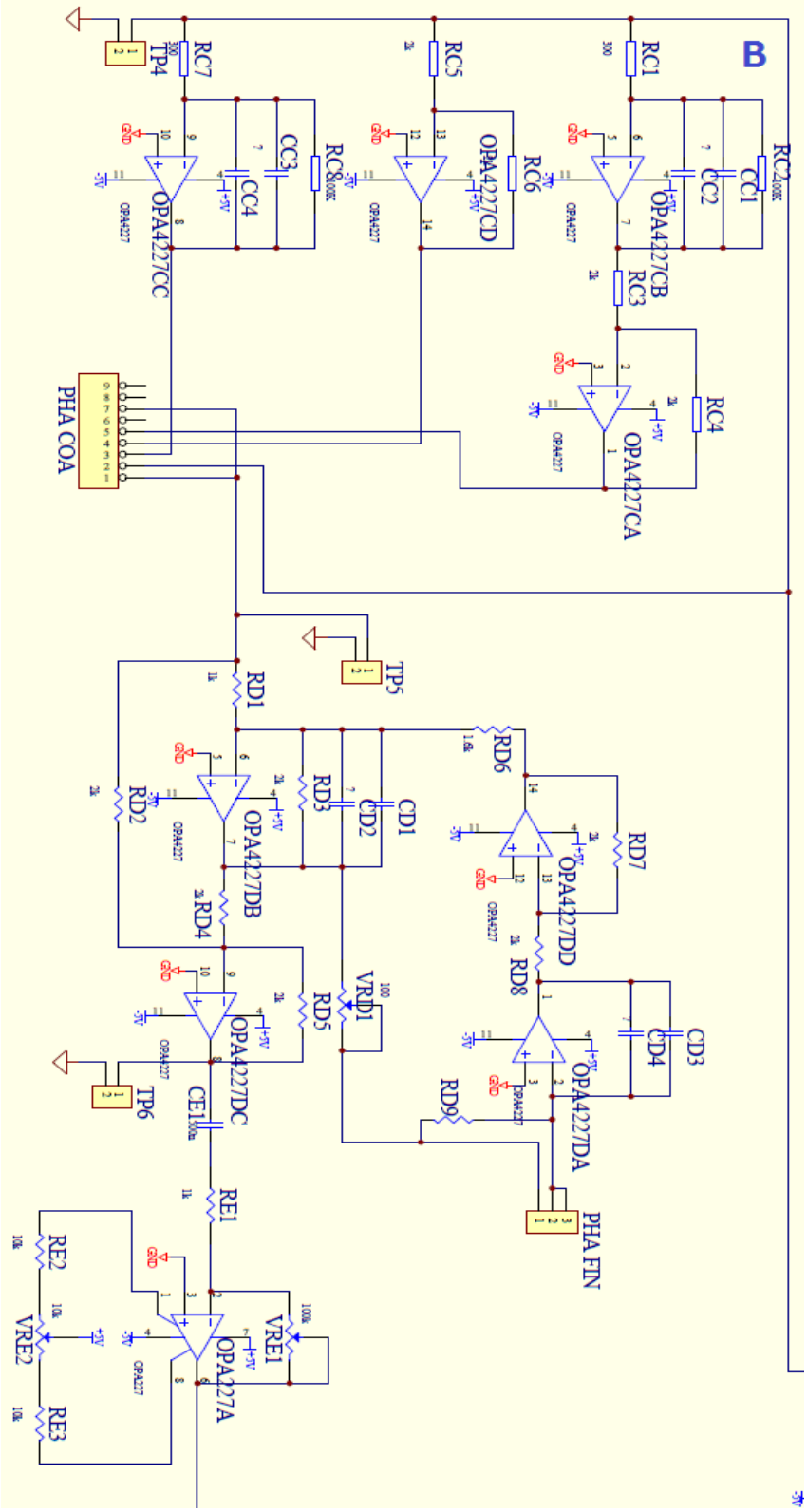

Fig. 2.15 The circuit diagram of Part B (marked in Fig. 2.13) of the phase-locking feedback module.

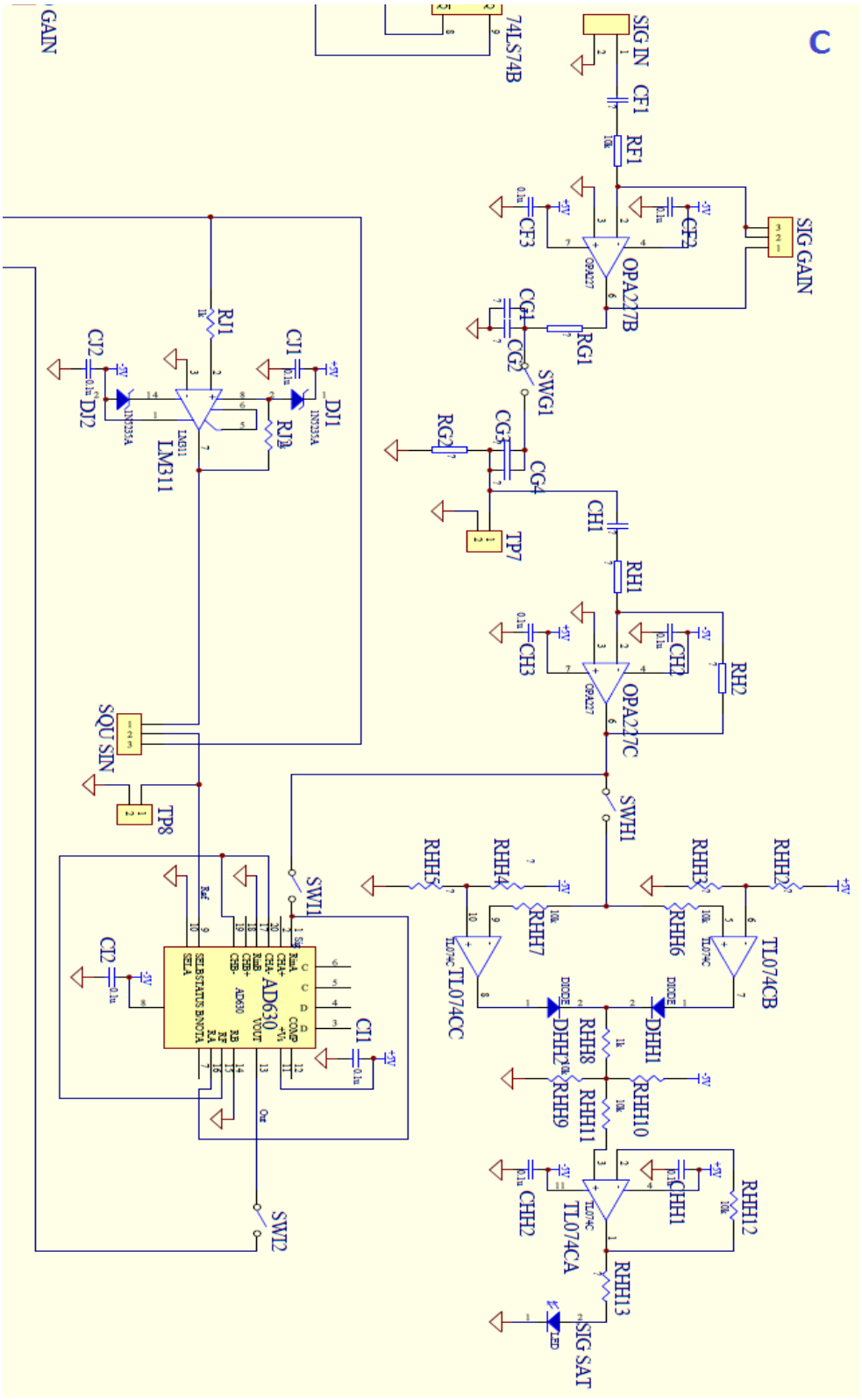

Fig. 2.16 The circuit diagram of Part C (marked in Fig. 2.13) of the phase-locking feedback module.

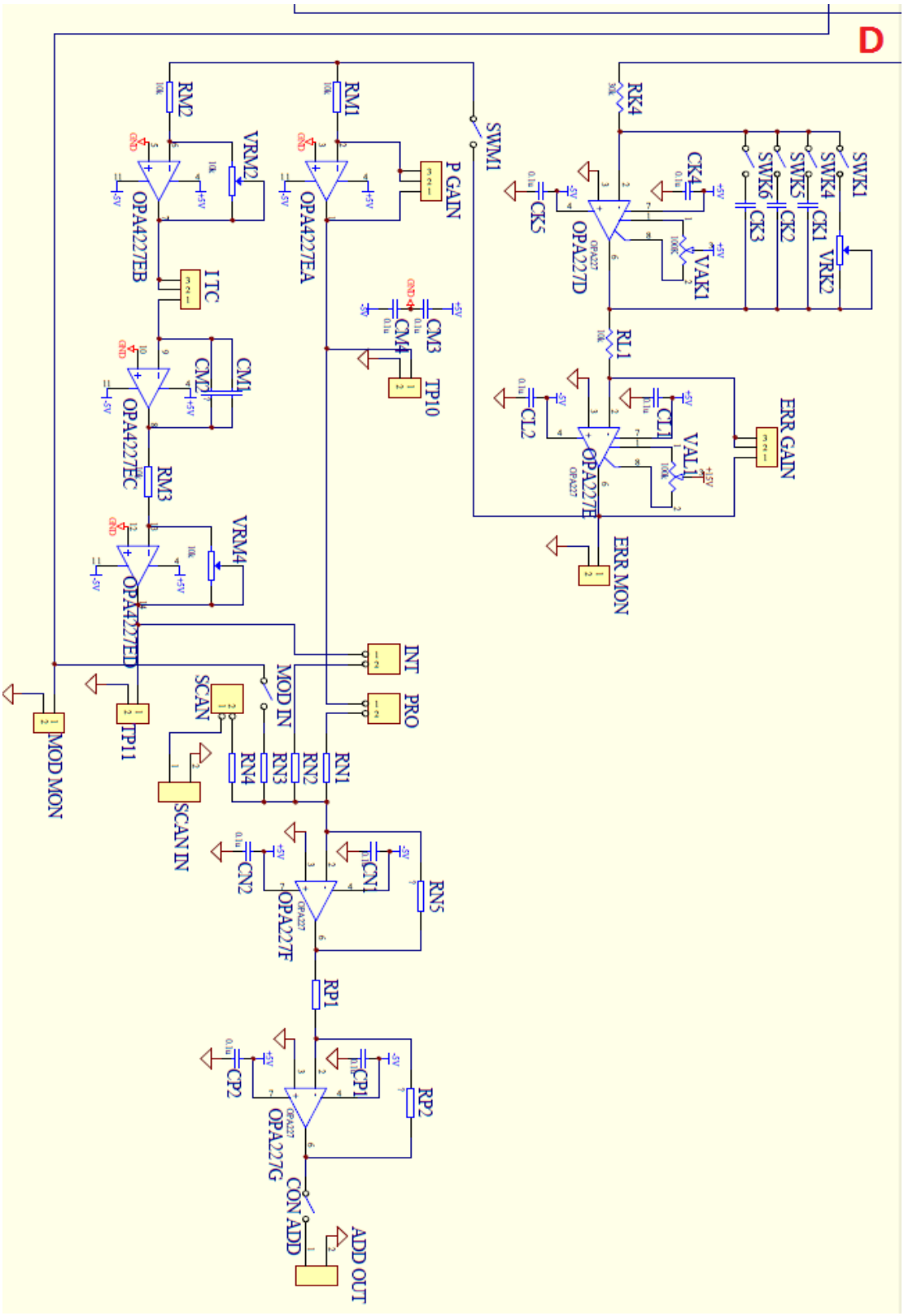

Fig. 2.17 The circuit diagram of Part D (marked in Fig. 2.13) of the phase-locking feedback module.

Component	Value	Component	Value	Component	Value	Component	Value
74LS193 A	74LS193	CI2	0.1u	RB1	800	RN1	5k
74LS193 B	74LS193	CJ1	0.1u	RB2	800	RN2	5k
74LS193 C	74LS193	CJ2	0.1u	RB3	800	RN3	5k
74LS74	74LS74	CK1	330n	RB4	10K	RN4	5k
AD630	AD630	CK4	0.1u	RC1	300	RN5	5k
C00	0.1u	CK5	0.1u	RC2	100K	RP1	10k
C000	0.1u	CL1	0.1u	RC3	2k	RP2	10k
C001	0.1u	CL2	0.1u	RC4	2k	SCAN	Toggle
C01	0.1u	CM1	100u	RC5	2k	Sel A1	SWDip
C02	0.1u	CM3	0.1u	RC6	2k	Sel A2	SWDip
C03	0.1u	CM4	0.1u	RC7	300	Sel A3	SWDip
C04	0.1u	CN1	0.1u	RC8	100K	Sel B1	SWDip
C05	10u	CN2	0.1u	RD1	1k	Sel B2	SWDip
C06	10u	CP1	0.1u	RD2	2k	Sel B3	SWDip
C07	10u	CP2	0.1u	RD3	2k	Sel C1	SWDip
C08	10u	DHH1	1N5235A	RD4	2k	Sel C2	SWDip
C09	10u	DHH2	1N5235A	RD5	2k	Sel C3	SWDip
C10	0.1u	DJ1	Short	RD6	1.6k	SIG GAIN	Pot 100k
C11	0.1u	DJ2	Short	RD7	2k	SIG SAT	LED
C12	0.1u	ERR GAIN	Pot 100k	RD8	2k	SQU SIN	Connector
C13	0.1u	I TC	Pot 100k	RD9	Debug	SWA1	Connector
C14	0.1u	INT	Toggle	RE1	1k	SWB1	Connector
C15	0.1u	LM311	LM311	RE2	10k	SWG1	Connector
C16	0.1u	MOD GAIN	Pot 100k	RE3	10k	SWH1	Connector
C17	0.1u	MOD IN	Connector	RF1	2k	SWI1	Connector
C18	0.1u	OPA227A	OPA227	RG1	2k	SWI2	Connector
C19	0.1u	OPA227B	OPA227	RG2	8k	SWK1	Connector
CA1	43.2n	OPA227C	OPA227	RH1	1k	SWK4	Connector
CA3	43.2n	OPA227D	OPA227	RH2	30k	SWK5	Connector
CB1	43.2n	OPA227E	OPA227	RHH11	10k	SWK6	Connector
CB3	43.2n	OPA227F	OPA227	RHH12	10k	SWM1	Connector
CC1	100n	OPA227G	OPA227	RHH13	Short	TL074C	TL074C
CC3	100n	OPA4227A	OPA4227	RHH2	Debug	VAK1	100k
CD1	120n	OPA4227B	OPA4227	RHH3	Debug	VAL1	100k
CD3	120n	OPA4227C	OPA4227	RHH4	Debug	VRA1	10k
CE1	1u	OPA4227D	OPA4227	RHH5	Debug	VRA2	100K
CF1	100n	OPA4227E	OPA4227	RHH6	10k	VRA3	100K
CF2	0.1u	P GAIN	Pot 100k	RHH7	10k	VRA4	1K
CF3	0.1u	PHA COA	ToggleRotary	RHH8	1k	VRB1	100k
CG1	10n	PHA FIN	Pot 100	RHH9	10k	VRB2	100K
CG3	10n	POWER	ToggleDP	RJ1	1k	VRB3	1K
CH1	47n	POWER IN	Tip	RJ2	1k	VRD1	100
CH2	0.1u	PRO	Toggle	RK4	30k	VRE1	100k
CH3	0.1u	RA1	10k	RL1	1k	VRE2	10k
CHH1	0.1u	RA2	800	RM1	5k	VRK2	200k
CHH2	0.1u	RA3	800	RM2	2k	VRM2	10k
CI1	0.1u	RA4	800	RM3	5k	VRM4	100k

Table 2.1 The values of the circuit components of the phase-locking feedback module.

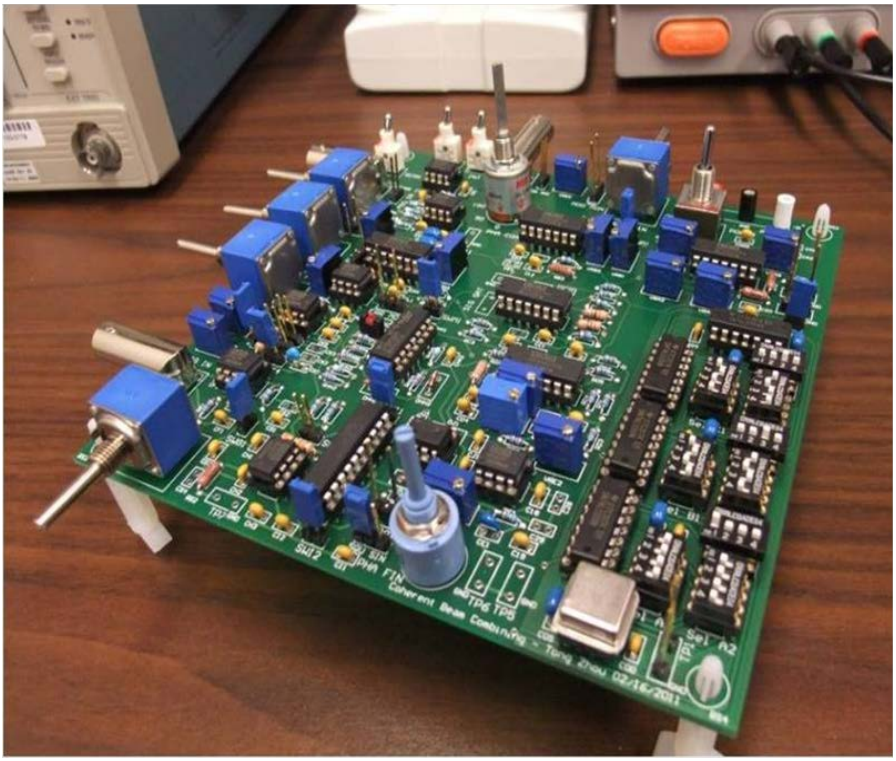

Fig. 2.18 A photo of the real phase-locking feedback module.

2.10 References

1. D. J. Richardson, J. Nilsson, and W. A. Clarkson, "High power fiber lasers: current status and future perspectives [Invited]," J. Opt. Soc. Am. B **27**, B63-B92 (2010).

2. T. Eidam, S. Hanf, E. Seise, T. V. Andersen, T. Gabler, C. Wirth, T. Schreiber, J. Limpert, and A. Tünnermann, "Femtosecond fiber CPA system emitting 830 W average output power," Opt. Lett. **35**, 94-96 (2010).

3. J. Limpert, F. Roser, D. N. Schimpf, E. Seise, T. Eidam, S. Hädrich, J. Rothhardt, C. J. Misas, and A. Tünnermann, "High repetition rate gigawatt peak power fiber laser systems: challenges, design, and experiment," IEEE J. Sel. Top. Quantum Electron. **15**, 159-169 (2009).

4. T. Schreiber, D. Schimpf, D. Müller, F. Röser, J. Limpert, and A. Tünnermann, "Influence of pulse shape in self-phase-modulation-limited chirped pulse fiber amplifier systems," J. Opt. Soc. Am. B **24**, 1809-1814 (2007).

5. T. Y. Fan, "Laser beam combining for high-power, high-radiance sources," IEEE J. Sel. Top. Quantum Electron **11**, 567-577 (2005).

6. G. D. Goodno, C. P. Asman, J. Anderegg, S. Brosnan, E. C. Cheung, D. Hammons, H. Injeyan, H. Komine, W. H. Long, M. McClellan, S. J. McNaught, S. Redmond, R.

Simpson, J. Sollee, M. Weber, S. B. Weiss, and M. Wickham, "Brightness-scaling potential of actively phase-locked solid-state laser arrays," IEEE J. Sel. Top. Quantum Electron **13**(3), 460–472 (2007).

7. J. Anderegg, S. Brosnan, M. Weber, H. Komine, and M. Wickham, "8-W coherently phased 4-element fiber array," Proc. SPIE, **4974**, 1–6 (2003).

8. E. C. Cheung, M. Weber, and R. R. Rice, "Phase locking of a pulsed fiber amplifier," in Advanced Solid-State Photonics, OSA Technical Digest Series (CD) (Optical Society of America, 2008), paper WA2.

9. E. Seise, A. Klenke, J. Limpert, and A. Tünnermann, "Coherent addition of fiber-amplified ultrashort laser pulses," Opt. Express **18**, 27827-27835 (2010).

10. L. Daniault, M. Hanna, L. Lombard, Y. Zaouter, E. Mottay, D. Goular, P. Bourdon, F. Druon, and P. Georges, "Coherent beam combining of two femtosecond fiber chirped-pulse amplifiers," Opt. Lett. **36**, 621-623 (2011).

11. G. J. Swanson, J. R. Leger, and M. Holz, "Aperture filling of phase-locked laser arrays," Opt. Lett. **12**, 245-247 (1987).

12. M. Tempus, W. Luthy, and H. P. Weber, "Coherent recombination of laser beams with interferometrical phase control," Appl. Phys. B: Photophys. Laser Chem. **56**, 79-83 (1993).

13. R. Uberna, A. Bratcher, and B. G. Tiemann, "Coherent polarization beam combination," IEEE J. Quantum Electron. **46**(8), 1191–1196 (2010).

14. E. C. Cheung, J. G. Ho, G. D. Goodno, R. R. Rice, J. Rothenberg, P. Thielen, M. Weber, and M. Wickham, "Diffractive-optics-based beam combination of a phase-locked fiber laser array," Opt. Lett. **33**, 354-356 (2008).

15. R. Uberna, A. Bratcher, T. G. Alley, A. D. Sanchez, A. S. Flores, and B. Pulford, "Coherent combination of high power fiber amplifiers in a two-dimensional re-imaging waveguide," Opt. Express **18**, 13547-13553 (2010).

16. G. D. Goodno, H. Komine, S. J. McNaught, S. B. Weiss, S. Redmond, W. Long, R. Simpson, E. C. Cheung, D. Howland, P. Epp, M. Weber, M. McClellan, J. Sollee, and H. Injeyan, "Coherent combination of high-power, zigzag slab lasers," Opt. Lett. **31**, 1247-1249 (2006).

17. T. M. Shay, "Theory of electronically phased coherent beam combination without a reference beam," Opt. Express **14**, 12188-12195 (2006).

18. T. M. Shay, V. Benham, J. T. Baker, A. D. Sanchez, D. Pilkington, and C. A. Lu, "Self-synchronous and self-referenced coherent beam combination for large optical arrays," IEEE Journal of Selected Topics in Quantum Electronics **13**, 480-486 (2007).

19. W. Liang, N. Satyan, F. Aflatouni, A. Yariv, A. Kewitsch, G. Rakuljic, and H. Hashemi, “Coherent beam combining with multilevel optical phase-locked loops,” J. Opt. Soc. Am. B **24**, 2930-2939 (2007).

20. C. D. Nabors, “Effects of phase errors on coherent emitter arrays,” Appl. Opt. **33**, 2284-2289 (1994).

21. W. H. Renninger, A. Chong, and F. W. Wise, “Pulse shaping and evolution in normal-dispersion mode-locked fiber lasers,” IEEE J. Sel. Top. Quantum Electron. **18**, 389-398 (2012).

22. G. D. Goodno, C. Shih, and J. E. Rothenberg, “Perturbative analysis of coherent combining efficiency with mismatched lasers,” Opt. Express **18**, 25403-25414 (2010).

23. S. J. Augst, T. Y. Fan, and A. Sanchez, “Coherent beam combining and phase noise measurements of ytterbium fiber amplifiers,” Opt. Lett. **29**, 474-476 (2004).

24. H. Tünnermann, J. H. Pöld, J. Neumann, D. Kracht, B. Willke, and P. Weßels, “Beam quality and noise properties of coherently combined ytterbium doped single frequency fiber amplifiers,” Opt. Express **19**, 19600-19606 (2011).

25. A. Klenke, E. Seise, J. Limpert, and A. Tünnermann, "Basic considerations on coherent combining of ultrashort laser pulses," Opt. Express **19**, 25379-25387 (2011).

26. L. Daniault, M. Hanna, L. Lombard, Y. Zaouter, E. Mottay, D. Goular, P. Bourdon, F. Druon, and P. Georges, "Impact of spectral phase mismatch on femtosecond coherent beam combining systems," Opt. Lett. **37**, 650-652 (2012).

Chapter 3

Femtosecond pulse spectral synthesis in coherently combined multi-channel fiber chirped pulse amplifiers (Spatial and spectral domains)

3.1 Introduction

Technological advantages of fiber lasers are associated with their practicality and their compatibility with high average power operation, due to high efficiency diode pumping, to compatibility with monolithic integration, which enables robust and compact laser systems, and due to fiber geometry with a large surface-to-volume ratio which facilitates efficient heat dissipation [1,2].

However, there are also significant limitations associated with individual fiber lasers. The primary one is a relatively low pulse energy achievable with an individual fiber laser due to a relatively small transverse modal area and a considerably long propagation length leading to nonlinear pulse distortions by stimulated Raman scattering (SRS), self-phase modulation (SPM), or four-wave mixing (FWM), or other constraints associated with energy extraction saturation and optical damage. For example, approximately ~1ns duration pulses in Yb-doped amplifiers (compatible with stretched ultrashort pulses) are limited to pulse energies of ~mJ [3]. Another limitation is associated with spectral gain narrowing when amplifying broad band signals, such as ultrashort optical pulses. For

example, although an Yb-doped fiber gain bandwidth can exceed 100 nm, chirped pulse amplification (CPA) of such a broad bandwidth pulse is not possible with a single Yb-doped fiber amplifier since gain narrowing limits the amplified spectrum to approximately 10-20 nm in high gain systems.

Individual-fiber pulse energy limitations can be overcome by combining multiple lasers or amplifiers. Pulse energy scaling of ultrashort pulses requires coherent phasing of multiple parallel fiber chirped-pulse amplifiers (FCPA), as has been recently demonstrated for up to 4 parallel channels [4] at low power, and up to two channels at high power [5,6]. On the other hand gain spectra limitations of individual lasers can be overcome by combining two different laser gain media, as has been demonstrated by locking and coherent phasing of two individual mode-locked oscillators [7], or seeding two different gain media with a single mode-locked oscillator [8,9]. Although very short durations of only a few optical cycles were produced, the coherent signal synthesis techniques involved in all these experiments are too cumbersome to be practical when combining more than two optical channels. Indeed, the approach in [7] requires repetition rate synchronization and phasing between individual mode-locked oscillators, the approach of [9] uses cross-correlation between the two channels to determine phasing and delay errors, and the approach in [8] relies on a passive optical-length matching between the two channels.

In this work we coherently spectrally combine multiple parallel fiber CPA channels, demonstrating that coherent phasing techniques used for beam combining of multiple parallel amplifiers can also be used for coherent spectral pulse synthesis. We developed a new phase tracking approach used in conjunction with the LOCSET technique [10,11]

which uses two-photon absorption (TPA) detector to measure phasing errors between spectrally non-overlapping combined signals. This approach simultaneously allows for increasing pulse energy and power from a fiber CPA array while increasing signal bandwidth to accommodate shorter pulses. For example, when applied to Yb-doped fiber amplifier arrays this technique allows amplification of individual spectrally-distinct broad-band signals, which when coherently spectrally combined at the amplifier array output can offset gain-narrowing effects of individual high-gain fiber amplification channels. In principle this technique could be extended to parallel array beam combining of different gain media, thus enabling a path towards energy scalable few-cycle optical pulses.

The structure of the chapter is the following. First we describe the basic concept of coherent-spectral combining/signal synthesis using a multi-channel amplifier array. Then we discuss technical issues associated with phase-error detection and correction in this combining system, and show that TPA detection can be used to implement the LOCSET technique [10,11] for coherent phasing of individual channels in a spectrally combined amplifier array. Further, we describe the experimental system used for the proof-of-the-principle demonstration and present experimental results, and finish the chapter with a brief discussion and summary.

3.2 Coherent-spectral combining of fiber CPA arrays

3.2.1 Conceptual outline

Two basic conceptual-layout variations of coherently-spectrally combined fiber CPA arrays are shown in Figs. 3.1(a) and 3.1(b). The main concept here is that initial broad-

band seed pulses from, for example, a mode-locked oscillator, are split into *N* channels *spectrally* so that each channel amplifies a relatively narrow-band and spectrally distinct signal. This is a major difference from a conventional coherent-combining scheme [4-6] where each channel amplifies identical signals. After amplification all signals are spectrally recombined into a broad-band signal again. The essential difference here from a conventional spectral-combining scheme [12] is that different spectral slices are combined *coherently*, i.e. phase-difference between all individual-channel signals is compensated using a suitable phase-error detection, tracking and phase-locking arrangements. This produces a bandwidth-limited broad-band ultrashort pulse consisting of all the different spectral "slices". It also enables the combination of partially overlapped spectra, so that a smooth pulse spectrum can be reconstituted without sacrificing combining efficiency or pulse shape fidelity, as described in more detail further in the text.

Configurations 3.1(a) and 3.1(b) are very different with respect to achievable pulse energy. In system 3.1(a) pulses are spectrally "sliced" after a common stretcher, thus reducing each channel's stretched-pulse duration *N*-times compared to that before spectral splitting (with *N* being a number of channels in the array). Since the maximum achievable energy is proportional to the stretched duration of pulses in an amplifier, achievable energies in this configuration are the same as would come from a single-channel CPA without a coherently combined array. Use of individual stretchers and compressors for each channel shown in 3.1(b) allows to use the same stretched pulse duration in each channel, thus leading to *N*-times increase in achievable pulse

energy while simultaneously increasing the amplified-signal bandwidth by approximately *N*-times.

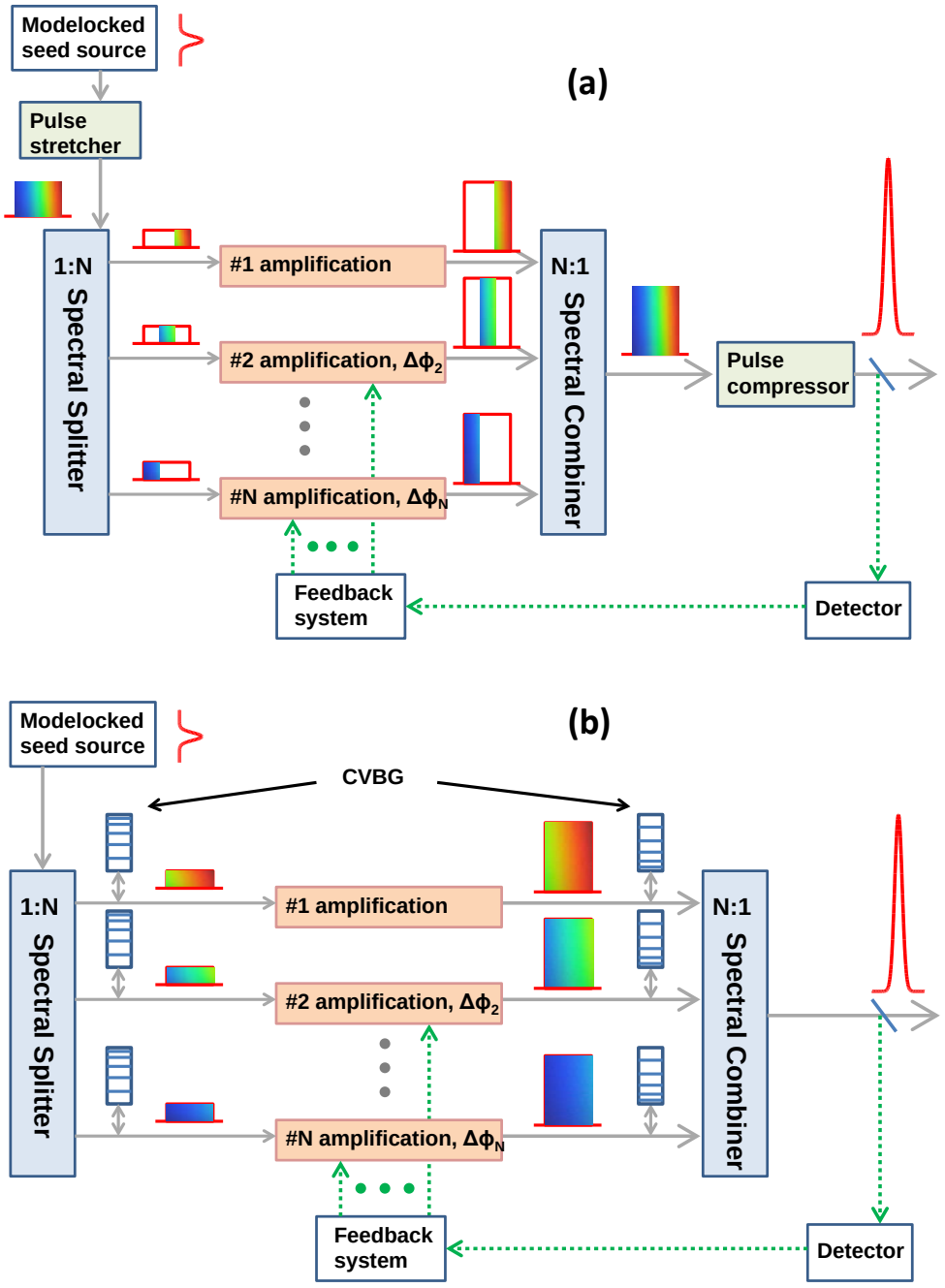

Fig. 3.1 Two alternative architectures of coherently-spectrally combined fiber CPA arrays. Layout in (a) uses a single pulse stretcher and a single compressor, thus being suitable for pulse synthesis, but limited in pulse energy scaling. Layout in (b) shows architecture with individual pulse stretchers and compressors in each channel. This permits pulse energy scaling. Here $\Delta\phi_i$ indicates i^{th} channel phase error with respect to the reference channel (channel #1 in this example).

3.2.2 Spectral combining elements

There is a variety of spectral combining elements that can be used for incoherent spectral combining, such as diffraction gratings [13], volume Bragg gratings [14], and ultra-sharp edge spectral filters based on multi-layered dielectric coatings [15]. Although in principle any of these combining elements could be used for coherent spectral combining, the broad-band spectrum of ultrashort optical pulses makes dielectric-coating filters a much preferred choice. Indeed, diffraction gratings and volume Bragg gratings rely on spatial spectral dispersion, which for broad-band spectrum is always associated with a spatial chirp of a beam. Dielectric-coating filters are spatial-dispersion free and, therefore, can accommodate any bandwidth without inducing spatial chirp.

Spectral splitters/combiners in systems depicted in Fig. 3.1 can be implemented as stacks of multilayer dielectric-film filters, consisting of either short-wave pass (SWP), long-wave pass (LWP), band-pass (BP), or band-reflection (BR) filters. Irrespective of a type of a dielectric filter used, the incident broad-band ultrashort-pulse spectrum after the spectral splitter will be “sliced” into separate partially-overlapping spectra for injecting into each parallel amplification channel. Note that this partial spectral overlap between adjacent channels can only be achieved with spatial-dispersion-free devices. The unique aspect of coherent spectral combining with such devices is that partially-overlapping spectra can be recombined (as shown in Fig. 3.1) without losing combining efficiency in the overlapping part of the spectra, thus enabling the reconstitution of a smooth spectrum at the output, which cannot be achieved with incoherent spectral combining.

This can be shown using an illustration in Fig. 3.2(a), which depicts wavelength-dependent normalized transmission $T(\lambda)$ at a spectral edge of a filter. This edge can

represent, for example, a short-wavelength edge of LWP or BP filters, or, alternatively, a long-wavelength edge of BR filters. Insert in this figure illustrates use of the filter as a beam combiner, when the transmitted beam is overlapped spatially with the reflected beam thus producing an output consisting of both short-wavelength and long-wavelength portions of the input signals. Reversed propagation direction should be used for spectral beam splitting. For example, consider a beam incident from right-to-left with the wavelength-independent spectral intensity $I(\lambda) \equiv I_0$, then, since within the spectral edge region this filter acts as a wavelength-dependent $T(\lambda)$:(1-$T(\lambda)$) beam splitter, the transmitted and reflected wavelength-dependent beam intensities will be $T(\lambda)\cdot I_0$ and (1-$T(\lambda)$)$\cdot I_0$, respectively. Now let's consider an identical filter being used as a beam combiner for input beams with intensities I_1 and I_2 as shown in the insert. It is straightforward to find by direct calculation that, assuming both beams are in phase, the combining efficiency $\eta = I_{\text{combined}}/(I_1 + I_2)$ is

$$\eta = \frac{\left(\sqrt{I_1 \cdot T(\lambda)} + \sqrt{I_2 \cdot (1 - T(\lambda))}\right)^2}{I_1 + I_2}. \qquad (1)$$

If the recombined two beams are the same as the reflected and transmitted beams from the previously considered identical filter used as a beam splitter, i.e. $I_1 = T(\lambda)\cdot I_0$ and $I_2 = (1\text{-}T(\lambda))\cdot I_0$, then substitution into Eq. 1 yields η = 100% for all wavelengths. In other words, all incident power can be coherently spectrally recombined into a single beam without any power loss provided that a split-edge spectral shape is perfectly preserved between splitting and combining.

In practice preservation of such an ideally perfect spectral-edge-shape match between split and recombined signals might be challenging due to spectral gain reshaping in

individual fiber amplifiers of a parallel array. Using relatively steep spectral-edge dielectric coating filters can mitigate this. Alternatively, it can be bypassed altogether by resorting to non-overlapping spectra, in which case spectrally smooth recombined spectra cannot be achieved.

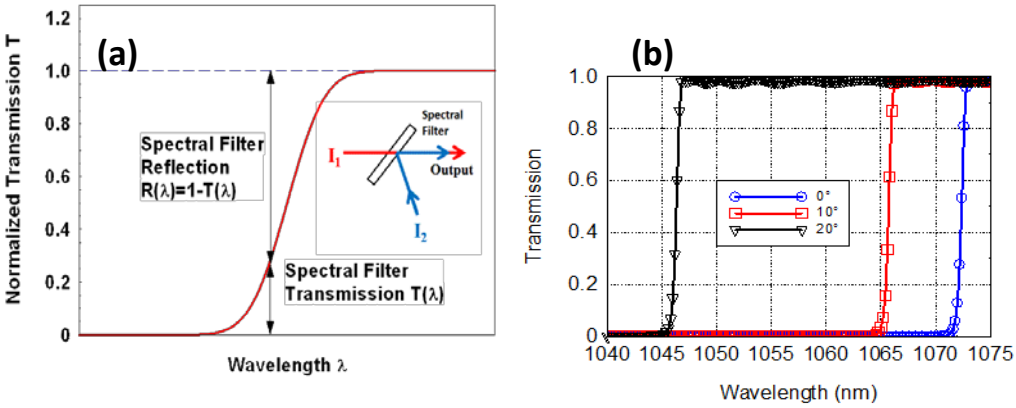

Fig. 3.2 (a) Wavelength-dependent normalized transmission T(λ) at a spectral edge of a filter. Normalization is with respect to the peak value of the filter's absolute transmission. (b) An example of spectral transmission characteristics of LWP filters used as spectral combiners. Three curves correspond to three different input-beam incidence angles, as indicated in the figure.

An example of spectral transmission characteristics of LWP filters (Semrock, LP02-1064RS-25) used as spectral combiners in the experiments reported in this work are shown in Fig. 3.2(b). The spectral-edge steepness of these filters is less than 1nm, and the spectral-edge wavelength can be adjusted by the input-beam angle of incidence as indicated in the figure.

3.2.3 Phase locking

Coherent phasing between all parallel amplification channels requires tracking and correcting phasing errors in each channel. In this work we are using the LOCSET coherent phasing scheme in which each channel is "tagged" by individual harmonic-modulation frequency imprinted through a phase modulator [10, 11], the same modulator

that is also used to correct the phase of the channel. Detection of individual-channel errors in this scheme is done with a single detector, in which each phase modulation frequency produces an identical-frequency electric current related to the magnitude of the corresponding-channel phase error. An electronic circuit connected to the detector recognizes each-channel phase error and applies the required-magnitude correction signal to the phase modulator in a corresponding channel.

LOCSET has been developed for conventional coherent phasing of spectrally identical parallel-channel signals, which are beam-combined at the system output interferometrically using some type of 50:50 beam splitters. This interference is what converts phase modulation in each channel into intensity modulation detected by the error-tracking detector. The main challenge in applying LOCSET to spectral-coherent combining is associated with the fact that the nature of spectral combining is non-interferometric, i.e. combined average power is independent of the relative phases between different-spectra signals, provided there is no spectral overlap between them. Interference can only occur in the regions of partial spectral overlap between the signals. Consequently, since in coherent spectral combining all channel spectra either do not overlap or overlap only weakly, a linear detector (i.e. a detector with an output signal *linearly* proportional to the incident power) at the combined output will respectively detect either no interference or only a weak interference signal. Therefore, linear detectors appear to be ineffective for phasing parallel channels in a coherently spectrally combined system.

As a result, it is necessary to devise a new phase-error detection approach, which is not based on combined-signal interference. Since the objective is to reconstitute from

parallel-channel spectral slices a bandwidth-limited combined pulse, it is natural to seek a detection scheme that would sense combined pulse peak power. This can be done by replacing a linear detector with a quadratic one, i.e. a detector with an output signal *quadratically* dependent on the incident peak power. We have implemented a quadratic detector by using a standard semiconductor diode specially selected so that the photon energy of ~1μm wavelength light falls well below its band edge. Consequently, the output signal of this detector is produced only by two-photon absorption (TPA), and is, therefore, proportional to the square of the peak power. Compatibility of a TPA detector with frequency tagging to track phase errors in the LOCSET scheme is shown in the Appendix of this chapter.

It is obvious that the highest TPA signal will occur for bandwidth-limited pulses, when all channels are in-phase, and the signal peak power is at its maximum. It is, however, far from obvious whether the TPA signal always increases with decreasing phase mismatch between the different channels. Indeed, changing phases between different spectral slices from different channels is equivalent to phase shaping the combined pulse. In principle, in a N-channel system there are N degrees of freedom in controlling pulse shape. This leads to a very complicated "landscape" of possible combined-waveform shapes, and to a very complex change in these shapes with decreasing phase "mismatch" between the channels. If the TPA signal would not always increase with decreasing phasing error then its use for phase correction feedback would be problematic.

In order to validate the suitability of a quadratic detector for implementing coherent phasing of a fiber amplifier array we have performed a numerical statistical study of the TPA signal dependence on inter-channel phasing error. This study shows that statistically

the TPA detector output always increases with a decrease in the overall phasing error, and, therefore, confirms that the quadratic detector should work with the LOCSET scheme. To show that, it is necessary to express the combined signal spectrum as a coherent sum of individual-channel spectral slices:

$$E_{comb.}^{\Sigma_k}(t) = \Im^{-1}\left[\mathcal{E}_{comb.}^{\Sigma_k}(\omega)\right] = \Im^{-1}\left[\sum_{j=1,N} \mathcal{E}_j(\omega)\cdot e^{i\phi_j}\right], \tag{2}$$

where each *j*-th channel has its individual phase ϕ_j. Here each *j*-th channel spectrum is $\mathcal{E}_j(\omega)$, the combined-signal spectrum is $\mathcal{E}_{comb.}^{\Sigma_k}(\omega)$, and the time-domain combined signal $E_{comb.}^{\Sigma_k}(t)$ is obtained by taking an inverse Fourier transform $\Im^{-1}$ of its spectrum. Symbol Σ_k in this expression is used to identify the particular combination $\{\phi_1, \phi_2, ..., \phi_j, ..., \phi_N\}$ of parallel-channel phases, and serves as a label to identify each time-domain signal shape corresponding to this inter-channel phase set. Each phase ϕ_j is determined by random variations in optical path length due to external factors (such as temperature variations, mechanical perturbations, etc.), and by the phase shifts produced deliberately by controlling phase modulators in each parallel path. The purpose for phase control electronics is to produce bandwidth-limited combined pulses at the system output by achieving $\phi_1 = \phi_2 = \ldots = \phi_j = \ldots = \phi_N$, i.e. all channels should be in phase.

The generation of carriers in a TPA detector is an instantaneous process, which is proportional to the square of the optical combined-signal irradiance. The TPA detector electric response, however, is much slower than the optical pulse repetition period (but is selected to be much faster than LOCSET modulation period). Therefore, the TPA

detector electric response $S_{TPA}^{\Sigma_k}$ is proportional to the time average of the optical combined-signal squared:

$$\left\langle S_{TPA}^{\Sigma_k}(t)\right\rangle \propto \left\langle \left[E_{TPA}^{\Sigma_k}(t)\cdot\left(E_{TPA}^{\Sigma_k}(t)\right)^*\right]^2\right\rangle. \tag{3}$$

Angle brackets here denote the time averaging operation, which in this case is over a time period longer than pulse repetition period but shorter than the shortest LOCSET modulation period. Symbol Σ_k indicates that the detected TPA electric signal magnitude depends on inter-channel phase set in the parallel-channel array.

The random variation in optical path length due to external factors is accounted by assigning the probability $p(\phi_j)$ with which each *j*-th channel phase magnitude ϕ_j occurs, and assuming that this probability distribution is described by a normal (Gaussian) distribution with its mean equal to zero and its variance equal to σ:

$$p(\phi_j)=\frac{1}{\sqrt{2\pi}\cdot\sigma}\cdot e^{-\frac{1}{2}\left(\frac{\phi_j}{\sigma}\right)^2}. \tag{4}$$

The variance σ is a measure of the magnitude of the overall inter-channel phasing error in the *N*-channel parallel-amplifier array. In simulations each set of random phases $\Sigma_k \equiv \{\phi_1,\phi_2,...,\phi_j,...,\phi_N\}$ is generated using a numerical random-number generator. Note that $0 \le \phi_j < 2\pi$. Since we are interested not in the absolute magnitude of the TPA electric signal but rather in its relative magnitude compared to the one produced by the bandwidth-limited (BL) pulse, we can calculate the normalized TPA signal $\eta_{TPA}^{\Sigma_k}$ as

$$\eta_{TPA}^{\Sigma_k} = \frac{\left\langle S_{TPA}^{\Sigma_k}(t) \right\rangle}{\left\langle S_{TPA}^{\mathrm{BL}}(t) \right\rangle}. \tag{5}$$

The magnitude of this normalized TPA signal is in the range $0 < \eta_{TPA}^{\Sigma_k} \leq 1$.

The statistical description of this normalized TPA response is achieved by running the $\eta_{TPA}^{\Sigma_k}$ calculations K times, each time with a different set of random phases $\Sigma_k \equiv \{\phi_1, \phi_2, ..., \phi_j, ..., \phi_N\}$, where k = 1, 2, …, K. All these random phase distributions Σ_k are calculated using the Gaussian probability distribution shown above, all with the same variance σ (i.e. the same overall inter-channel phasing error magnitude). Results of this statistical calculation can be cast as a histogram, with the horizontal axis representing TPA signal η_{TPA} and subdivided into M slots with the width $\Delta\eta = 1/M$ each, and the vertical axis representing the number of occurrences $L(\Delta\eta)$ that the calculated $\eta_{TPA}^{\Sigma_k}$ values fall into each interval $\Delta\eta_m = m \cdot \Delta\eta$ (m = 1, 2, …, M).

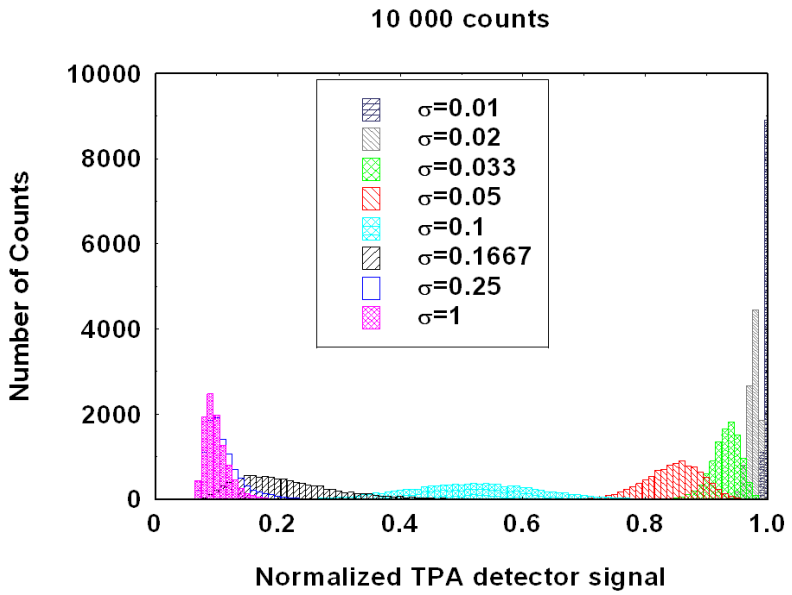

Fig. 3.3 Numerically simulated histograms of the statistics of the TPA responses for different overall inter-channel phasing-error magnitudes, as indicated by different values of variance σ.

One representative example of this statistical calculation is shown in Fig. 3.3. It shows calculated histograms of the statistics of the TPA responses for different overall inter-channel phasing-error magnitudes, as indicated by the different variance σ values shown in the figure. This particular calculation has been performed for 14-nm FWHM wide "flat top" spectrum, similar to the one used in actual experiments. The spectrum, however, was subdivided into 10 equal-width slots, which corresponds to a 10-channel array. To get reliable statistical distributions each $\eta_{TPA}^{\Sigma_k}$ calculation with each particular σ has been performed K = 10,000 times. Plotted results clearly show that the TPA electric-response signal *increases* with *decreasing* overall inter-channel phasing error σ.

3.3 Experimental setup

The experimental setup of 3-channel pulse synthesis is shown in Fig. 3.4. A femtosecond seed source from the Nd:glass oscillator (central wavelength at 1059 nm, 72 MHz repetition rate, 12 nm spectral width) generates pulses that are stretched by a conventional diffraction-grating stretcher to around 500 ps in duration and coupled into a fiber CPA system. The stretched pulses are split into 3 channels and proceed to delay lines. The delay lines are composed of non-reciprocal fiber circulators, micro-optic mirrors, and 4-nm bandwidth bandpass spectral filters (Semrock, LL01-1064-25). The first two are used to fine tune the delay within a range of 1 cm whereas the last one is placed in a free space portion to divide the channel spectra into distinct parts. The schematic of the delay line with a spectral filter and its 3D rendering is shown in Fig. 3.5.

When using a linear detector (Thorlabs, DET10A) for partial spectral overlap, we slightly overlap the spectra of adjacent channels so that without phase locking some

output power fluctuates due to random constructive and destructive interference from the common wavelength range, and thus can be used for feedback control. When using a TPA detector (Hamamatsu, G1735) for no spectral overlap, we just slice the spectra into three adjacent pieces with no spectral overlap.

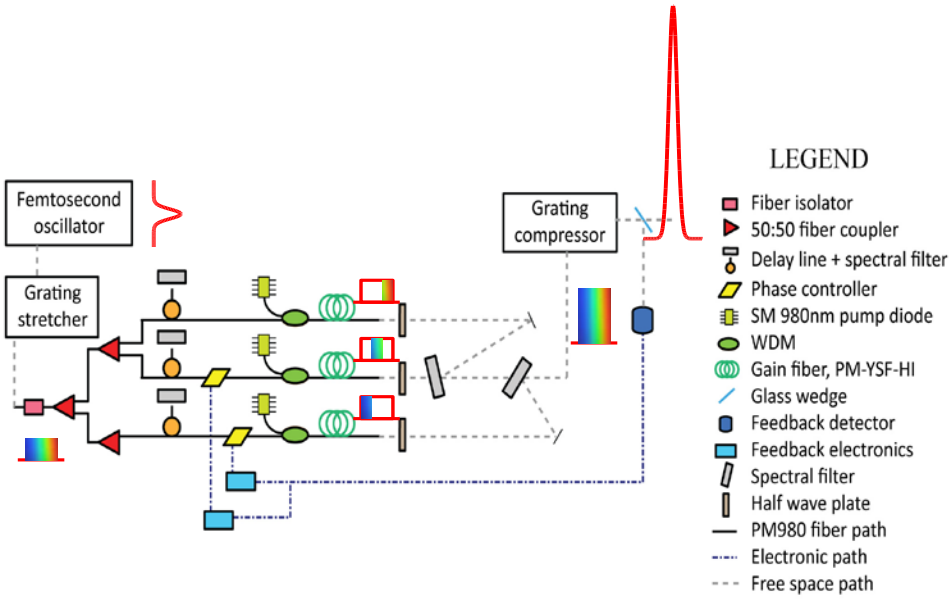

Fig. 3.4 Experimental setup for three-channel pulse synthesis.

After the delay line the pulses in two of three channels go to fiber piezo-stretchers (Optiphase, PZ1) for phase control. Following the piezo-stretchers the pulses are amplified with standard telecom grade single-mode pump diodes and PM fiber components. All three channels use identical in-fiber components to ensure the equal amount of linear and higher-order dispersion from these components in each channel. Moreover, each channel provides approximately 20-dB net gain in a fiber amplifier.

After amplification, the three separate channels are collimated out of the fibers into a free-space spectral combiner composed of two edge spectral filters (Semrock, LP02-1064RS-25). Note that each output from a single-mode fiber amplifier is diffraction-limited. Special care has been taken to ensure that a good spatial overlap between

combined beams has been achieved. For this purpose we use a single-mode test fiber positioned after the beam combining. Spatial overlap is evaluated by measuring and comparing coupling efficiencies for each individual channel and for the combined beam. At 75% coupling, the difference in these coupling efficiencies is only 2%, indicating a very good spatial overlap between the beams. The combined pulse is then recompressed with a diffraction grating compressor. A small portion of the compressed output power is detected by either the linear or TPA detector and served as a feedback signal with phase error information for two of three channels with respect to the reference channel. Through the self-referenced LOCSET technique [10,11] and two sets of feedback signal processing units, the phase error signal is individually extracted and sent to piezo-stretchers for phase compensation. A feedback loop that maximizes the linear or TPA intensity reinforces the channels to interfere constructively and hence locks the phases of the separate channels. In our experiment, the combining efficiency is defined as the combined power at the output of spectral combiner divided by the sum of each individual input power of spectral combiner. Therefore, it refers to "absolute" combining efficiency.

In the feedback system, the piezo-stretcher can provide a π phase shift per 2.6 V driving voltage and can be driven up to ±500 V equivalent to 384π continuous phase control. Our feedback electronics is limited to an output of ±5 V (3.8π). To attain long-time stable locking, we use the high-voltage amplifiers to reach at least ±100 V (76π). Moreover, the noise regime of our environment associated with acoustic vibrations and temperature drift is below 1 kHz [4]. We choose RF modulation/demodulation frequencies at 5 kHz and 6 kHz to be fast enough to detect the phase drift as well as to be slower than the repetition rate (72 MHz) of the oscillator to maintain the validity of self-

referenced LOCSET technique. The integration time of the feedback electronics is set to 50 msec to cancel phase disturbances up to 20 Hz in frequency and the phase modulation amplitude β is set to 0.25 to provide stable locking.

Owing to two different off-the-shelf types of spectral filters for splitting and combining the spectra, it is inevitable to consider their steepness mismatch. To achieve the best combining efficiency for partial spectral overlap, we adjust bandpass and edge filters to let any two adjacent spectra overlap the minimal detectable range so that phase locking can still be fulfilled as well as minimizing the power loss.

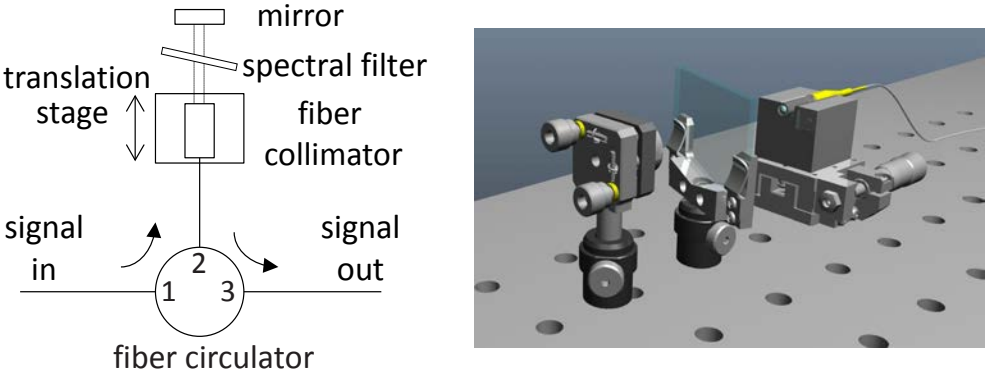

Fig. 3.5 Schematic and 3D rendering of the micro-optic delay line with spectral filter.

3.4 Experimental results

The objective of the proof-of-the-principle experiment was to demonstrate synthesis of coherently spectrally combined pulses with the combined-pulse durations much shorter than that from each individual channel, and to characterize the combined and synthesized pulse temporal quality. We explored two different coherent spectral combining cases: one with partially overlapping spectra, and another with separated non-overlapping spectra.

Experimental results for the partially overlapping case are shown in Fig. 3.6. As is apparent from Fig. 3.6(a), each individual channel spectra are roughly triangular with

approximately 3-nm bandwidth, as determined by the spectral-edge steepness of the filters used in the experiment. Overlap between any two adjacent individual spectra was set to be approximately 1nm. The full-width-half-maximum (FWHM) of the combined spectrum is 8 nm. Due to the partial spectral overlap it was possible to use in this case both linear and TPA detectors for tracking inter-channel phasing errors. The measured background-free SHG autocorrelation traces of individual-channel and combined signals are shown as solid lines in Fig. 3.6(b). For reference we also show in this figure the calculated autocorrelation trace (dash line) of the bandwidth-limited pulse obtained from the measured combined spectrum (red line) from Fig. 3.6(a). The measured autocorrelation trace durations of individual-channel and combined pulses are 1328 fsec (829 fsec), 1368 fsec (777 fsec), 1501 fsec (871 fsec), and 547 fsec (403 fsec) respectively, with the the corresponding deconvolved pulse durations given in parentheses. These results clearly show that the combined pulse is approximately 2 to 3 times shorter than each individual-channel pulse. Comparison between the measured and calculated autocorrelation traces indicates that the combined pulse duration of 403 fsec is slightly longer than the calculated transform-limited 363 fsec duration, and the measured trace has long wings, which are absent in the calculated trace. We identified that this difference is caused by some residual third-order dispersion uncompensated in the system. The absolute combining efficiency and combined power are measured to be 76.3% and 257 mW respectively. Since the spectral combiner has intrinsic loss from each edge filter with 95% transmission and 99.7% reflection, it gives 94.9% spectral filter efficiency in a 3-channel setup. The additional 18.6% efficiency loss in this experiment was from the slope mismatch between the bandpass and edge filters in each channel.

Experimental results for non-overlapping spectra are shown in Fig. 3.7. In this case phasing between the channels was achievable only with the TPA detector. Fig. 3.7(a) shows individual-channel and combined spectra. The FWHM of the combined spectrum spans approximately 10 nm and is comprised from 3 nearly identical triangular-shaped individual spectra. The measured autocorrelation traces are shown in Fig. 3.7(b) by solid lines, and the dashed line shows the calculated transform-limited trace of the combined spectrum. Corresponding autocorrelation-trace and deconvolved pulse (shown in parentheses) durations for individual-channel and combined pulses are 1700 fsec (1071 fsec), 1420 fsec (761 fsec), 1327 fsec (834 fsec), and 474 fsec (356 fsec). The combined pulse width in this case is also approximately 2 to 3 times shorter than each individual-channel ones, and longer than the calculated transform-limited 278 fsec duration. Note, however, that in this case the satellite structure appears in the wings of both the measured as well as the calculated bandwidth-limited traces of the combined pulses, with wings in the measured trace still being noticeably larger than in the calculated trace. The later is still caused by the uncompensated third-order dispersion in the system. The satellites in the combined pulse appear due to the strongly modulated profile of the combined spectrum, produced by the triangular shape and large separation between individual channel spectra. The absolute combining efficiency and combined power are measured to be 85.8% and 273 mW respectively. With 94.9% spectral filter efficiency, the 9.1% additional loss corresponds to efficiency loss from the some spectral mismatch between signal splitting and combining arrangements. Note that the small overlap in Fig. 3.7 does not capture the fact that there was a much more significant mismatch between spectral characteristics of the spectral splitters and combiners used in this experiment. In both

partial overlapping and non-overlapping cases, the autocorrelation traces were very stable in time, as indicated by the fact the autocorrelation trace from a phase-locked array observed on an oscilloscope screen was not changing in time.

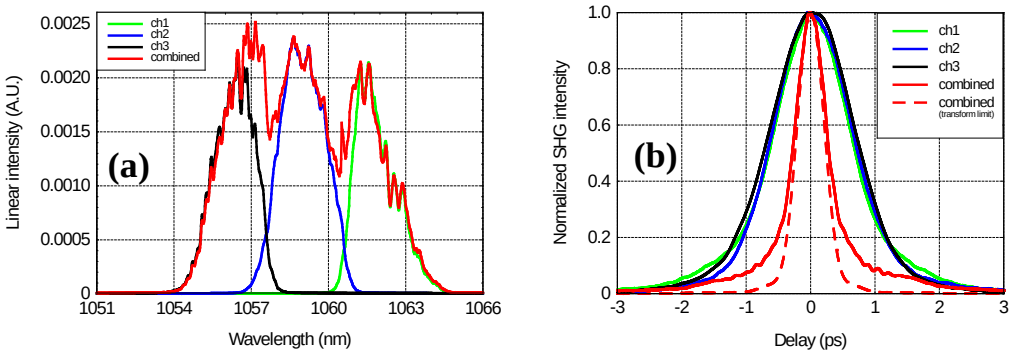

Fig. 3.6 Results for that case of partially overlapping spectra. (a) Measured spectra of the individual-channel and combined signals; (b) normalized autocorrelation traces for the individual-channel and combined signals. The dash line shows the calculated transform-limited autocorrelation of the combined spectrum in (a).

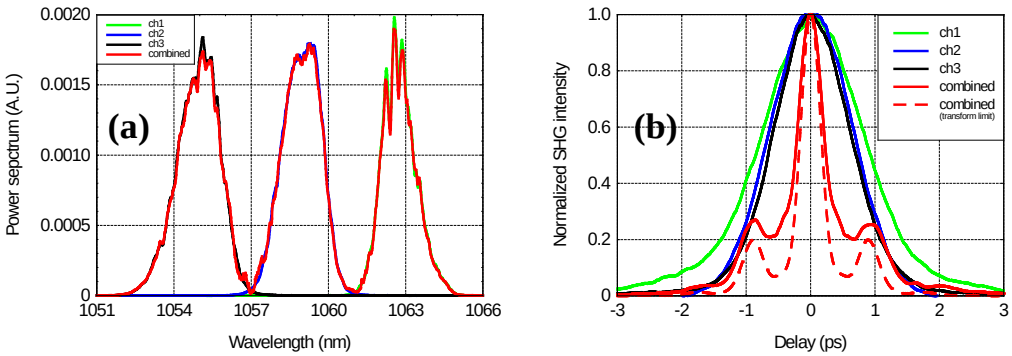

Fig. 3.7 Results for the case of non-overlapping spectra. (a) Spectra for the individual-channel and combined signals; (b) normalized autocorrelation traces for the individual-channel and combined signals. The dash line shows the calculated transform-limited autocorrelation of the combined spectrum in (a).

Phase locking results for the two cases are shown in Fig. 3.8. Fig. 3.8(a) shows phase–error tracking detector output for the configuration with partial spectral overlap. For this particular measurement a linear detector has been used. Fig. 3.8(b) shows TPA detector output for the configuration with non-overlapping spectra. Both figures compare results for locked and free running operation. As one can see from these figures stable phase locking has been achieved in both cases and with both detectors (as indicated by red lines

in the figures). Note that for free running operation (blue lines) in both cases phase tracking detector output fluctuates, as expected. However, the span of these fluctuations does not reach zero for reasons that are very different for each of the two cases. In Fig 3.8(a) fluctuations measured with linear detector are due to the interference in the spectrally overlapped regions. Since the fraction of the power in these overlapped regions is small compared to the total power, fluctuation amplitude is only a small fraction of the detector output voltage. In Fig. 3.8(b) fluctuations measured with TPA detector are due to peak intensity variation in the combined signal. In this case, although the detector operates at frequencies below its absorption bandgap and in principle should only detect the two-photon signal, there is still a small residual linear absorption which produces a background signal comparable to the TPA signal magnitude. Moreover, the TPA signal in a free-running system should not go to zero even in the absence of residual linear absorption, when the background signal would be comprised only of the sum of the individual-channel TPA signals. This background signal is constant both for locked and free running operation.

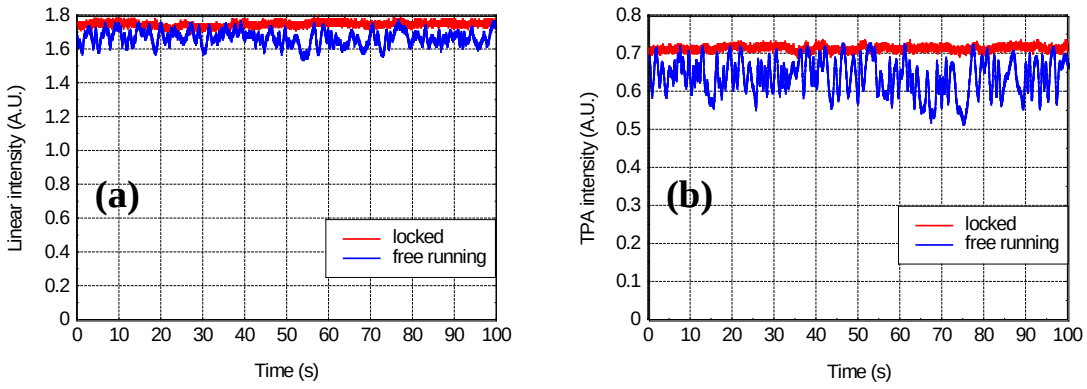

Fig. 3.8 Locked and unlocked intensity variations measured using (a) the linear detector in a system with partial spectral overlap between the channels, and (b) the TPA detector in a system without any spectral overlap between the channels.

3.5 Discussion and summary

These experimental results show that, since coherent spectral combining of ultrashort pulses essentially constitutes a signal synthesis, combined-pulse temporal shape very strongly depends on individual-channel spectra. Generation of background-free pulses requires smooth combined spectrum, which can be achieved using partially overlapping individual-channel spectra. Combining of separate, non-overlapping individual-channel spectra leads to significantly structured combined-pulse background. In addition, controlling the phase between the channels can be used to shape the temporal profile of the combined signal.

To summarize, we had demonstrated coherent spectral combining of femtosecond optical pulses from multiple parallel fiber CPA channels. This technique enables ultrashort pulse amplification with an aggregate spectrum significantly exceeding amplification bandwidths of each individual amplifier, as well as allows scaling average power and pulse energy beyond single fiber limitations. Potentially, this technique could lead to fiber laser sources of tens of femtosecond duration multi-mJ pulses with high average powers.

3.6 Appendix

Here we evaluate the two-photon-absorption (TPA) phase error signal under the LOCSET scheme. The total electric field in the time domain from a system using self-referenced LOCSET technique [10,11] can be written as

$$E_T(t) = E_1 \cos(\omega_L t + \phi_1) + \sum_{i=2}^{N} E_i \cos(\omega_L t + \phi_i + \beta_i \sin(\omega_i t)), \tag{A1}$$

where N is the total number of elements, E_1 and E_i are the field amplitudes for the unmodulated and i^{th} phase modulated elements, ϕ_1 and ϕ_i are optical phases, ω_L is the laser frequency, ω_i is an RF modulation frequency, and β_i is a phase modulation amplitude.

Since the optical fields from the unmodulated element and all of the phase modulated elements are superimposed on the photodetector, the TPA photodetector current is

$$\begin{aligned} i_{TPA}(t) &= qP_T^2 \\ &= qA^2 \frac{\varepsilon_0}{\mu_0} |E_T|^4, \end{aligned} \tag{A2}$$

where ε_0 and μ_0 are the electric and magnetic permeabilities of free space, A is the photodetector area, and q is the responsivity of the TPA photodetector.

The phase error signal is extracted from the TPA photocurrent using coherent demodulation in the RF domain. The TPA photocurrent is multiplied by $\sin(\omega_i t)$ and integrated over a time T that is larger than the optical period ($2\pi/\omega_L$) but smaller than any of the modulation periods ($2\pi/\omega_i$). Then, the phase error signal for the i^{th} element is given by

$$S_i = \frac{1}{T} \int_0^T i_{TPA}(t) \cdot \sin(\omega_i t) dt. \tag{A3}$$

Using the Fourier series expansions

$$\cos(\beta_i \sin(\omega_i t)) = J_0(\beta_i) + 2\sum_{n=1}^{\infty} J_{2n}(\beta_i) \cdot \cos(2n\omega_i t),$$
$$\sin(\beta_i \sin(\omega_i t)) = 2\sum_{n=1}^{\infty} J_{2n-1}(\beta_i) \cdot \sin(2(n-1)\omega_i t), \tag{A4}$$

where J_n is a Bessel function of order n of the first kind, and neglecting the oscillating terms at optical frequencies since the detector is slow to rewrite the terms in Eq. (A1), then we can substitute Eq. (A1) into Eq. (A2) and calculate the phase error signal from Eq. (A3) to give

$$S_i = qA^2 \frac{\varepsilon_0}{\mu_0} \cdot \left\{ \begin{array}{l} \frac{1}{2}E_i^2 \left(\sum_{\substack{j=2 \\ j\neq i}}^{N} E_j \right)^2 \cos(\phi_i - \phi_j)\sin(\phi_i - \phi_j) J_0(\beta_i) J_1(\beta_i) \left(2\sum_{n=1}^{\infty} J_{2n-1}^2(\beta_j) - \left(J_0^2(\beta_j) + 2\sum_{n=1}^{\infty} J_{2n}^2(\beta_j) \right) \right) \\ -\frac{1}{2}E_i^3 \left(\sum_{\substack{j=2 \\ j\neq i}}^{N} E_j \right) \sin(\phi_i - \phi_j) J_1(\beta_i) J_0(\beta_j) \\ +2E_1^2 E_i^2 \cos(\phi_i - \phi_1)\sin(\phi_i - \phi_1) J_0(\beta_i) J_1(\beta_i) \\ -\frac{1}{2}E_1^2 E_i \left(\sum_{\substack{j=2 \\ j\neq i}}^{N} E_j \right) \sin(\phi_i - \phi_j) J_1(\beta_i) J_0(\beta_j) + E_1^3 E_i \sin(\phi_i - \phi_1) J_1(\beta_i) \\ +E_1 E_i^2 \sum_{\substack{j=2 \\ j\neq i}}^{N} E_j \left[\cos(\phi_i - \phi_j)\sin(\phi_i - \phi_1) - \cos(\phi_i - \phi_1)\sin(\phi_i - \phi_j) \right] J_0(\beta_i) J_1(\beta_i) J_0(\beta_j) \\ +E_1 E_i^3 \sin(\phi_i - \phi_j) J_1(\beta_i) \end{array} \right\}. \tag{A5}$$

From the complicated Eq. (A5), one can conclude specific phase error signal is extracted when specific demodulation frequency is implemented so that each modulated element has its own specific phase error signal without confusion with other elements. Moreover, Eq. (A5) is nonzero under the free-running operation except when the system is phase-locked, $\phi_i=\phi_j$ ($i, j=1, 2,...N$), then $\cos(\phi_i-\phi_j)=1$, $\sin(\phi_i-\phi_j)=0$, and thus $S_i=0$.

If TPA photocurrent is demodulated by $\sin(\omega_k t)$, where ω_k is different from the tagging modulation frequency ω_i, then

$$\begin{aligned}\frac{1}{T}\int_0^T \cos(\beta_i \sin(\omega_i t))\cdot\sin(\omega_k t)dt &= \frac{1}{T}\int_0^T \cos^2(\beta_i \sin(\omega_i t))\cdot\sin(\omega_k t)dt = 0\\ \frac{1}{T}\int_0^T \sin(\beta_i \sin(\omega_i t))\cdot\sin(\omega_k t)dt &= \frac{1}{T}\int_0^T \sin^2(\beta_i \sin(\omega_i t))\cdot\sin(\omega_k t)dt = 0,\end{aligned} \tag{A6}$$

one can expect

$$S_{k,i} = \frac{1}{T}\int_0^T i_{TPA}(t)\cdot\sin(\omega_k t)dt = 0. \tag{A7}$$

This is due to the orthogonality of Fourier series for different frequencies over an integration of a time period T. With $S_i \neq 0$ and $S_{k,i}=0$, one can summarize TPA provides with the correct "frequency tagged" signal for the LOCSET-scheme phase error signal detection.

3.7 References

1. D. J. Richardson, J. Nilsson, and W. A. Clarkson, "High power fiber lasers: current status and future perspective," J. Opt. Soc. Am. B **27**, B63-B92 (2010)

2. T. Eidam, S. Hanf, E. Seise, T.V. Andersen, T. Gabler, C. Wirth, T. Schreiber, J. Limpert, and A. Tünnermann, , "Femtosecond fiber CPA system emitting 830W average output power," Opt. Lett. **35**, 94-96 (2010)

3. F. Röser, T. Eidam, J. Rothhardt, O. Schmidt, D. N. Schimpf, J. Limpert, and A. Tünnermann, "Millijoule pulse energy high repetition rate femtosecond fiber chirped-pulse amplification system," Opt. Lett. **32**, 3495-3497 (2007)

4. L. A. Siiman, W. Z. Chang, T. Zhou, and A. Galvanauskas, "Coherent femtosecond pulse combining and scalability of multiple parallel chirped pulse fiber amplifiers," Opt. Express **20**, 18097-18116 (2012).

5. A. Klenke, E. Seise, S. Demmler, J. Rothhardt, S. Breitkopf, J. Limpert, and A. Tünnermann, "Coherently-combined two channel femtosecond fiber CPA system producing 3 mJ pulse energy," Opt. Express **19**, 24280-24285 (2011)

6. L. Daniault, M. Hanna, L. Lombard, Y. Zaouter, E. Mottay, D. Goular, P. Bourdon, F. Druon, and P. Georges, "Coherent beam combining of two femtosecond fiber chirped-pulse amplifiers," Opt. Lett. **36**, 621-623 (2011)

7. R. K. Shelton, L. S. Ma, H. C. Kapteyn, M. M. Murnane, J. L. Hall, and J. Ye, "Phase-coherent optical pulse synthesis from separate femtosecond lasers," Science **293**, 1286-1289 (2001)

8. G. Krauss, S. Lohss, T. Hanke, A. Sell, S. Eggert, R. Huber, and A. Leitenstorfer, "Synthesis of a single cycle of light with compact erbium-doped fibre technology," Nature Photon. **4**, 33-36 (2010)

9. S. W. Huang, G. Cirmi, J. Moses, K. H. Hong, S. Bhardwaj, J. R. Birge, L. J. Chen, E. Li, B. J. Eggleton, G. Cerullo, and F. X. Kartner, "High-energy pulse synthesis with sub-cycle waveform control for strong-field physics," Nature Photon. **5**, 475-479 (2011)

10. T. M. Shay, "Theory of electronically phased coherent beam combination without a reference beam," Opt. Express **14**, 12188-12195 (2006)

11. T. M. Shay, V. Benham, A. D. Sanchez, D. Pilkington, and C. A. Lu, "Self-synchronous and self-referenced coherent beam combination for large optical arrays," IEEE J. Sel. Top. Quant. **13**, 480-486 (2007)

12. T. Y. Fan, "Laser beam combining for high-power, high-radiance sources," IEEE J. Sel. Top. Quantum Electron. **11**, 567-577 (2005)

13. T. H. Loftus, A. Liu, P. R. Hoffman, A. M. Thomas, M. Norsen, R. Royse, and E. Honea, "522 W average power, spectrally beam-combined fiber laser with near-diffraction-limited beam quality," Opt. Lett. **32**, 349-351 (2007)

14. O. Andrusyak, V. Smirnov, G. Venus, N. Vorobiev, and L. Glebov, "Applications of volume Bragg gratings for spectral control and beam combining of high power fiber lasers," SPIE **7195**, 71951Q (2009)

15. K. Regelskis, K. Hou, G. Raciukaitis, and A. Galvanauskas, "Spatial-dispersion-free spectral beam combining of high power pulsed Yb-doped fiber lasers," CLEO, CMA4(2008)

Chapter 4

Coherent pulse stacking amplification using low-finesse Gires-Tournois interferometers (Time domain)

4.1 Introduction

Peak power limitations associated with detrimental nonlinear effects and optical damage in an optical amplifier constitute the most important constraints on achievable energies of short optical pulses. This is particularly true for optical fiber amplifiers, which are characterized by a relatively small guided-mode area and long propagation lengths of amplified signals. The chirped pulse amplification (CPA) technique alleviates this limitation by stretching broadband ultrashort pulses prior to amplification by a factor of up to 10^3 - 10^4 times [1], and compressing them afterwards, thus enabling the increase in achievable pulse energy by a similar factor. However, the maximum stretched pulse duration is limited to approximately 1-2 ns by practical constraints on the compressor and stretcher grating size and cost, which establishes a limitation on the achievable pulse energy by the CPA method. For example, in Yb-doped fiber amplifiers the achievable pulse energy using CPA is smaller than the stored energy by more than an order of magnitude [2], even when using very large diffraction grating stretchers and compressors [3]. Recently a divided pulse amplification (DPA) technique has been proposed and demonstrated as a CPA extension to increase the amplified pulse duration by another

factor of a few times [4,5], by splitting and delaying stretched pulse replicas in spatially arranged delay lines, amplifying the pulses, and recombining them through constructive interference in a similar spatial arrangement. The delay between pulse replicas is directly determined by the spatial length of each delay line, which increases exponentially with the number N of used delay lines as 2^N , and therefore constitutes a constraint on the achievable pulse "multiplication" factors.

Here we propose and demonstrate a new approach to effectively extend the amplified pulse duration in which a sequence of pulses generated directly from a laser oscillator is amplified and coherently stacked into a single pulse at the system output using resonant reflecting cavities. This coherent pulse stacking (CPS) essentially constitutes a signal synthesis technique, where a suitable phase and amplitude coding/modulation is imprinted onto the initial pulse train to first store it as a single pulse in an optical resonator by destructive interference at its output port, and subsequently to switch it out as a single output pulse by constructive interference at this port induced by the final pulse of the input sequence. The main distinction of this technique is that, unlike CPA or DPA techniques, it does not require initial pulse splitting or stretching in a spatial arrangement, but rather produces the required signal directly from an oscillator-modulators system, which when built using fiber optics, can comprise a monolithically-integrated circuitry. This also allows the generation of any arbitrary temporal profile of individual pulses and of the overall pulse sequence, so that amplitude (as well as phase) distortions due to energy saturation and nonlinear effects could be pre-compensated with respect to the systems output, thus enabling very high pulse stacking efficiencies even at maximum energies. Furthermore, the use of resonator cavities instead of delay lines can produce

large delays using small-footprint arrangements, which is an important practical feature. Note also that this technique is distinct from coherent pulse stacking using pulse dumping from high-finesse resonant enhancement cavities [6,7]. Since no active cavity-dumping elements are used, CPS with resonant reflecting cavities is not subjected to any pulse energy and efficiency limitations due to active beam-modulating elements.

In this chapter we report a proof-of-the-principle demonstration of this CPS technique using a single reflecting resonant cavity, in which the theoretically predicted stacking performance in terms of peak-power enhancement, satellite-pulse contrast and stacking efficiency has been achieved. We also show theoretically that large numbers of equal-amplitude pulses can be stacked using various sequences of multiple reflecting resonators. Future development of this technique to multiple stacking cavities could enable very high enhancement factors, and thus a complete extraction of the stored pulse energy from fiber CPA systems with negligible nonlinearity-induced distortions.

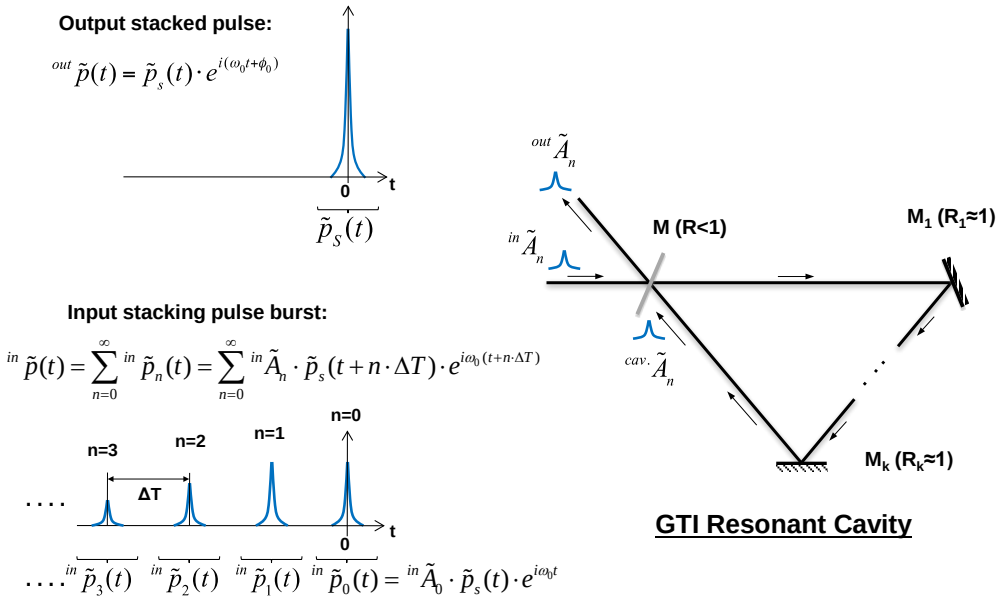

Fig. 4.1 Coherent pulse stacking in a traveling-wave Gires-Tournois interferometer, showing the stacking-signal pulse sequence at its input and the stacked solitary pulse at its output.

4.2 Theoretical description of coherent pulse stacking with a single Gires-Tournois Interferometer

This section provides a detailed theoretical description of coherent pulse stacking with a single Gires-Tournois Interferometer, the requirements for a stacking cavity and input pulse burst parameters, and of the main performance characteristics.

4.2.1 Reflecting resonant cavity

A reflecting interferometer can be configured either as a linear or a traveling-wave cavity. A linear reflecting cavity is essentially a Fabry-Perot interferometer with one completely reflecting mirror, which is commonly referred to as a Gires-Tournois interferometer (GTI). The practical advantage of a traveling–wave reflecting cavity, shown in Fig. 4.1, is that it allows one to spatially separate the incident input and reflected output beams. For usage convenience we will also refer to this traveling-wave cavity as a GTI. Let's consider a traveling–wave GTI cavity, consisting of a partially reflecting front-mirror M (with power reflectivity $R = r^2 < 1$), and K completely reflecting beam-folding mirrors M_1, M_2, …, M_K, schematically shown in Fig. 4.1. Ideally we should have $R_k = 1$ for all $k = 1, 2, \ldots K$, but in practice it will always be $R_k \approx 1$. We can denote the round-trip cavity transmission as $\alpha = r_1 \cdot r_2 \cdot \ldots r_K$, where r_k is the corresponding k-th mirror amplitude reflection coefficient. Then $\alpha^2 = R_1 \cdot R_2 \cdot \ldots R_K$ describes power loss per round trip due to the finite reflectivity of the folding mirrors. If the round trip distance in this traveling-wave cavity is P, then the round trip time is $\Delta T = P/c$ (here c is the speed of light), and the round-trip phase is $\delta = 2\pi P/\lambda_0 = \omega_0 \cdot \Delta T$ (here λ_0 and ω_0 are, respectively, the signal

central wavelength and angular frequency). We can describe electric field transmission through this cavity by a transmission matrix [*T*]:

$$[T] = \begin{bmatrix} 1 & 0 \\ 0 & \alpha \cdot e^{i\delta} \end{bmatrix}. \tag{1}$$

The incident and reflected fields at both sides of the front mirror M can be described by a unitary scattering matrix [S], which can be written in a symmetric form [8]:

$$[S] = \begin{bmatrix} r & it \\ it & r \end{bmatrix}. \tag{2}$$

Here *r* is the front mirror amplitude reflection and *t* its amplitude transmission coefficient, which for a lossless (and reciprocal) dielectric mirror are related by $t^2 = 1 - r^2$, with both *r* and *t* being real quantities [8]. Usage of these matrices in describing the stacking cavity is given at the end of the next section.

4.2.2 Incident, output, and circulating fields in a GTI cavity

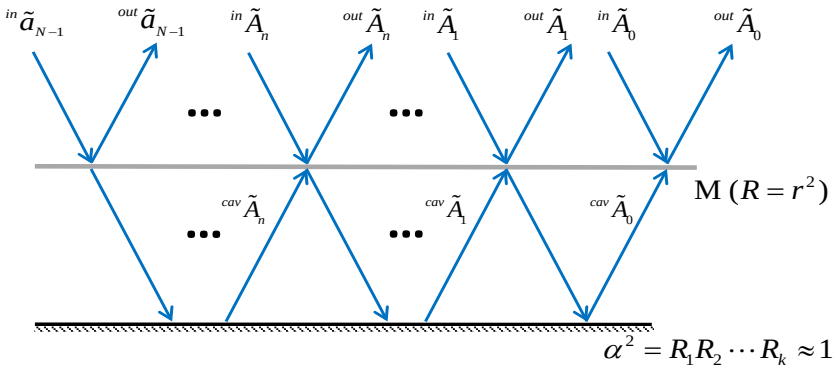

Fig. 4.2 Amplitudes of all incident, in-cavity circulating, and output pulses in a conceptualized 2-mirror GTI cavity.

Let's assume that all pulses at the input, output and circulating inside of a GTI cavity have identical complex envelopes $\tilde{p}_s(t)$, where complex notation accounts for the fact that stacking can be achieved with bandwidth-limited (described by real envelopes

$\tilde{p}_s(t) \equiv p_s(t)$) as well as with chirped (described by complex envelopes $\tilde{p}_s(t)$) pulses. As illustrated in Fig. 4.1, we seek to convert an input pulse burst ${}^{in}\tilde{p}(t)$ into a single output "stacked" pulse:

$$ {}^{in}\tilde{p}(t) = \sum_j {}^{in}\tilde{p}_j(t) \rightarrow {}^{out}\tilde{p}(t) = \tilde{p}_s(t) \cdot e^{i(\omega_0 t + \phi_0)}. \tag{3} $$

Let's choose the time axis reference such that this output stacked pulse is centered at $t = 0$. Then we can enumerate all the pulses in the incident train as

$$ {}^{in}\tilde{p}(t) = \sum_{n=0}^{\infty} {}^{in}\tilde{p}_n(t) = \sum_{n=0}^{\infty} {}^{in}\tilde{A}_n \cdot \tilde{p}_s(t + n \cdot \Delta T) \cdot e^{i\omega_0 (t + n \cdot \Delta T)}, \tag{4} $$

so that $n = 0$ corresponds to the pulse at $t = 0$ and $n = 1,2,\ldots$ are at correspondingly increasing separations $n \cdot \Delta T$ at negative t values, as shown in Fig. 4.1. Here ${}^{in}\tilde{A}_n = {}^{in}A_n \cdot e^{i\phi_n}$ is the complex amplitude characterizing the amplitude and phase of the n^{th} individual pulse ${}^{in}\tilde{p}_n(t)$ of the semi-infinite input pulse burst. The pulse repetition period ΔT should be equal to the cavity round trip time ΔT, since interference at the front mirror M occurs only when the incident pulse and the circulating in-cavity pulse arrive at that mirror simultaneously. As shown in Fig. 4.2, let's denote the amplitude of the circulating pulse arriving at the front mirror M from inside the cavity simultaneously with the ${}^{in}\tilde{A}_n$ input pulse as ${}^{cav.}\tilde{A}_n$. Interference at the front mirror M between these two simultaneously incident pulses ${}^{in}\tilde{A}_n$ and ${}^{cav.}\tilde{A}_n$ produces a "reflected" output pulse with an amplitude ${}^{out}\tilde{A}_n$ and a "transmitted" in-cavity pulse, which after passing mirrors M_1 through M_K arrives at M as a subsequent circulating pulse ${}^{cav.}\tilde{A}_{n-1}$. Amplitudes of all incident, in-cavity circulating, and output pulses are shown in Fig. 4.2 for a

conceptualized 2-mirror GTI cavity. Using the front-mirror scattering matrix [*S*] given by the Eq. (2), and the cavity transmission matrix [*T*] given by the Eq. (1) we can describe this interference (plus a subsequent round trip) using the following matrix equation:

$$\begin{bmatrix} {}^{out}\tilde{A}_n \\ {}^{cav.}\tilde{A}_{n-1} \end{bmatrix} = \begin{bmatrix} 1 & 0 \\ 0 & \alpha \cdot e^{i\delta} \end{bmatrix} \cdot \begin{bmatrix} r & it \\ it & r \end{bmatrix} \cdot \begin{bmatrix} {}^{in}\tilde{A}_n \\ {}^{cav.}\tilde{A}_n \end{bmatrix}, \tag{5}$$

for each $n = 0, 1, 2, \ldots$.

4.2.3 Conditions for coherent pulse stacking

Ideally, when coherent pulse stacking is achieved then ${}^{out}\tilde{A}_0 = 1$ and ${}^{out}\tilde{A}_n = 0$ for all $n > 0$. This means that for all incident pulses prior to the last pulse (i.e. $n > 0$), totally destructive interference between the incident and circulating pulses should eliminate all reflections from the front mirror, thus storing all incident pulses as a single circulating pulse inside the cavity. For the last incident pulse ($n = 0$) totally constructive interference in the reflection direction of that mirror should combine the incident and circulating pulses into a single output pulse, thus extracting all stored circulating energy. Additionally, it is ${}^{cav.}\tilde{A}_n = 0$ and ${}^{out}\tilde{A}_n = 0$ for all n < 0, since ideally there should be no field left in the cavity after the last $n = 0$ pulse has passed. Using Eq. (5) above, we can express all these conditions mathematically as:

$$\begin{bmatrix} 1 \\ 0 \end{bmatrix} = \begin{bmatrix} 1 & 0 \\ 0 & \alpha \cdot e^{i\delta} \end{bmatrix} \cdot \begin{bmatrix} r & it \\ it & r \end{bmatrix} \cdot \begin{bmatrix} {}^{in}\tilde{A}_0 \\ {}^{cav.}\tilde{A}_0 \end{bmatrix}, \text{ for } n = 0, \tag{6}$$

and

$$\begin{bmatrix} 0 \\ {}^{cav.}\tilde{A}_{n-1} \end{bmatrix} = \begin{bmatrix} 1 & 0 \\ 0 & \alpha \cdot e^{i\delta} \end{bmatrix} \cdot \begin{bmatrix} r & it \\ it & r \end{bmatrix} \cdot \begin{bmatrix} {}^{in}\tilde{A}_n \\ {}^{cav.}\tilde{A}_n \end{bmatrix}, \text{ for } n = 1, 2, \ldots \infty. \tag{7}$$

By solving the linear-equation sets Eq. (6) and, iteratively, Eq. (7), we get all the complex amplitudes of the pulses in the semi-infinite train at the cavity input, and of the corresponding circulating pulses inside the cavity:

$$\begin{cases} {}^{in}\tilde{A}_0 = r \\ {}^{in}\tilde{A}_n = -(1-r^2)\cdot r^{n-1}\cdot\dfrac{e^{-in\delta}}{\alpha^n}, \quad for\ \ n=1,2,3,...\infty \\ {}^{cav.}\tilde{A}_n = -it\left(\dfrac{r}{\alpha\cdot e^{i\delta}}\right)^n, \qquad for\ \ n=0,1,2,...\infty \end{cases} \tag{8}$$

Correspondingly, the peak power coefficients ${}^{in}B_n = \left|{}^{in}\tilde{A}_n\right|^2$ of the incident pulses are:

$$\begin{cases} {}^{in}B_0 = R \\ {}^{in}B_n = \dfrac{(1-R)^2 R^{n-1}}{(\alpha^2)^n}, \quad for\ n=1,2,3,...\infty \end{cases} \tag{9}$$

Note that by defining the output stacked pulse using Eq. (3) we chose its peak power coefficient to be normalized to 1: ${}^{out}B_0 = 1$. In an ideal case, when amplitudes of all the pulses in the semi-infinite input train fulfill the Eq. (8), then all other output pulses are absent, i.e. ${}^{out}B_n = 0$ for all $n \neq 0$. According to Eq. (8), if the GTI cavity round trip phase is chosen to be $\delta = 2\pi m$ (where m is an integer) then the last pulse in the input sequence is out of phase with respect to the rest of the pulses in the sequence. It is easy to recognize from Eq. (9) that the peak powers of all the pulses in the input sequence prior to the last pulse (i.e. n = 1,2, …) are described by a decreasing geometrical progression.

4.2.4 Finite-length input pulse sequences

Eq. (8) and (9) describe an ideal semi-infinite input pulse sequence, when the only output is the stacked pulse. In practice one needs to truncate this semi-infinite pulse train into a finite pulse burst consisting of *N* pulses. As it is shown in Appendix A, the last N-1 pulses in this finite sequence ${}^{in}\tilde{A}_0$, …, ${}^{in}\tilde{A}_{N-2}$ remain the same as prescribed by Eq. (8), and it is only the amplitude of the first input pulse ${}^{in}\tilde{A}_{N-1}$ that needs to be replaced by ${}^{in}\tilde{a}_{N-1} = \frac{{}^{in}\tilde{A}_{N-1}}{1-R}$. This is to accommodate the fact that there is no pulse in the cavity to interfere with when this first pulse arrives. Consequentially, this first input pulse always produces a reflected pre-pulse at the output. This first-pulse reflection, however, can always be made arbitrarily small by increasing the length *N* of the incident pulse burst, since, as shown by Eq. (22) in the Appendix A, the reflected pre-pulse amplitude ${}^{out}\tilde{a}_{N-1}$ is geometrically decreasing with *N*.

4.2.5 Peak-power enhancement with a GTI cavity

This coherent stacking of multiple pulses into one output pulse containing all the energy of the input pulse sequence is beneficial when amplifying high energy pulses in, e.g. a fiber amplifier, since it enables the amplification of pulses with lower peak powers, thus reducing the detrimental nonlinear effects in an amplifier. This benefit is proportional to the peak-power enhancement factor

$$\eta = {}^{out}B_0 \,/\, {}^{\max}\left\{{}^{in}B_n\right\} = 1 \,/\, {}^{\max}\left\{{}^{in}B_n\right\}, \tag{10}$$

where ${}^{\max}\left\{{}^{in}B_n\right\}$ denotes the highest peak-power coefficient in the incident pulse sequence. One can maximize this peak-power enhancement factor by selecting GTI

parameters, which minimize the magnitude of $^{\max}\left\{ {}^{in}B_n \right\}$. By inspecting Eq. (9) it is straightforward to recognize that $^{\max}\eta$ is achieved when $^{in}B_0 = {}^{in}B_1$. This condition defines the optimum front-mirror reflectivity R_{opt} of a GTI cavity:

$$^{in}B_0 = {}^{in}B_1 \rightarrow R_{opt} = \frac{(1-R_{opt})^2}{\alpha^2} \rightarrow R_{opt}^2 - (2+\alpha^2)R_{opt} + 1 = 0.$$

The solution of this quadratic algebraic equation, corresponding to a physically meaningful power reflectivity in the range $0 \le R \le 1$, is

$$R_{opt} = \frac{(2+\alpha^2) - \sqrt{(2+\alpha^2)^2 - 4}}{2}. \tag{11}$$

The corresponding $^{\max}\eta$ is

$$^{\max}\eta = \frac{1}{R_{opt}} = \frac{\alpha^2}{(1-R_{opt})^2}. \tag{12}$$

For an ideal case when $\alpha^2 = 1$ (all folding mirrors are perfectly reflecting) we have $R_{\text{opt}} = 0.382$, and the corresponding highest possible peak-power enhancement for a single GTI cavity of $^{\max}\eta = 2.62$.

4.2.6 Energy efficiency of a GTI pulse stacker

It is important to know the pulse energy losses in a GTI pulse stacker, which can be characterized by its energy efficiency defined as the ratio χ between the energy of a stacked output pulse $\varepsilon_{\text{stck.}}$ and the total energy of an incident pulse train ε_{in}: $\chi = \varepsilon_{\text{stck.}}/\varepsilon_{\text{in}}$. This accounts for the effects of cavity losses α^2 on an ideally stacked (i.e. pre-pulse free) output pulse. Detailed analysis for both semi-infinite and finite pulse sequences is

presented in Appendix B. Here we give only the main result - energy efficiency χ_N for a finite N-pulse input burst:

$$\chi_N{}^{-1} = \frac{1-R(2-\alpha^2)}{\alpha^2-R} + \left(\frac{R}{\alpha^2}\right)^{N-1} \frac{\alpha^2(2-R)-1}{\alpha^2-R}. \tag{13}$$

We also found that for all practically relevant cases of relatively low cavity loss of $\alpha^2 >$ 89%, the energy efficiency for a semi-infinite sequence can be approximated by $\chi_\infty \approx \alpha^2$.

4.3 Experimental demonstration of coherent pulse stacking amplification with a single GTI cavity

This section describes the coherent pulse stacking demonstration experiments, and includes an experimental setup description, an analysis of signal source and stacking-cavity stability requirements, and a review of achieved stacking results with their comparison to theoretical predictions.

4.3.1 Experimental setup

Two types of proof of the principle demonstrations of the coherent pulse stacking are presented here: one is a nanosecond pulse amplification experiment using a high-coherence CW laser seed, and the other is a femtosecond CPA experiment using a mode-locked laser seed. Both experiments share mostly the same experimental setup outlined in black color in Fig. 4.3, which implements the coherent pulse stacking amplification. This CPS amplification arrangement consists of two parallel signal-preparation and amplification channels, a GTI-cavity based pulse stacker, and also includes stacker-cavity monitoring and stabilization electronics. One channel is for preparing and amplifying the pulsed signal that is being stacked (stacking-signal channel), and the other is for

preparing and amplifying the monitor signal used for tracking and stabilizing the stacker-cavity length to ensure coherent pulse stacking (monitor-signal channel). Differences between the two experimental arrangements are outlined in Fig. 4.3 in blue and red colors respectively for ns and fs pulses, and consist of different seed sources, the presence of a pulse stretcher and a compressor for the CPA experiment, use of different-reflectivity mirrors M_1 in the GTI cavity, and replacing mirror M_2 from a flat mirror in the nanosecond experiment to a curved mirror in the femtosecond experiment.

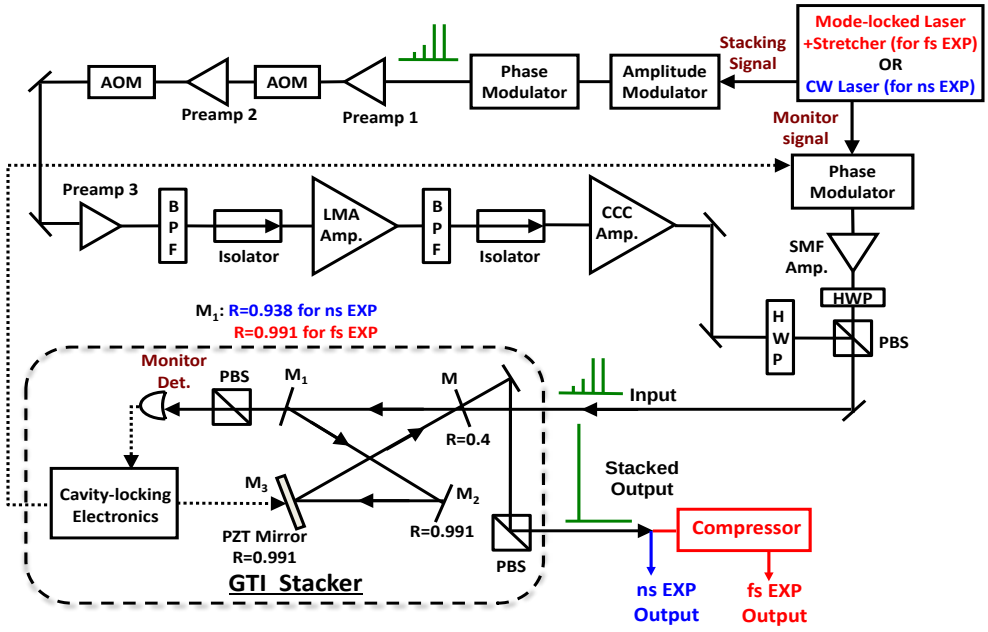

Fig. 4.3 Experimental coherent pulse stacking amplification system. fs EXP: femtosecond experiment; ns EXP: nanosecond experiment; BPF: band-pass filter; HWP: half-wave plate; SMF Amp.: single-mode fiber amplifier; LMA Amp.: large-mode-area fiber amplifier; CCC Amp.: chirally-coupled-core fiber amplifier.

The CW seed source for the nanosecond experiment is a Toptica DL 100 tunable single-frequency diode laser set to produce a 45 mW output beam at 1064 nm. An optical isolator (>35 dB) is placed between the oscillator and the subsequent CPS arrangement to prevent any optical feedback into the oscillator, and thus to ensure narrow-linewidth operation, which is required for implementing CPS (as explained in detail in Subsection

4.3.2). Nanosecond pulses in a burst prepared for stacking in a GTI cavity are "carved-out" from this CW signal at the beginning of the stacking-signal channel, as described later in the text. For the femtosecond experiment a mode-locked oscillator and a subsequent grating stretcher are used as a seed source. The mode-locked laser operates at 1054 nm central wavelength, producing 300 fs bandwidth-limited pulses with 4.5 nm FWHM spectral width (with approximately Gaussian spectrum) at 122 MHz repetition rate, with 30 mW average power. The diffraction-grating based pulse stretcher is arranged in a standard Martinez-type configuration, and it stretches output pulses from the mode-locked oscillator to a pulse width of ~600 ps. At the input of the CPS amplification arrangement, the output beam from each corresponding seed source is coupled into a polarization-maintaining (PM) single-mode fiber (SMF), and is then split into the two parallel channels by a 50:50 PM single-mode fiber splitter.

In the stacking-signal channel the signal from a seed source is first reshaped, and then amplified in a five-cascade fiber amplifier chain. The primary purpose of the seed-signal reshaping is to produce a sequence of pulses where each pulse is properly amplitude and phase modulated, as prescribed by Eq. (8), so that this prepared pulse burst can be stacked in the GTI cavity at the system output. This reshaping is performed in a sequence of two fiber-coupled electro-optic (EO) lithium niobate ($LiNbO_3$) amplitude and phase modulators, with 10 GHz bandwidth each. Each of the two modulators are controlled by a computer-controlled 12-bit and 4.0 GigaSamples/sec Arbitrary Waveform Generator (AWG), providing full flexibility in controlling amplitudes, phases, and even shapes of individual pulses in the stacking burst. For the nanosecond experiment the stacking pulse burst is carved out of the CW signal input. In this case the broad bandwidth of the EO-

modulators and the high speed of the AWG enable generation of sub-nanosecond individual pulses with ~160 ps rise and fall times, separated by 5 ns (i.e. corresponding to 200 MHz repetition rate). For the femtosecond experiment the stacking pulse burst is carved out of a periodic (122 MHz repetition rate) stretched-pulse train from the mode-locked oscillator and the grating stretcher, so that only amplitudes and phases of individual pulses in the burst are controlled. Flexibility of this pulse-burst control arrangement allows the generation of stacking pulse bursts, and the corresponding stacked pulses at the system output, at an arbitrarily selectable repetition rate in the range from <1 kHz to a few MHz. This arrangement also allows the pre-compensation of pulse burst amplitude and phase distortions due to energy saturation and non-linear effects in the stacking-signal channel, providing a very useful feature for this CPS technique.

As shown schematically in Fig. 4.3, the Yb-doped fiber amplifier chain in the stacking-signal channel consists of three single-mode PM-fiber pre-amplifiers, followed by two large-core power amplifier stages. Each of the three SMF pre-amplifier stages is pumped by standard telecom-grade single-mode pump diodes, and there are two acousto-optic modulators (AOM) inserted between them. These modulators serve as optical gates primarily to suppress the unwanted amplified spontaneous emission (ASE) background between low-repetition pulse bursts. They also can be used to additionally down-count pulse bursts, if needed for achieving optimized amplifier performance. Details of each SMF amplifier stage are not shown here. The first power amplifier is a co-pumped monolithically-integrated module based on a standard 25 μm large-mode-area (LMA) fiber. Two band-pass filters (BPF) tuned to 1064 nm with a bandwidth of 4 nm are inserted before and after this stage to filter out the ASE background in the power

amplifier stage. The final amplifier is a counter-pumped high-energy stage based on 55 μm chirally-coupled-core (CCC) Yb-doped double-clad fiber [9], in which stacking pulse bursts can be boosted to up to 1.2 mJ per burst, with the corresponding average power of ~12 W at 10 kHz burst repetition rate, limited by the applied pump power.

In the monitor-signal channel the signal from a seed source, which is a continuous wave for the nanosecond experiment and a 122 MHz repetition rate stretched-pulse train for the femtosecond experiment, is first phase modulated in a PM-fiber pigtailed electro-optic $LiNbO_3$ phase modulator, and then amplified in a standard single-mode PM fiber amplifier. Phase modulation with a 5 MHz sinusoidal waveform is applied to implement the stabilization of the GTI-stacker cavity length by locking it to the monitor-signal carrier frequency, as discussed later in the text. This modulated monitor signal is amplified to ~100 mW to provide a sufficient power for reliable monitor-signal detection and demodulation, after picking it up as leakage through the GTI-cavity mirror M_1.

The stacking-signal and the monitor-signal beams at the output of each respective channel are spatially combined into one beam, which is then launched into the GTI stacker. Since each of the two output beams is linearly polarized, they are spatially combined using two half-wave plates and a polarizing beam splitter (PBS), as shown in Fig. 4.3. Consequentially, both the stacking and the monitor signals share the GTI cavity. At the GTI output the residual monitor signal was stripped from the beam using another PBS, as shown in Fig. 4.3, thus producing a “clean” beam containing only the stacked pulse signal. Additionally, a PBS was used at the monitor-signal detection port after the mirror M_1 to separate the leaking monitor signal from the stacking-signal “background” thus reducing detection noise.

The GTI-stacker cavity consists of a partially-reflecting front mirror M with a reflectivity R = 40%, and three high-reflectivity cavity folding mirrors M_1, M_2, and M_3. The reflectivity of mirrors M_2 and M_3 is fixed in both experiments to $R_2 = R_3$ = 99.1%, but the reflectivity of mirror M_1 is different for the nanosecond (R_1 = 93.8%) and the femtosecond (R_1 = 99.1%) experiments. This difference is used to verify the relation between cavity transmission and stacker efficiency described by Eq. (25) and Eq. (26). GTI-cavity length adjustment is done using mirror M_3, which is mounted on a PZT-controlled mount. Mirrors M, M_1, and M_3 are flat in all experiments, while mirror M_2 is flat in the nanosecond experiment, but curved (with a focal length of 1.5 m) in the femtosecond experiment. Ideally, the reflected input beam and the transmitted in-cavity beam should perfectly overlap in position and direction at the cavity front mirror M, so that their interference can produce a single output beam. For this to happen, beam sizes and wavefront curvatures at the mirror M must perfectly match. In practice, when all four cavity mirrors are flat, sufficient spatial matching is achieved using a suitably large incident beam. When a curved mirror is used in the femtosecond experiment to construct a stable cavity, the incident beam must be mode-matched to the cavity mode.

Finally the stacked solitary chirped pulse output from the GTI stacker in the femtosecond experiment is compressed into a solitary femtosecond pulse by a standard Treacy-type diffraction-grating compressor.

4.3.2 Signal and GTI cavity stability requirements for coherent pulse stacking

Because coherent pulse stacking in a GTI cavity is achieved by the interference between all individual pulses in the incident pulse burst, it is imperative that there should be negligible random phase fluctuations among the pulses $\Delta\varphi_n << \pi$, as well as a negligible

random variation of the GTI-cavity round-trip phase $\Delta\delta(t) << \pi$. Causes of random phase variations between incident pulses $\Delta\varphi_n$ are associated with the phase noise present in the seed source, as well as the phase noise that could be imprinted by optical modulators when the signal is transmitted through an optical amplification channel. Random variation of the round-trip phase $\Delta\delta(t)$ is associated with the drift of the GTI cavity length due to mechanical and thermal perturbations. One has to ensure that random phase variations are negligible by either selecting suitable optical components and their operation conditions, or, if necessary, by using feedback-controlling stabilization. It is helpful to recognize that, according to Eq. (8), phase noise contributions $\Delta\varphi_n$ by the oscillator and $\Delta\delta(t)$ by the GTI cavity to coherent pulse stacking are completely equivalent, and therefore both can be treated as one "general" random phase variation Δ. To ensure coherent pulse stacking, it is necessary to determine how small these random phase variations Δ should be.

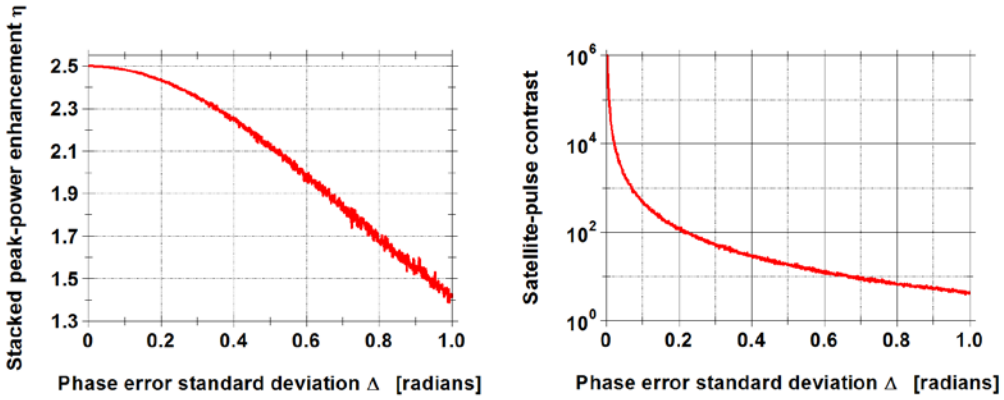

Fig. 4.4 Peak-power enhancement η and satellite-pulse contrast γ vs the phase error of the input pulse burst.

Numerically calculated dependencies of the two key CPS characteristics, peak power enhancement factor η and satellite-pulse contrast ratio γ, vs random phase variation standard deviation Δ are plotted in Fig. 4.4. Here the peak power enhancement factor η is

defined in Eq. (10) as the pulse peak power ratio between the output stacked pulse and the most intense input pulse, and the satellite-pulse contrast ratio is defined as the peak power ratio between the output stacked pulse and its pre-pulse: $\gamma = {}^{out}B_0/{}^{out}B_1$, where ${}^{out}B_0$ and ${}^{out}B_1$ are peak power coefficients of the output pulses defined in Subsection 4.2.3, and ${}^{out}B_1$ is typically the highest pulse peak power among all the residual pre-pulses. In the simulation we assume that every pulse in the burst has random phase errors described by a Gaussian normal distribution with mean 0 and a standard deviation Δ. The peak powers of the 1^{st} output pulse (pre-pulse) and the 0^{th} output pulse (stacked pulse) are recorded and averaged over 1000 iterations (corresponding to a 1000 sequential pulse bursts), and then used to calculate the averaged satellite-pulse contrast γ and the averaged enhancement η. Numerical simulation results from Fig. 4.4 show that, for example, maintaining satellite-pulse contrast γ better than 20 dB and peak-power enhancement η higher than 97% of η^{max} requires keeping the phase noise Δ lower than 0.2 radians, or, equivalently, the phase error should be less than $\lambda/30$.

These results can be used to determine the phase-noise requirements for a seed-signal source of a CPS amplification system. Seed requirements are defined somewhat differently for nanosecond and femtosecond sources. One way to ensure that phase errors in a stacking nanosecond-pulse burst are negligible is to select a seed source with its temporal coherence time τ_c sufficiently long compared to the pulse burst duration τ_b. For example, in a nanosecond CPS experiment reported here we used a single-frequency CW laser with a linewidth Δf < 1MHz followed by a fast electro-optic modulator producing nanosecond pulse bursts for coherent stacking with a pulse burst duration τ_b = 25 ns. Therefore, the coherence time of this CW laser is $\tau_c \approx 1/\Delta f$ > 1 μs, which is more than 30

times longer than the pulse burst duration τ_b, and consequently the resulting inter-pulse phase errors $\Delta\varphi_n$ are smaller than $\lambda/30$. For a mode-locked source of periodic ultrashort pulses, pulse-to-pulse phase as well as amplitude noise is determined by the spectral linewidth Δf_c of the frequency-comb lines constituting the spectrum of such a periodic signal [10]: significant phase and amplitude variations build-up over time τ_c proportional to the inverse of this spectral linewidth $\tau_c \approx 1/\Delta f_c$. The frequency-comb linewidth Δf_c is primarily determined by the magnitude and characteristic speed of mechanical and thermal perturbations present in the cavity of a mode-locked laser, and even for a typical free-running (i.e. without stabilization) laser cavity is quite narrow: $\Delta f_c < 1$ kHz [11]. The corresponding $\tau_c > 1$ ms is more than four orders of magnitude larger than the pulse burst duration $\tau_b = 36$ ns used in the femtosecond experiment, which is more than sufficient for implementing coherent pulse stacking. This also indicates that CPS of much longer pulse bursts of 100 ns to 1 μs in duration would also be compatible with seeding from a free-running mode-locked oscillator.

Let's now consider the GTI stacker phase contribution δ in more detail. The GTI cavity round-trip frequency is $f_{cav} = 1/\Delta T = c/P$. For an incident signal with its carrier frequency $\omega_0 = 2\pi \cdot f_0$ the resulting GTI-stacker phase is $\delta = \omega_0 \cdot \Delta T = \omega_0/f_{cav} = 2\pi \cdot f_0/f_{cav} = 2\pi \cdot P/\lambda_0$, where λ_0 is the signal carrier wavelength $f_0 = c/\lambda_0$. We can express the cavity round-trip distance P in terms of the signal carrier wavelength as $P = m \cdot \lambda_0 + \Delta P/\lambda_0$, where m is an integer denoting the number of wavelengths "fitting" into the cavity, and the residual fractional cavity-length "mismatch" is $\Delta P < \lambda_0$. Then the cavity phase can be rewritten as $\delta = 2\pi \cdot (m + \Delta P/\lambda_0)$. Since according to Eq. (8) the in-burst phase modulation

φ_n remains identical for every consecutive burst only if the GTI stacker phase δ is not changing in time, it is necessary to lock the GTI cavity round-trip length P with respect to the carrier wavelength λ_0 so that the ratio $\Delta P/\lambda_0$ is kept constant. According to Fig. 4.4, precision and stability of this locking should be such that the random drift error $\Delta\delta(t)$ should be smaller than $2\pi/30$. Such a precise locking can be achieved using the Pound–Drever–Hall (PDH) locking technique [12]. Details of the optical set-up arrangements for implementing it are given in the corresponding experimental description presented in Subsection 4.3.1. What is important here is that the PDH locking is implemented by taking a fraction of the initial seed-laser output, phase-modulating it with a 5 MHz sinusoidal waveform, amplifying it, and then using it as a cavity-length monitor. This monitor signal is a narrow-linewidth CW signal for the nanosecond, and an unmodified "original" mode-locked train for the femtosecond experiments. The GTI-cavity length is monitored by detecting leakage of the monitor signal through the mirror M_1, and controlled by sending the detected signal into the feedback system for demodulation and then producing a cavity-length error signal which is used to correct the cavity length by adjusting the PZT-controlled mirror M_3. Since the mirror M_1 has a finite reflectivity R_1 (R_1 = 93.8% in the nanosecond and R_1 = 99.1% in the femtosecond experiments), the monitor-signal transmission has the spectrum of a low-finesse Fabry-Perot cavity, with a free-spectral range equal to f_{cav}, and transmission maxima occurring at $\delta = 2\pi \cdot m$. The error signal in the Pound–Drever–Hall scheme maximizes this transmission, thus setting the fractional cavity-length "mismatch" to $\Delta P = 0$, and stabilizing the GTI cavity length at the round-trip phase $\delta = 0$.

Coherent pulse stacking requires good temporal overlapping of the pulses when interfering, thus it is required that the in-burst pulse repetition frequency f_r should closely match the stacker round-trip frequency f_{cav}. However, a perfect match is difficult to achieve. Indeed, we can express the carrier frequency in terms of the pulse repetition frequency as $f_0 = q \cdot f_r + f_{CE}$, where q is an integer. Here f_{CE} accounts for a carrier-envelope phase (CEP) mismatch [13]. On the other hand, when the stacker is locked to this carrier and $\Delta P = 0$ is achieved then we have $f_0 = m \cdot f_{cav}$. Thus f_r and f_{cav} are best matched when the GTI cavity is adjusted to get $q = m$. But as long as $f_{CE} > 0$ these two frequencies are always slightly mismatched. Consequentially, during pulse stacking there is a small but finite timing error stemming from the slight discrepancy between the pulse separation $\Delta T_r = 1/f_r$ in the incident burst and the "stacking delay" equal to the round-trip duration ΔT of the GTI cavity: $\Delta t = \Delta T_r - \Delta T$. It is straightforward to see that this timing error between subsequent pulses is always smaller than one optical cycle $\Delta t < 1/f_0$. Therefore, when implementing CPS with relatively long pulses this timing error is practically negligible.

It is also important to consider phase contributions that might be introduced by acousto-optic modulators, which are often used as optical gates for pulse down-counting and ASE suppression in a pulsed fiber amplifier. An AOM uses an RF-driven moving sound wave to produce Bragg diffraction of the optical wave, and consequentially imprints a frequency up- or down-shift onto the $+1^{st}$ or -1^{st} diffraction-order [14]. This frequency shift is equal to the RF-driver frequency, which we can denote as an angular frequency Ω, and which typically is in the approximate frequency range of 50 MHz < $\Omega/2\pi$ < 200 MHz. The effect of this frequency shift can be represented as a phase shift of

$|\Delta\varphi| = \Omega \cdot \Delta T_r$ between subsequent pulses, or, equivalently, as a corresponding linear phase ramp imprinted on the input pulse burst. This phase ramp can be compensated by either choosing $\Omega/2\pi = f_r$, or, if there is an even number of identical AOM gates in the system, by arranging sequential pairs to operate in opposite diffraction orders ($+1^{st}$ and -1^{st}) so that their corresponding phase ramps cancel each other. Additionally, applying the conjugate phase ramp to the pulse burst using the phase modulator at the system input can also compensate this AOM-shift ramp.

Note that an electro-optic amplitude modulator in the stacking-signal channel can in general imprint additional amplitude-dependent inter-pulse phases on the optical pulse burst going through it [15]. We choose the EOM in our experiment to be arranged as a push-pull Mach-Zehnder interferometer, which is free from such parasitic amplitude-dependent phase effects [15].

4.3.3 Experimental results

The stacking pulse burst in the nanosecond experiment is generated using the amplitude modulator at the beginning of the stacking-signal channel to carve out the injected CW seed signal into five 850-picosecond-long pulses separated by a 5 ns period. The corresponding in-burst repetition rate is equal to 200 MHz. These bursts are generated at a 7.81 MHz inter-burst repetition rate, which is afterwards down-counted twice by the two AOMs in the stacking-signal channel to 10 kHz. Relative peak powers of the generated pulses are selected such that the amplitudes of the amplified in-burst pulses at the output of the channel obey Eq. (8) for the 5-pulse stacking signal sequence. In the experiment this is achieved by observing the pulse burst incident into the GTI stacker and adjusting the AWG control signal into the amplitude EOM as needed, which

automatically compensates gain saturation effects in the amplifier. An example of such a measured stacking pulse burst is shown in Fig. 4.5. The amplitude modulation at the channel input is followed by a phase modulation to imprint the stacking pulse-phase pattern also prescribed by Eq. (8). Since, as described in Subsection 4.3.2, the GTI cavity round-trip phase in our experiments is set to $\delta = 2\pi m$, coherent stacking requires that the first four pulses in the burst are in-phase, and the last pulse in the sequence is out of phase with respect to the others. This is achieved by imprinting phases $\varphi_n = 0$ for the first pulses with $n = 4, 3, 2, 1$, and $\varphi_0 = \pi$ for the last pulse.

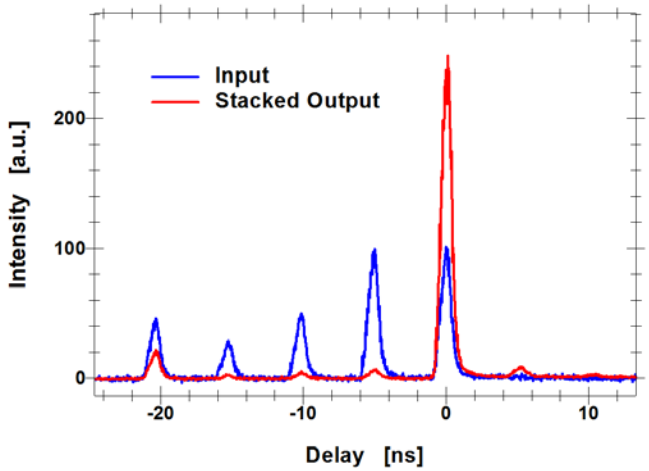

Fig. 4.5 Nanosecond experiment: the input pulse burst and output stacked pulse.

Experimental results of the nanosecond pulse stacking experiment are presented in Fig. 4.5, where the measured incident stacking pulse burst is shown in blue, and the output stacked pulse in red. The achieved peak-power enhancement factor η is 2.48 times, measured as the ratio between the peak power of the stacked pulse at the GTI output and that of the two last equal-amplitude pulses in the stacking sequence at the GTI input. Another important stacking performance metric is the residual magnitude of the pre-pulses, preceding the stacked pulse at the output, which shows how well destructive

interference at the stacker output prevents leakage of the pulses stored in the GTI cavity. In the results shown in Fig. 4.5 the measured satellite-pulse contrast γ is 16.2 dB, defined in Subsection 4.3.2 as the peak power ratio between the output stacked pulse and its pre-pulse. Note that for this metric one should discount the very first pre-pulse in the stacked output, since it is caused by the unavoidable but relatively weak reflection of the first input-burst pulse with the amplitude ${}^{out}\tilde{a}_{N-1}$ given by Eq. (22). As it is discussed in Subsection 4.2.4 and Appendix A, this first reflection can be made arbitrarily small by increasing the length N of the incident pulse burst. For example, for the 5-pulse stacking burst used in this experiment this first-reflection magnitude is $8 \cdot 10^{-2}$ of the stacked pulse peak power, but for achieving this magnitude smaller than 10^{-3} one needs to use 9 or more pulses in the stacking sequence. The stacking efficiency is 92%, measured as the ratio between the total energy of the GTI stacker output and that of the stacking-burst input. Note that the measured stacked output energy includes reflection of the first input-burst pulse as well as all residual pre-pulses, which are indistinguishable from the stacked main pulse when measured with an integrating power meter. Therefore, the measured stacking efficiency is somewhat different from the one defined by Eq. (13), where the first-pulse reflection is ignored. However, it is straightforward to show that this experimentally-measured efficiency $\chi_{\exp}$ is related to the one defined by Eq. (13) through

$$\chi_{\exp} = \chi_N \bullet [1 + (\frac{R}{\alpha^2})^{N-1}]. \qquad (14)$$

It is useful to compare these measured stacking characteristics with the theoretical predictions from Section 4.2. The end mirrors used in the GTI cavity in this experiment, M_1 at 93.8%, M_2 and M_3 both at 99.1%, produce a cavity round-trip energy transmission

of α^2 = 0.92. According to Eq. (11), the corresponding optimum front-mirror reflectivity is R_{opt} = 39.6%, very close to the R = 40% actually used. According to Eq. (12), the theoretical maximum possible stacked peak-power enhancement for α^2 = 0.92 and R_{opt} = 39.6% is ${}^{max}\eta$ = 2.52, which is close to the experimentally measured value of 2.48. Using Eq. (13) for the N = 5 pulse sequence for this GTI cavity we calculate the theoretical stacking efficiency of χ_N = 89%, which after using the earlier described correction in Eq. (14) considering the first-pulse reflection leads to a theoretically predicted χ_{exp} = 92%, practically the same as the measured stacking efficiency.

The experimental result shown in Fig. 4.5 is measured with a stacking-burst energy of up to 0.1 mJ, corresponding to up to 1W of average power at a 10 kHz inter-burst repetition rate. With further increase in the burst energy beyond this level we observe that CPS performance starts degrading in terms of enhancement and satellite-pulse contrast (stacking efficiency is not sensitive to pulse energy). For example, at 0.7 mJ of stacking-burst energy, the peak-power enhancement η decreases to 2, and the satellite-pulse contrast γ degrades to 8.5 dB. This is primarily caused by nonlinear self-phase modulation occurring in the fiber amplifier at high in-burst peak powers, which induces amplitude-dependent inter-pulse phase shifts in addition to the inter-pulse phases prescribed by Eq. (8), and thus perturbs the stacking process. In principle, this nonlinear phase modulation can be pre-compensated with the phase modulator at the input of the stacking-signal channel. In this initial proof-of-the-principle experiment, however, we have not done that, because each pulse in the stack is approximately Gaussian shaped rather than flat-top shaped, thus requiring phase corrections both between and inside the pulses, a sophistication that will be explored in subsequent experiments.

In the femtosecond experiment, the input stacking pulse bursts are produced from a mode-locked train of stretched pulses, each 600 ps long, and separated by an 8.2 ns period corresponding to the in-burst repetition rate of 122 MHz. The same pair of amplitude and phase modulators at the input of the stacking-signal channel is used to modulate this train according to the same prescription of Eq. (8) as in the nanosecond experiment to generate a 5-pulse stacking pulse burst. The same inter-burst repetition rate of 7.81 MHz, and the same subsequent down-counting to 10 kHz are chosen. The stacking pulse burst measured at the GTI input is shown as the blue trace in Fig. 4.6. The same as in the nanosecond experiment, a π phase shift is applied to every final pulse in each incident burst. The chirped stacked output pulse from the stabilized GTI cavity is shown in Fig. 4.6 as the red trace. From this trace a stacked peak-power enhancement of 2.56 and a satellite-pulse contrast of 15 dB are measured. Additionally, the measured stacking efficiency is 97.4%.

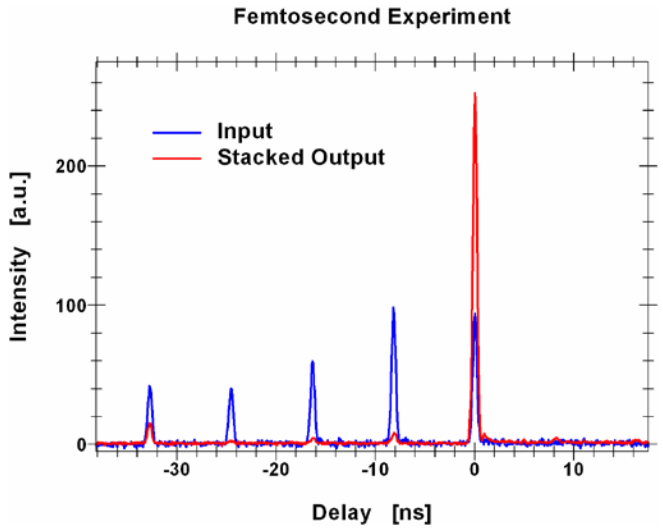

Fig. 4.6 Femtosecond experiment: the input pulse burst and output stacked pulse.

Just as in the nanosecond experiment, the measured stacking performance characteristics agree well with the theoretical predictions. In the femtosecond experiment

the reflectivity of mirrors M_1, M_2 and M_3 are all equal to 99.1%, and the front mirror M reflectivity is the same 40% as used in the nanosecond experiment. Consequently the cavity round-trip energy transmission is α^2 = 0.973, the corresponding optimum front-mirror reflectivity given by Eq. (11) is R_{opt} = 38.66%, and the theoretical highest possible peak-power enhancement given by Eq. (12) is $^{max}\eta$ = 2.586, which indeed is very close to the measured enhancement value of 2.56. For this GTI-stacker cavity the predicted stacking efficiency χ_{exp} = 97.38% from Eq. (14) and Eq. (13) is also practically the same as the measured value of 97.4%.

For the femtosecond experiment we have shown that the pulse stacker does not affect the quality of the compressed short pulses at the system output. The normalized autocorrelation trace of the stacked and compressed solitary pulse at the GTI output is shown as the red line in Fig. 4.7. The blue line in this figure shows the normalized autocorrelation trace of the stacking signal at the input of the GTI stacker, measured after sending it through the same compressor. Both autocorrelation traces appear to overlap very closely, indicating the absence of any observable pulse distortions associated with the coherent pulse stacking process. Note also that the measured autocorrelation trace width of either trace is 1 ps, thus the corresponding de-convolved pulse duration is 700 fs, which is very close to the bandwidth limit of the 4 nm spectral bandwidth (of square-like spectrum) measured at the system output.

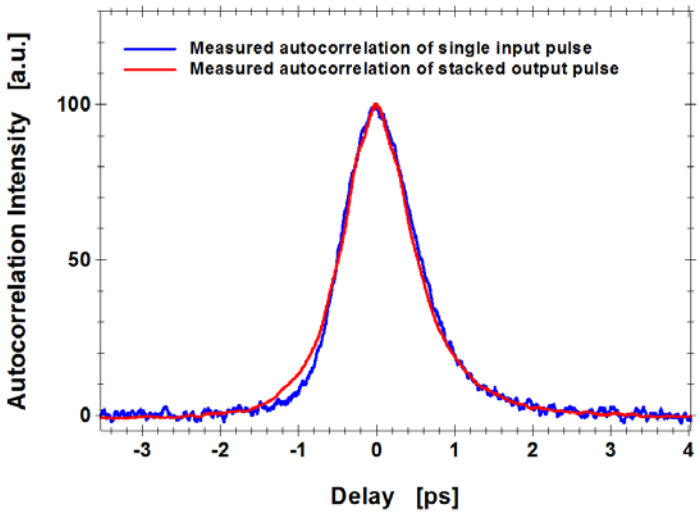

Fig. 4.7 Femtosecond experiment: normalized autocorrelation signals of the output stacked pulse, and the input stacking pulse of the GTI stacker.

It is important to discuss the relationship between the measured satellite-pulse contrast and the parameters of both the stacking cavity and the incident stacking-signal beam. As it was described in Subsection 4.3.1, since coherent pulse stacking is based on optical interference, it is very important to achieve complete spatial overlap between beams reflected from and transmitted through the cavity front mirror. To ensure this, the incident beam and the transmitted beam after each round trip should be sufficiently accurately matched in size. The two different experiments use two distinct strategies to achieve that. The nanosecond experiment uses a GTI cavity with all flat mirrors. For negligible beam diffraction over five complete roundtrips in the cavity the incident beam size has to be large enough to achieve a Rayleigh range much longer than this total propagation distance. We choose a 2.3 mm radius beam (measured at $1/e^2$ intensity) incident into the GTI. The achieved satellite-pulse contrast of 16 dB agrees well with the theoretically predicted expectation for this beam size. This contrast can be further improved by using even larger beam sizes. Increasing the beam size, however, is not very convenient from the practical standpoint. From this point the femtosecond experiment

uses a GTI cavity with a concave curved mirror M_2 with a focal length of 1.5 m. Therefore, the beam q-parameter is preserved every round-trip, provided the input beam size is mode-matched to the cavity. In this particular experiment the incident beam size is chosen to have a 700 μm radius (at $1/e^2$). However, in this case the stacking interferences are very sensitive to exactly matching the beam and mode sizes, and we attribute the achieved 15 dB satellite-pulse contrast to the residual beam-mode mismatch.

4.4 Coherent stacking of multitude of pulses in sequences of GTI cavities

Theoretical and experimental results presented above pertain to a single GTI cavity in which pulse peak-power enhancement only of up to 2.6 is possible. For practical use of this technique much larger stacking factors will be needed. In this section we theoretically and numerically show that this technique can be extended to stacking large numbers of equal-amplitude pulses by using properly configured sequences of multiple GTI cavities.

4.4.1 Cascaded equal-roundtrip GTI cavities

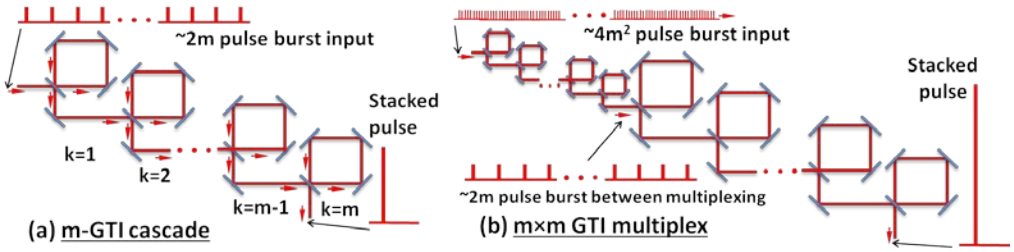

Fig. 4.8 (a) m cascaded equal-roundtrip GTI cavities; (b) m x m multiplexed different-roundtrip GTI cavities.

From the description given earlier it is clear that when stacking with a single GTI cavity the last "switching" pulse should have its energy comparable to the energy stored in the

cavity. However, by arranging multiple GTI cavities in a sequence (or cascade), as shown in Fig. 4.8 (a), it is possible to overcome this limitation, and to achieve stacking with an input-pulse burst containing approximately 2m equal-amplitude pulses for a sequence of m cascaded cavities. This process works by distributing the energy from a burst of 2m pulses among the m cavities, and then extracting this energy with the last, $2m^{th}$ pulse. This last pulse "grows" gradually when propagating through this cascade of cavities, so that every time this pulse arrives at the partially reflecting front mirror of the k^{th} cavity, its energy is comparable to the energy inside the cavity, and thus can extract all of the energy stored in the k^{th} cavity by constructively interfering with the stored intra-cavity pulse. Because the cavities are independent and every pulse follows the same optical path between each cavity, the distance between each cavity can be chosen arbitrarily.

We can show mathematically how the cascaded cavities work by extending the theoretical analysis for a single GTI cavity presented in Subsection 4.2.1 and Subsection 4.2.3. Let's use the same notation for cavity parameters and field amplitudes, but add subscripts indicating the corresponding cavity in the sequence, as shown in Fig. 4.8 (a). Then Eq. (5) can be rewritten to describe the interference in the k^{th} cavity, occurring between the input, output and circulating fields for the n^{th} input pulse as following:

$$\begin{bmatrix} {}^{out}_{k}\tilde{A}_n \\ {}^{cav}_{k}\tilde{A}_{n-1} \end{bmatrix} = \begin{bmatrix} 1 & 0 \\ 0 & \alpha_k e^{i\delta_k} \end{bmatrix} \begin{bmatrix} r_k & it_k \\ it_k & r_k \end{bmatrix} \begin{bmatrix} {}^{out}_{k-1}\tilde{A}_n \\ {}^{cav}_{k}\tilde{A}_n \end{bmatrix}.$$

Note that now the output field from each cavity becomes the input field for the next cavity in the sequence ${}^{out}_{k-1}\tilde{A}_n = {}^{in}_{k}\tilde{A}_n$. This leads to the following set of equations, which are analogous to Eq. (6) and Eq. (7) from above for the semi-infinite input pulse train case when there are m cavities:

$$\begin{bmatrix} 1 \\ 0 \end{bmatrix} = \begin{bmatrix} 1 & 0 \\ 0 & \alpha_m e^{i\delta_m} \end{bmatrix} \begin{bmatrix} r_m & it_m \\ it_m & r_m \end{bmatrix} \begin{bmatrix} {}^{out}_{m-1}\tilde{A}_0 \\ {}^{cav}_{m}\tilde{A}_0 \end{bmatrix}, \quad \text{for n=0 and k=m} \tag{15}$$

$$\begin{bmatrix} {}^{out}_{k}\tilde{A}_0 \\ 0 \end{bmatrix} = \begin{bmatrix} 1 & 0 \\ 0 & \alpha_k e^{i\delta_k} \end{bmatrix} \begin{bmatrix} r_k & it_k \\ it_k & r_k \end{bmatrix} \begin{bmatrix} {}^{out}_{k-1}\tilde{A}_0 \\ {}^{cav}_{k}\tilde{A}_0 \end{bmatrix}, \quad \text{for n=0 and k=2,3,...m-1} \tag{16}$$

$$\begin{bmatrix} {}^{out}_{1}\tilde{A}_n \\ 0 \end{bmatrix} = \begin{bmatrix} 1 & 0 \\ 0 & \alpha_1 e^{i\delta 1} \end{bmatrix} \begin{bmatrix} r_1 & it_1 \\ it_1 & r_1 \end{bmatrix} \begin{bmatrix} {}^{in}_{1}\tilde{A}_0 \\ {}^{cav}_{1}\tilde{A}_0 \end{bmatrix}, \quad \text{for n=0 and k=1} \tag{17}$$

$$\begin{bmatrix} 0 \\ {}^{cav}_{m}\tilde{A}_{n-1} \end{bmatrix} = \begin{bmatrix} 1 & 0 \\ 0 & \alpha_m e^{i\delta_m} \end{bmatrix} \begin{bmatrix} r_m & it_m \\ it_m & r_m \end{bmatrix} \begin{bmatrix} {}^{out}_{m-1}\tilde{A}_n \\ {}^{cav}_{m}\tilde{A}_n \end{bmatrix}, \quad \text{for n=1,2,...}\infty \text{ and k=m} \tag{18}$$

$$\begin{bmatrix} {}^{out}_{k}\tilde{A}_n \\ {}^{cav}_{k}\tilde{A}_{n-1} \end{bmatrix} = \begin{bmatrix} 1 & 0 \\ 0 & \alpha_k e^{i\delta_k} \end{bmatrix} \begin{bmatrix} r_k & it_k \\ it_k & r_k \end{bmatrix} \begin{bmatrix} {}^{out}_{k-1}\tilde{A}_n \\ {}^{cav}_{k}\tilde{A}_n \end{bmatrix}, \quad \text{for n=1,2,...}\infty \text{ and k=2,3,...m-1} \tag{19}$$

$$\begin{bmatrix} {}^{out}_{1}\tilde{A}_n \\ {}^{cav}_{1}\tilde{A}_{n-1} \end{bmatrix} = \begin{bmatrix} 1 & 0 \\ 0 & \alpha_1 e^{i\delta_1} \end{bmatrix} \begin{bmatrix} r_1 & it_1 \\ it_1 & r_1 \end{bmatrix} \begin{bmatrix} {}^{in}_{1}\tilde{A}_n \\ {}^{cav}_{1}\tilde{A}_n \end{bmatrix}, \quad \text{for n=1,2,...}\infty \text{ and k=1} \tag{20}$$

For each incident pulse n ≥ 0 there are 2m algebraic equations, which completely define all 2m fields ${}^{in}_{k}\tilde{A}_n$ and ${}^{cav}_{k}\tilde{A}_n$ (k = 1, ... m) present for that incident pulse in all m cavities, each as a function of front-mirror reflectivities $r_1, r_2, ..., r_m$, round-trip phases $\delta_1, \delta_2, ..., \delta_m$ of all GTI cavities in the sequence, and the pulse number n. We are interested only in the input-field amplitudes into the first GTI cavity ${}^{in}_{1}\tilde{A}_n$, each defined by the 2m independent parameters $r_1, r_2, ..., r_m$ and $\delta_1, \delta_2, ..., \delta_m$. Consequently, we can choose to write 2m-1 equations $\left|{}^{in}_{1}\tilde{A}_n\right|^2 = \left|{}^{in}_{1}\tilde{A}_{n+1}\right|^2$ for n = 0, 1, …, 2m-1, which set the condition for all peak-intensities of the last 2m pulses in the incident pulse burst to be equal. This means that a pulse burst with 2m equal-amplitude pulses can be stacked in a

sequence of GTI cavities with m reflectivities $r_1, r_2, ..., r_m$, and m-1 round-trip phases $\delta_1, \delta_2, ..., \delta_{m-1}$ defined by solving these 2m-1 equations. One of the round-trip phases (for example δ_m) can be freely selected, and only affects the required individual-pulse phases of the input stacking-pulse burst.

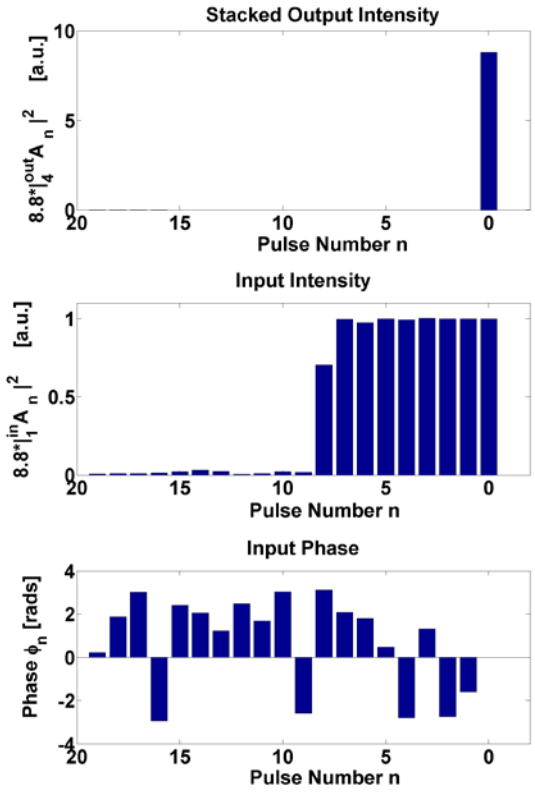

Fig. 4.9 The calculated intensities and phases of the semi-infinite input pulse burst and the output pulse intensities of 4 cascaded cavities (cavity parameters given in the text).

A calculated example for the case of 4 cascaded cavities and a semi-infinite pulse train is presented in Fig. 4.9, showing a stacking sequence consisting of eight equal-amplitude pulses with a numerical stacking factor close to 9, since the n = 8 pulse in the burst has its peak intensity nearly equal to those of the last eight pulses. The calculated GTI-cascade parameters $R_k = |r_k|^2$ and δ_k are as follows: R_1=0.535, R_2=0.526, R_3=0.618, R_4=0.666, δ_1=4.66, δ_2=3.15, δ_3=5.46, and we chose δ_4=0. Note that in reality this semi-infinite

stacking- pulse train can be truncated to a finite pulse burst, just as in the single-GTI configuration. A promising truncation for this 4 cavity scenario is to choose 9 equal-amplitude input pulses, and the CPSA simulation is presented in Fig. 4.10, showing an input pulse sequence consisting of 9 equal-amplitude pulses and an output stacked pulse with a numerical pulse energy enhancement factor of η=8.8.

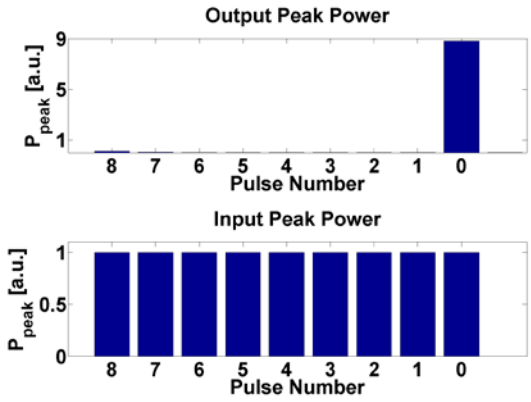

Fig. 4.10 The calculated peak power amplitudes of the 9 equal-amplitude input pulses and the output pulse of 4 cascaded cavities.

4.4.2 Multiplexed different-roundtrip GTI cavities

Cascaded equal-roundtrip GTI cavities provide multiple-pulse stacking proportional to the number of GTI cavities. It is possible to achieve a substantially quicker increase in stacking factors by using a multiplexed GTI cavity configuration shown in Fig. 4.8 (b). This configuration essentially multiplexes a cascade of m equal-roundtrip GTI cavities with an identical cascade of m GTI cavities, but with the second cascade round-trip being more than 2m times longer than that of the first cascade. In this case, the first set of m cavities transforms a pulse burst with $4m^2$ pulses into a burst of 2m pulses with a pulse separation that is 2m times longer than the initial pulse separation and a peak power that is 2m times larger. The second set of m cavities then transforms that burst of 2m pulses into a single pulse with roughly $4m^2$ times the peak power of a single pulse from the

initial burst. A numerically calculated example for the case of 4 x 4 multiplexed cavities and a finite input-pulse burst consisting of 81 equal-amplitude pulses is shown in Fig. 4.11 using the same GTI front mirror reflectivities and cavity round-trip phases as in the previous example of 4 cascaded cavities in Subsection 4.4.1. It shows that by multiplexing eight GTI cavities, one can achieve a stacked peak-power enhancement close to 80 times. Another example using 4 x 4 x 4 multiplexed GTI cavities will allow 729 equal-amplitude input pulses to be stacked into an output pulse, which is shown in the numerical simulation presented in Fig. 4.12. Therefore, starting with relatively low input pulse energies gives the ability to extract all of the stored energy from a single fiber amplifier with low nonlinearity.

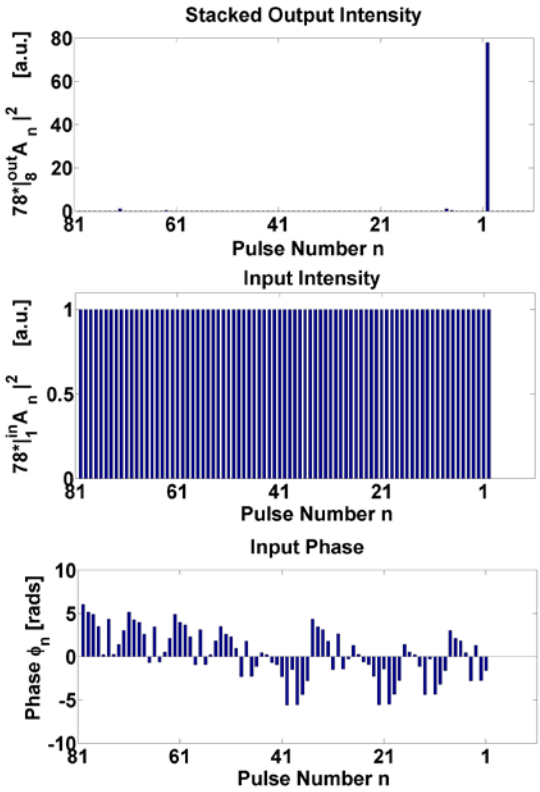

Fig. 4.11 The calculated intensities and phases of the input pulse burst and the output pulse intensities of 4 x 4 multiplexed cavities (cavity parameters given in the text).

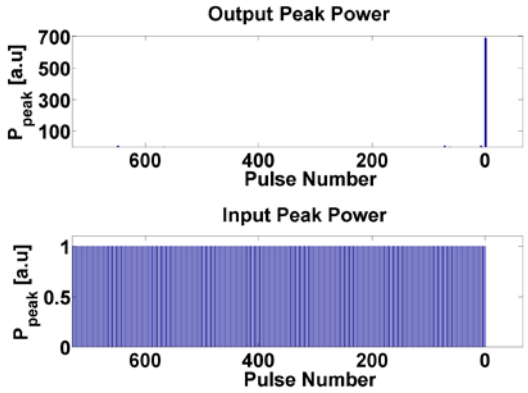

Fig. 4.12 The calculated peak power amplitudes of the input pulse burst and the output pulse of 4 x 4 x 4 multiplexed cavities.

4.4.3 Cavity stabilization for multi-GTI systems

In a cascaded- and multiplexed-GTI system for stacking large number of equal-amplitude pulses, the round-trip lengths of all GTI cavities have to be stabilized to achieve coherent stacking, just similar to the single-GTI coherent pulse stacking experiment described in Section 4.3.

While the monitor-beam stabilization scheme, which is used in the single-GTI coherent pulse stacking experiment described in Section 4.3, can be extended to this multi-cavity case, here we propose and analyze a more efficient and elegant cavity stabilization scheme without the need of any monitor beam, the two-photon absorption (TPA) detection scheme. This scheme is based on a similar idea as in the LOCSET coherent phasing scheme in which each channel is "tagged" by individual harmonic-modulation frequency imprinted through a phase modulator and the detection of individual-channel errors is done with a single detector [16,17]. Here it is each GTI cavity round-trip length that is "tagged" by individual harmonic-modulation frequency. The main challenge in applying LOCSET to multi-cavity stabilization is associated with the fact that in the multi-cavity coherent pulse stacking case the output average power is independent with

the individual cavity round-trip phases. Thus a linear detector (i.e. a detector with an output signal *linearly* proportional to the incident power) at the system output appears to be of no use for stabilization the cavities.

As a result, it is necessary to devise a new cavity-phase-sensitive detection approach. Since the objective of the coherent pulse stacking process is to achieve a single stacked output pulse, it is natural to seek a detection scheme that would sense stacked pulse peak power. This can be done by replacing a linear detector with a quadratic one, i.e. a detector with an output signal *quadratically* proportional to the incident peak power. We have implemented a quadratic detector by using a standard semiconductor diode specially selected so that photon energy of ~1μm wavelength light falls well below its band gap edge. Consequently, output signal of this detector is produced only by two-photon absorption (TPA), and is, therefore, proportional to the square of the peak power.

It is obvious that the highest TPA signal will occur for the optimum stacking case, when all cavity round-trip phases are as required for coherent pulse stacking, and the stacked pulse peak power is at its maximum. It is, however, far from obvious whether TPA signal always increases with decreasing phase mismatches of the cavity round-trip phases. Indeed, phase mismatches of the cavity round-trip phases result in multiple output pulses after pulse stacking. In principle, in a m-cavity system there are m degrees of freedom in controlling the output pulse/pulses. This leads to a very complicated "landscape" of possible stacked output pulse profiles, and to a very complex change in these profiles with decreasing phase mismatches. However, if the TPA signal would indeed increase with decreasing phasing errors, then each cavity round-trip phase can be stabilized as required by the TPA detection feedback. In other words, each cavity round-

trip phase is corrected by the corresponding TPA detection feedback signal for this cavity until the TPA signal at the system output is maximized, which corresponds to the optimum stacking case. The TPA detection feedback signal is unique for each cavity and is produced through a modulation-demodulation technique as applied in the LOCSET scheme. An example of using the TPA detection scheme for stabilizing N cascaded GTI cavities is shown in Fig. 4.13.

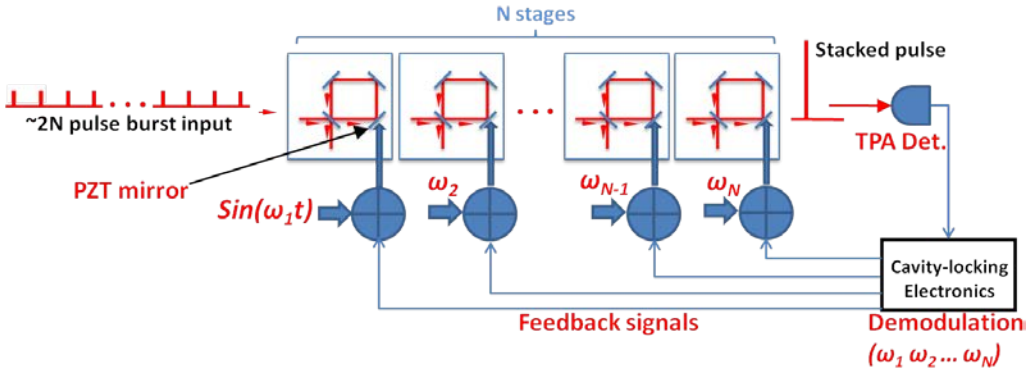

Fig. 4.13 The TPA detection scheme for stabilizing N cascaded GTI cavities.

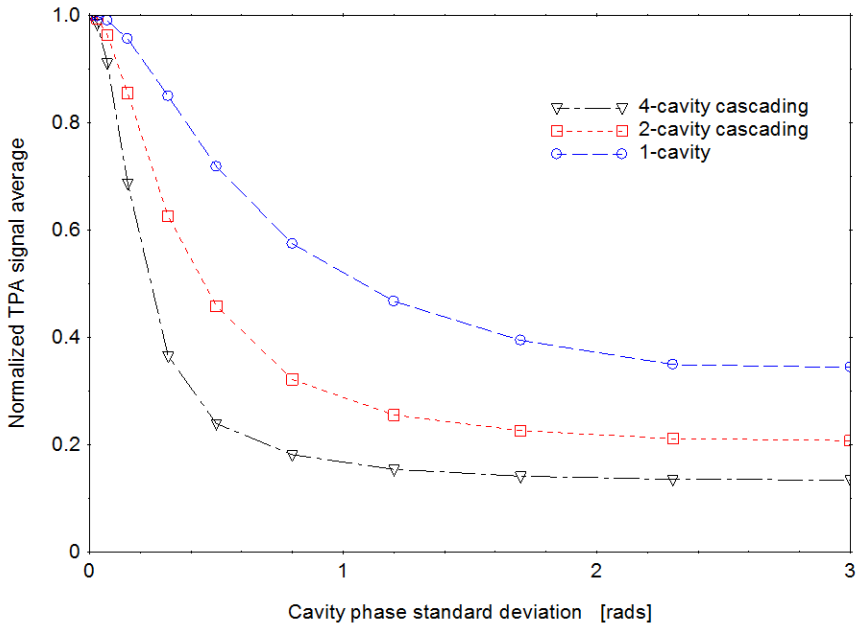

Fig. 4.14 Normalized average TPA signals versus cavity phase standard deviations for coherent pulse stacking with a single GTI, 2 cascaded GTIs, and 4 cascaded GTIs.

In order to validate suitability of a quadratic detector for implementing cavity stabilization of a cascaded- and multiplexed-GTI system, we have performed a numerical statistical study of TPA signal dependence on cavity round-trip-phase mismatches. This study shows that statistically the TPA detector output always increases with the decrease in the overall cavity round-trip phase errors, and, therefore, confirms that the quadratic detector should work with the LOCSET scheme.

Fig. 4.14 shows the results of the numerical statistical study of the TPA signal dependence on the cavity round-trip phase errors. This study is based on simulations of coherent pulse stacking processes for the cases of single-GTI, 2 cascaded GTIs, and 4 cascaded GTIs. Take the case of 4 cascaded GTIs for example, we manually set 10 cavity phase standard deviations distributed from 0 to pi. For each cavity phase standard deviation, we generate 10000 sets of particular cavity phase combination $\{\varphi_1, \varphi_2, \varphi_3, \varphi_4\}$, where each cavity phase φ_i is randomly generated using Gaussian probability distribution with the cavity phase standard deviation. We do the coherent pulse stacking simulation based on each particular cavity phase combination and calculate the average TPA signal of the 10000 sets, thus get the statistical average TPA signal for a particular cavity phase standard deviation. The normalized average TPA signals are plotted out versus the 10 cavity phase standard deviations for the cases of single-GTI, 2 cascaded GTIs, and 4 cascaded GTIs in Fig. 4.14. Plotted results clearly show that the TPA electric-response signal *increases* with the *decrease* of overall cavity round-trip phase error. It is also shown in this study that the TPA signal sensitivity on cavity round-trip phase errors increases with the increase of the number of cascaded GTI cavities. Thus,

the proposed TPA detection cavity stabilization scheme becomes more effective in a larger coherent pulse stacking system consisting of more GTI cavities.

Experimentally we verify the validity of the TPA detection cavity stabilization scheme in a single-GTI coherent pulse stacking experiment. Fig. 4.15 shows the TPA signal as well as the feedback correction signal when the GTI cavity round-trip phase is stabilized and when the cavity stabilization is turned off. As shown in the figure, the TPA detection scheme stabilize the cavity round-trip phase as required by correcting the cavity phase to maximize the TPA signal at the system output.

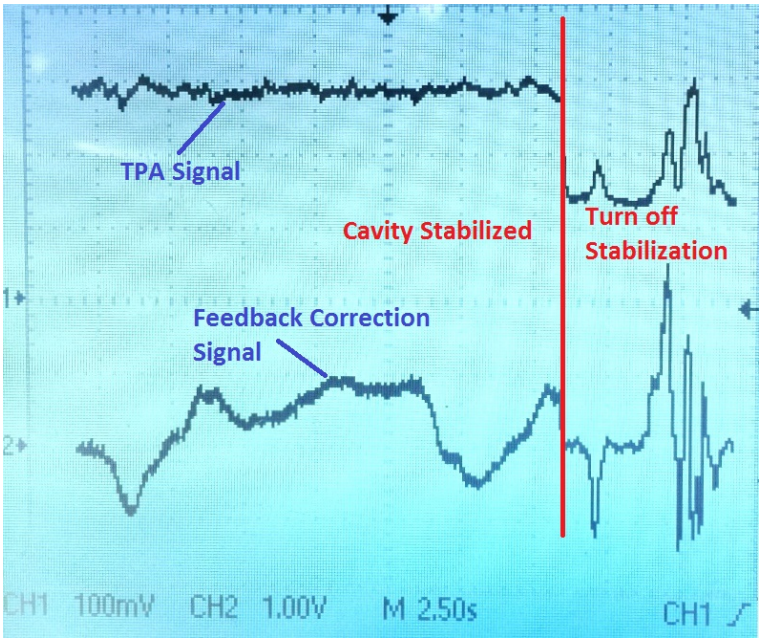

Fig. 4.15 The TPA signal and the feedback correction signal before and after the cavity stabilization for single-GTI coherent pulse stacking is turned off.

4.5 Coherent pulse stacking utilizing very-compact Herriott cell

As discussed in Section 4.4, in order to achieve very large stacking enhancement factors, GTI cavities with long roundtrip lengths are needed in order to satisfy the 2m scaling condition on the subsequent sets. Thus it is greatly beneficial to use multi-pass Herriott-

type cells to provide long cavity lengths with small footprints. The Herriott cell design basically serves as a very compactly folded delay line that preserves the q-parameter of an input Gaussian beam [18]. Our analysis shows these GTI cavities can be compactly folded using Herriott cell configurations by a factor of up to ~50, thus establishing pulse energy scaling metrics for the extension into multiple GTI cascades [19].

We show in a single-GTI coherent pulse stacking (CPS) experiments how Herriott-type cells can be incorporated in the CPS technique. The design we select for this experiment results in 10 roundtrips through a 12 cm Herriott cell which results in 2.4 m of total path length in this very compact footprint, which is shown in Fig. 4.16. We experimentally demonstrate single-stage coherent pulse stacking of a burst of femtosecond pulses with a burst energy up to 100 uJ by implementing this Herriott cell. The input pulse burst with a burst energy of 12.5 uJ and the output stretched pulses of the GTI stacker are also shown in Fig. 4.16.

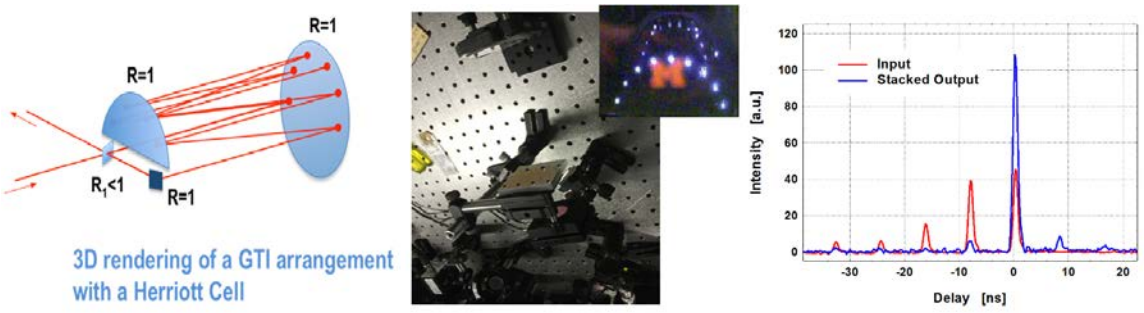

Fig. 4.16 A compact GTI with Herriott cell and the coherent pulse stacking experiment using this GTI with a input burst energy of 12.5 uJ.

For the CPS example using 4 x 4 x 4 multiplexed GTI cavities described in Subsection 4.4.2, assuming using a high repetition rate oscillator (1 GHz), the roundtrip lengths of the 3 sets of 4 GTI cavities would be 0.3m, 2.7m, and 24.3m respectively. It is possible to use Herriott cells to compactly fold the 2.7m cavities into roughly 10cm mirror

separations, and the 24.3m cavities into roughly 50cm mirror separations. This will allow all of the cavities to be folded into a compact arrangement, thus making the technique very practical.

4.6 Summary and conclusions

In conclusion, we have proposed and demonstrated a new technique of coherent pulse stacking (CPS) amplification to overcome limits on achievable energies of short optical pulses from optical amplifiers. We achieve CPS of amplified femtosecond and nanosecond pulses based on a single reflecting resonant cavity, with near-theoretical stacked peak-power enhancement factors of ~2.5 and high satellite-pulse contrast factors of ~16 dB.

We experimentally demonstrate that this CPS technique is compatible with the chirped-pulse amplification (CPA) technique. We also show theoretically that large numbers of equal-amplitude pulses can be stacked using sequences of multiple reflecting resonators. Further work on cascading of multiple GTI cavities for attaining orders of magnitude higher peak-power enhancement factors is in progress. This CPS technique, when implementing together with CPA and coherent combining techniques, offers a potential path to achieving very high-energy pulses from ultrashort-pulse fiber-amplifier systems.

4.7 Appendix A: Finite-length input pulse sequences

In practice one needs to truncate the semi-infinite input pulse train discussed in Subsection 4.2.3 into a finite pulse burst consisting of N pulses. Since we count pulses from $n = 0$, the very first pulse in this sequence corresponds to $n = N - 1$. Coherent pulse

stacking conditions defined by Eq. (6) and (7) still apply to all the pulses in the finite sequence, except for this very first pulse. Indeed, since there are no prior pulses this $n = N - 1$ pulse can only reflect from the front mirror, because it cannot interfere with any prior field in the GTI cavity. Consequently, we can rewrite the amplitude-coefficient condition set by Eq. (7) for this first $n = N - 1$ pulse as

$$\begin{bmatrix} {}^{out}\tilde{a}_{N-1} \\ {}^{cav.}\tilde{A}_{N-2} \end{bmatrix} = \begin{bmatrix} 1 & 0 \\ 0 & \alpha \cdot e^{i\delta} \end{bmatrix} \cdot \begin{bmatrix} r & it \\ it & r \end{bmatrix} \cdot \begin{bmatrix} {}^{in}\tilde{a}_{N-1} \\ 0 \end{bmatrix}. \tag{21}$$

Here we use the lowercase letters $\tilde{a}$ instead of $\tilde{A}$ to distinguish between the (N-1)st pulse amplitude coefficients in the finite and semi-infinite sequences respectively, as shown in Fig. 4.2. Consequently, Eq. (8) and (21) give us:

$$\begin{cases} {}^{in}\tilde{a}_{N-1} = \dfrac{{}^{in}\tilde{A}_{N-1}}{1-R} \\ {}^{out}\tilde{a}_{N-1} = -\left(\dfrac{r}{\alpha \cdot e^{i\delta}}\right)^{N-1} \end{cases} \tag{22}$$

From this it is clear that the amplitude coefficient of the first input pulse in the finite sequence is by a factor $1/(1 - R)$ larger than the amplitude coefficient of the same input pulse in the semi-infinite sequence, all the other amplitudes of pulses with $n < N - 1$ are the same in both finite and semi-infinite sequences. The GTI output with a finite sequence input contains both the stacked pulse as well as a weak first-pulse reflection with amplitude ${}^{out}\tilde{a}_{N-1}$. From Eq. (22) describing ${}^{out}\tilde{a}_{N-1}$ it is also clear that this reflection can be made negligibly small by increasing the length N of the incident pulse burst. For example, for a 9-pulse stacking sequence this reflection peak power can be smaller than 10^{-3} of the stacked pulse peak power.

4.8 Appendix B: Energy efficiency of a GTI pulse stacker

The energy efficiency is defined as the ratio χ between the energy of a stacked output pulse $\varepsilon_{\text{stck.}}$ and the total energy of an incident pulse train ε_{in}: $\chi = \varepsilon_{\text{stck.}}/\varepsilon_{\text{in}}$. Because in our analysis we assumed that all incident, circulating and output pulses have identical envelopes $p_s(t)$ but, in general, different peak powers, and we choose to normalize the peak power coefficient ${}^{out}B_0$ of a stacked output pulse to 1, the energy of a stacked output pulse $\varepsilon_{stck.}$ can be calculated as follows:

$$\varepsilon_{stck.} = {}^{out}B_0 \cdot \int_{-\infty}^{+\infty} p_s{}^2(t)dt = {}^{out}B_0 \cdot \varepsilon_S = \varepsilon_S .$$

Here ε_S denotes the energy of a solitary pulse with a unit peak power coefficient and envelope $p_s(t)$. The total energy of the incident semi-infinite pulse train can be calculated using Eq. (4):

$$\varepsilon_{in} = \int_{-\infty}^{+\infty} \left| {}^{in}\tilde{p}(t) \right|^2 dt = \int_{-\infty}^{+\infty} \sum_{n=0}^{\infty} \left| {}^{in}\tilde{A}_n \cdot \tilde{p}_S(t + n \cdot \Delta T) \right|^2 dt = \sum_{n=0}^{\infty} \left| {}^{in}\tilde{A}_n \right|^2 \cdot \varepsilon_S = \sum_{n=0}^{\infty} {}^{in}B_n \cdot \varepsilon_S .$$

Here we assumed that the temporal overlap between adjacent pulses in the incident pulse train is negligible. Then the energy efficiency χ_∞ of a GTI pulse stacker when the incident pulse train is semi-infinite can be expressed as

$$\chi_\infty = \frac{\varepsilon_{stck.}}{\varepsilon_{in}} = \left(\sum_{n=0}^{\infty} {}^{in}B_n \right)^{-1} . \tag{23}$$

For calculating the energy efficiency χ_N for an N-pulse train we need to consider that according to Eq. (22) the first pulse in a finite input sequence has a different peak power

coefficient ${}^{in}b_{N-1}$ compared to a corresponding ${}^{in}B_{N-1}$ of a semi-infinite input sequence: ${}^{in}b_{N-1}\cdot(1-R)^2 = {}^{in}B_{N-1}$. Then we can express χ_N as

$$\chi_N = \frac{\varepsilon_{stck.}}{\varepsilon_{in}} = \left(\sum_{n=0}^{N-2} {}^{in}B_n + b_{N-1}\right)^{-1} = \left(\sum_{n=0}^{N-2} {}^{in}B_n + \frac{B_{N-1}}{(1-R)^2}\right)^{-1}. \tag{24}$$

According to Eq. (9) the peak power coefficients B_1, B_2,… constitute a geometrical progression, which allows the simplification of the sums in Eq. (23) and (24). For a semi-infinite input this gives

$$\chi_\infty = \left(B_0 + \sum_{n=1}^{\infty} {}^{in}B_n\right)^{-1} = \left(R + \frac{(1-R)^2}{\alpha^2 - R}\right)^{-1} = \frac{\alpha^2 - R}{1-R(2-\alpha^2)}, \tag{25}$$

and for an *N*-pulse train after some algebra one can show that

$$\chi_N{}^{-1} = \chi_\infty{}^{-1} + \left(\frac{R}{\alpha^2}\right)^{N-1} \frac{\alpha^2(2-R)-1}{\alpha^2 - R}. \tag{26}$$

When $\alpha^2 = 1$ the GTI pulse stacker cavity is lossless and, according to Eq. (25), the stacking efficiency of a semi-infinite input train is 100%: $\chi_\infty = 1$. By taking the Taylor expansion of $\chi_\infty(\alpha^2)$ in Eq. (25) at $\alpha^2 = 1$, and retaining only zero- and first-order terms one can show that $\chi_\infty \approx \alpha^2$, when $\alpha^2 \approx 1$. Numerical calculation shows that this approximation remains accurate to within 1% for $\alpha^2 > 0.89$. Also, from Eq. (26) one can see that in the majority of practical cases $\chi_N < \chi_\infty$ since usually $\alpha^2 > R$, $R = R_{\text{opt}}$, and $\alpha^2 \approx 1$. Note that for a lossless GTI when $\alpha^2 = 1$ we have $\chi_N{}^{-1} = \chi_\infty{}^{-1} + R^{N-1}$.

4.9 References

1. D. Strickland and G. Mourou, “Compression of amplified chirped optical pulses,” Opt. Commun. **56**(3), 219 (1985).

2. F. Stutzki, F. Jansen, A. Liem, C. Jauregui, J. Limpert, and A. Tünnermann, "26 mJ, 130 W Q-switched fiber-laser system with near-diffraction-limited beam quality," Opt. Lett. **37**(6), 1073-1075 (2012).

3. F. Röser, T. Eidam, J. Rothhardt, O. Schmidt, D. N. Schimpf, J. Limpert, and A. Tünnermann, "Millijoule pulse energy high repetition rate femtosecond fiber chirped-pulse amplification system," Opt. Lett. **32**(24), 3495-3497 (2007).

4. M. Kienel, A. Klenke, T. Eidam, S. Hädrich, J. Limpert, and A. Tünnermann, “Energy scaling of femtosecond amplifiers using actively controlled divided-pulse amplification,” Opt. Lett. **39**(4), 1049-1052 (2014).

5. Y. Zaouter, F. Guichard, L. Daniault, M. Hanna, F. Morin, C. Hönninger, E. Mottay, F. Druon, and P. Georges, "Femtosecond fiber chirped- and divided-pulse amplification system," Opt. Lett. **38**(2), 106-108 (2013).

6. R. Jason Jones, and Jun Ye, "Femtosecond pulse amplification by coherent addition in a passive optical cavity," Opt. Lett. **27**(20), 1848-1850 (2002).

7. S. Breitkopf, T. Eidam, A. Klenke, L. von Grafenstein, H. Carstens, S. Holzberger, ..., and J. Limpert, "A concept for multiterawatt fibre lasers based on coherent pulse stacking in passive cavities," Light: Science & Applications. **3**(10), e211 (2014).

8. A. E. Siegman, *Lasers* (University Science Books, 1986), Chap. 11.

9. X. Ma, C. Zhu, I. Hu, A. Kaplan, and A. Galvanauskas, "Single-mode chirally-coupled-core fibers with larger than 50μm diameter cores," Opt. Express. **22**(8), 9206-9219 (2014).

10. J. Ye, and S. T. Cundiff, *Femtosecond Optical Frequency Comb: Principle, Operation, and Applications* (Springer, 2005), Chap. 9.

11. L. Hollberg, C. W. Oates, E. A. Curtis, E. N. Ivanov, S. A. Diddams, T. Udem, H. G. Robinson, J. C. Bergquist, R. J. Rafac, W. M. Itano, R. E. Drullinger, and D. J. Wineland, "Optical frequency standards and measurements," IEEE J. Quant. Electron. **37**(12), 1502-1513 (2001).

12. R. W. P. Drever, J. L. Hall, F. V. Kowalski, J. Hough, G. M. Ford, A. J. Munley, and H. Ward, “Laser phase and frequency stabilization using an optical resonator,” Appl. Phys. B **31**(2), 97-105 (1983).

13. S. T. Cundiff, "Phase stabilization of ultrashort optical pulses," J. Phys. D: Appl. Phys. **35**(8), R43-R59 (2002).

14. A. Yariv, and P. Yeh, *Optical Waves in Crystals* (Wiley, 1984), Chap. 9.

15. F. Kuyama, and K. Iga, "Frequency chirping in external modulators," J. Lightwave Technol. **6**(1), 87-93 (1988).

16. T. M. Shay, “Theory of electronically phased coherent beam combination without a reference beam,” Opt. Express 14, 12188-12195 (2006)

17. T. M. Shay, V. Benham, A. D. Sanchez, D. Pilkington, and C. A. Lu, “Self-synchronous and self-referenced coherent beam combination for large optical arrays,” IEEE J. Sel. Top. Quant. 13, 480-486 (2007)

18. D. R. Herriott, H. Kogelnik, and R. Kompfner, “Off-axis paths in spherical mirror interfometers,”Appl. Opt. 3, 523-526 (1964).

19. Tong Zhou, John Ruppe, Cheng Zhu, I-Ning Hu, John Nees, Russell Wilcox, Wim Leemans, and Almantas Galvanauskas, “Coherent Pulse Stacking Amplification using Cascaded and Multiplexed Gires-Tournois Interferometers,” submitted to CLEO 2015.

Chapter 5

N^2 coherent combining of parallel chirped pulse fiber amplifiers (Spatial and time domains)

5.1 Introduction

Achieving very-high-energy short pulses from fiber amplifier systems is practically hindered by peak power limitations due to detrimental nonlinear effects, such as self-phase modulation, four-wave-mixing, critical self-focusing, etc. The chirped pulse amplification (CPA) technique alleviates this limitation by a factor of up to 10^3 - 10^4 times by stretching broadband ultrashort pulses prior to amplification and compressing them afterwards [1], thus enabling pulse energies up to the range of 100μJ to ~1 mJ, which is yet much less than the stored pulse energy of the fiber amplifier [2]. Consequentially, achieving approximately 40 J per ultrashort pulse as needed for a 10GeV laser-plasma acceleration stage [3], would require combining of 10^4 - 10^5 parallel amplification channels in a coherently phased fiber laser array.

To maximize achievable pulse energy per CPA channel, in this chapter a multi-dimensional N^2 coherent combining techniques is proposed. Based on passive resonant cavities, N^2 coherent combining represents coherent pulse synthesis in both time and spatial domains, enhancing both average power and pulse energy. Average power is increased proportionally to the number of channels N in an array, the same as in any

other coherent or incoherent combining approaches. The unique aspect of N^2 combining is that it simultaneously reduces by N times pulse repetition rate in the combined beam at the system output, thus increasing the resulting energy per pulse proportionally to N^2 times. Use of this technique enables achieving high pulse energies with relatively small number of parallel coherently-phased amplification channels, much smaller than would be required by using conventional coherently combined arrays.

5.2 Concept of N^2 coherent combining

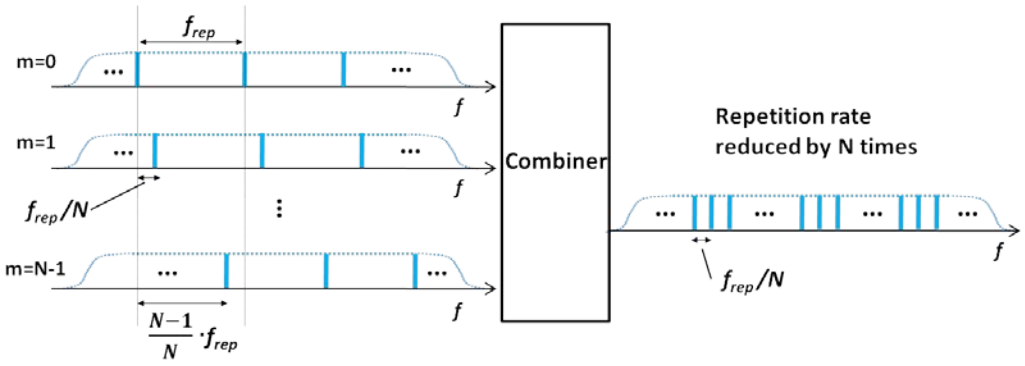

Fig. 5.1 The concept of N^2 coherent combining.

Fig. 5.1 outlines the concept of N^2 coherent combining, showing how *N* spatially-separate periodic pulse trains (in parallel channels labeled $m = 0,1, \ldots, N\text{-}1$) can be combined into one spatial beam with *N*-times lower pulse repetition rate. The concept can be best explained in the frequency domain. N^2 combining can only be achieved with strictly periodic pulse trains. In the frequency domain such signals are described by a pulse envelope, multiplied by a frequency-comb (i.e. a frequency-periodic sequence of vanishingly-narrow spectral lines). The separation between frequency-comb lines corresponds to the pulse repetition frequency f_{rep}. In this arrangement all parallel channels have the same repetition frequency and the same pulse envelope. However, for

achieving N^2 combining it is necessary that each-channel signal is individually phase modulated such that the *m*-th channel frequency comb is frequency shifted by $(m/N)\cdot f_{rep}$ with respect to the m=0 channel signal. Then linear addition in a combiner of all *N* evenly shifted frequency combs should produce a signal, which in the spectral domain is characterized by the same pulse envelope, but with *N* times denser frequency comb lines separated by f_{rep}/N. In the time domain this corresponds to *N* times lower pulse repetition rate compared to the repetition rate in each of the channels. Consequentially, since average power in the combined beam is approximately *N* times higher, and the pulse repetition rate is *N* times lower than those of each channel, the combined-signal pulse energy is approximately N^2 times higher than in each channel.

Such a linear addition of beams containing evenly shifted frequency-combs can be achieved using beam combiners based on Fabry-Perot interferometer (FPI) cavities. This is shown in Fig. 5.2, where the simplest case of two-beam combining is presented as an illustrative example. Such two-beam combining requires a single FPI cavity, which in Fig. 5.2(a) is represented by a traveling-wave configuration consisting of partially reflecting front mirrors with reflectivity $R_F < 1$, and fully reflecting folding mirrors with $R_b = 1$. Fabry-Perot spectral transfer functions for reflection R(f) and transmission T(f) shown in Fig. 5.2 (b) are

$$R(f) = \frac{\sqrt{R_F}\cdot(1-e^{i2\pi f\delta/c})}{1-R_F\cdot e^{i2\pi f\delta/c}} \text{ and } T(f) = \frac{e^{i\pi f\delta/c}\cdot(1-R_F)}{1-R_F\cdot e^{i2\pi f\delta/c}}. \quad (1)$$

Here δ is the cavity round trip length, and c is the speed of light in the cavity. If the FPI round-trip time is equal to the pulse repetition period, then the cavity's free spectral range $\Delta f_{FSR} = c/\delta$ is equal to the pulse repetition rate f_{rep}. Consequentially, such a cavity can act

as an optical signal inter-leaver for the two evenly-shifted frequency combs, provided that cavity roundtrip δ is suitably selected to center transmission and reflection channel spectral transfer functions on the corresponding frequency combs, as shown in Fig. 5.2(a). This means that it is necessary to stabilize cavity length to the required length δ, as discussed in more detail in Section 5.5.

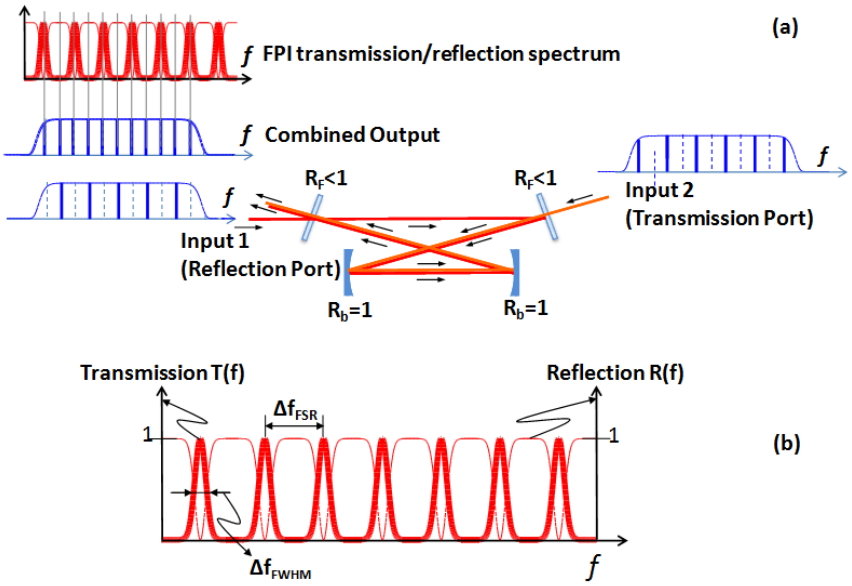

Fig. 5.2 N^2 coherent combining with a single cavity.

For combining more than two beams, it is necessary to use more than one FPI cavity. Fig. 5.3 shows an example of an FPI arrangement for coherent combining of N parallel channels, consisting of N -1 FPI cavities arranged sequentially. In this case it is important to note that each cavity should have its finesse (i.e. ratio between FPI free spectral range and its transmission linewidth $\Delta f_{FSR} / \Delta f_{FWHM} = \pi\sqrt{F} / 2$, where $F = 4R_F/(1-R_F)^2$) at least equal to the number of combined channels $\Delta f_{FSR}/\Delta f_{FWHM} \geq N$. Furthermore, each cavity's round-trip length δ_L should be individually selected (and stabilized) to align its transmission peak with the frequency comb of the corresponding transmitting input signal.

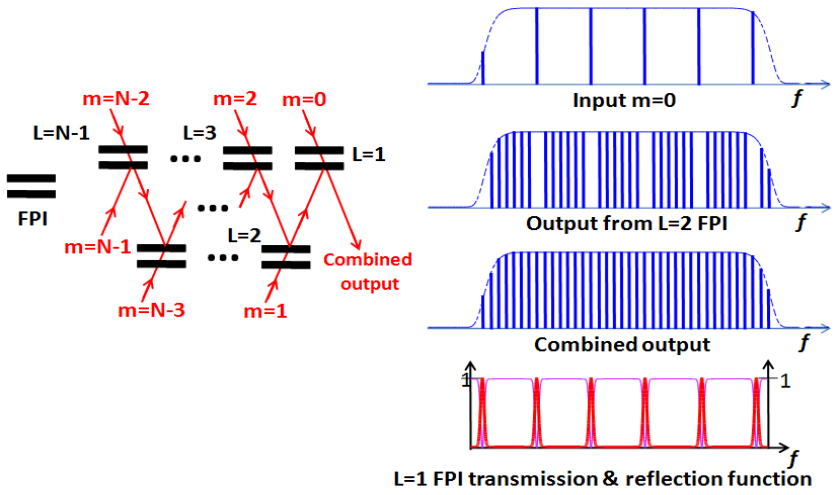

Fig. 5.3 A FPI sequence arrangement for N^2 coherent combining of N parallel channels.

Overall N^2 system architecture for a fiber CPA array is shown in Fig. 5.4. In this system initial seed of periodic pulses at f_{rep} from a mode-locked oscillator is split into N parallel amplification channels, where each signal can be frequency shifted by applying a suitably selected linear phase ramp through a phase modulator in each parallel channel. Note that such phase modulation would be relatively slow, since it is determined by the repetition rate f_{rep}. Since typical f_{rep} for mode-locked sources are in ~100MHz range, this should be easily achievable with standard 10GHz telecom-grade electro-optic modulators.

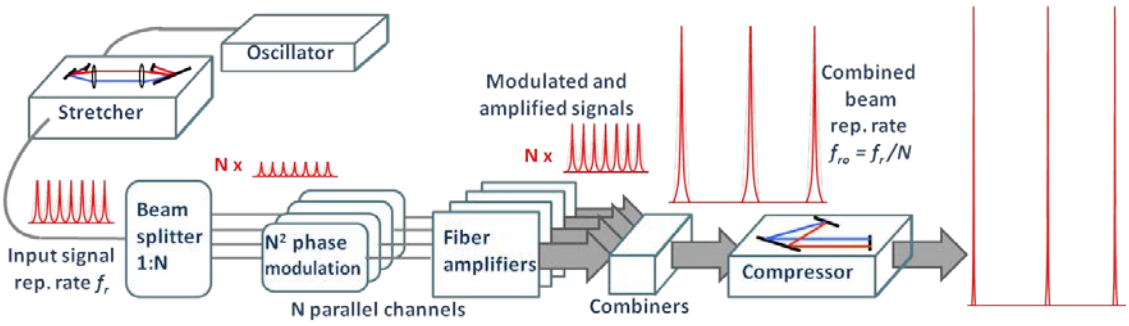

Fig. 5.4 The architecture of a N^2 coherent combining system.

5.3 Time-domain analysis of N^2 coherent combining

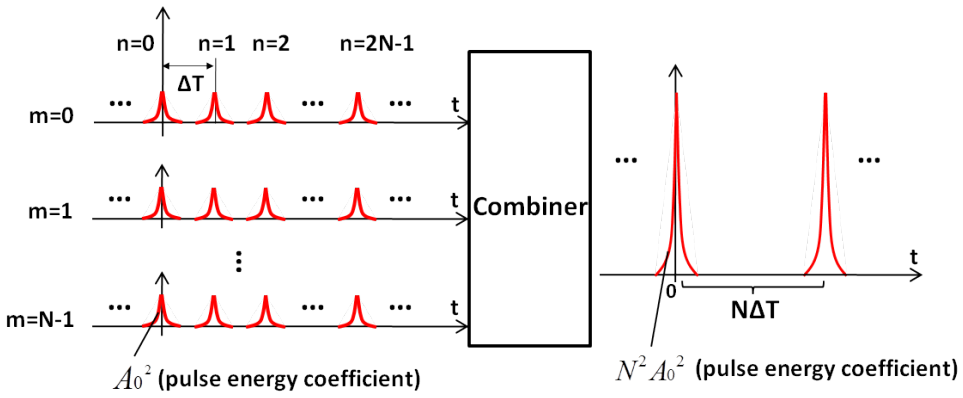

Fig. 5.5 Time-domain picture of N^2 coherent combining showing the input and output pulse sequences as well as their pulse energy coefficients.

Fig. 5.5 shows the time-domain picture of N^2 coherent combining, where it is assumed that all pulses at the input and output have identical complex envelopes $\tilde{p}_s(t)$. The complex notation accounts for the fact that stacking can be achieved with bandwidth-limited (described by real envelopes $\tilde{p}_s(t) \equiv p_s(t)$) as well as with chirped (described by complex envelopes $\tilde{p}_s(t)$) pulses. The time axis reference is set in a way such that the 0-th pulses in all the input channels are centered at t = 0. It is also assumed that all the input channels have identical pulse amplitude A_0 and identical pulse repetition period ΔT. In addition, to achieved N^2 coherent combining, a specific phase code/modulation (which shifts the frequency combs of the input pulse sequences as discussed in Section 5.2) is applied to the input pulse sequences, e.g. the n-th pulse in the m-th channel is phase modulated with a phase shift:

$$\psi_{mn} = e^{in\frac{m}{N}2\pi}. \tag{2}$$

Thus this pulse can be expressed as

$$\tilde{p}_{mn}(t) = A_0 e^{in\frac{m}{N}2\pi} \bullet \tilde{p}_S(t - n\Delta T) e^{i\omega_0 (t - n\Delta T + \phi_{0mn})}, \tag{3}$$

where ω_0 is the pulse carrier angular frequency and φ_{0mn} is the carrier initial phase. To achieve N^2 coherent combining, φ_{0mn} needs to be synchronized so that

$$\phi_{0mn} = \phi_{0n}, \tag{4}$$

which corresponds to the phase locking discussed in Section 5.5. Thus the combined n-th pulse can be derived as

$$^{out}\tilde{p}_n(t) = \sum_{m=0}^{N-1} \tilde{p}_{mn}(t) = A_0 \bullet \tilde{p}_S(t - n\Delta T) e^{i\omega_0 (t - n\Delta T + \phi_{0n})} \sum_{m=0}^{N-1} e^{im\frac{n}{N}2\pi}. \tag{5}$$

Since mathematically we have $\sum_{m=0}^{N-1} e^{im\frac{n}{N}2\pi} = 0$ if $\frac{n}{N}$ is not an integer, we get

$$\begin{cases} ^{out}\tilde{p}_n(t) = 0, & \text{when } \frac{n}{N} \text{ is not an integer} \\ ^{out}\tilde{p}_n(t) = NA_0 \bullet \tilde{p}_S(t - n\Delta T) e^{i\omega_0 (t - n\Delta T + \phi_{0n})}, & \text{when } \frac{n}{N} \text{ is an integer} \end{cases} \tag{6}$$

$$\begin{cases} ^{out}A_n = 0, \ ^{out}B_n = 0, & \text{when } \frac{n}{N} \text{ is not an integer} \\ ^{out}A_n = NA_0, \ ^{out}B_n = N^2 A_{0^2}, & \text{when } \frac{n}{N} \text{ is an integer} \end{cases}, \tag{7}$$

where $^{out}A_n$ is the amplitude of the combined n-th output pulse, and $^{out}B_n$ is the corresponding pulse energy coefficient of the combined n-th output pulse $^{out}B_n = \left|^{out}A_n\right|^2$. Thus a repetition-rate down-counting factor of N and a combined pulse energy enhancement factor of N^2 are shown.

5.4 Experimental demonstration of N^2 coherent combining

The system layout of the 2-channel N^2 coherent combining experiment is shown in Fig. 5.6. The system consists of a mode-locked laser, a grating stretcher, two parallel fiber amplifier channels, a FPI based combiner, and a grating compressor. It also contains the control electronics for coherent phasing of the parallel fiber amplifier channels, as well as cavity-length stabilization of the FPI combiner.

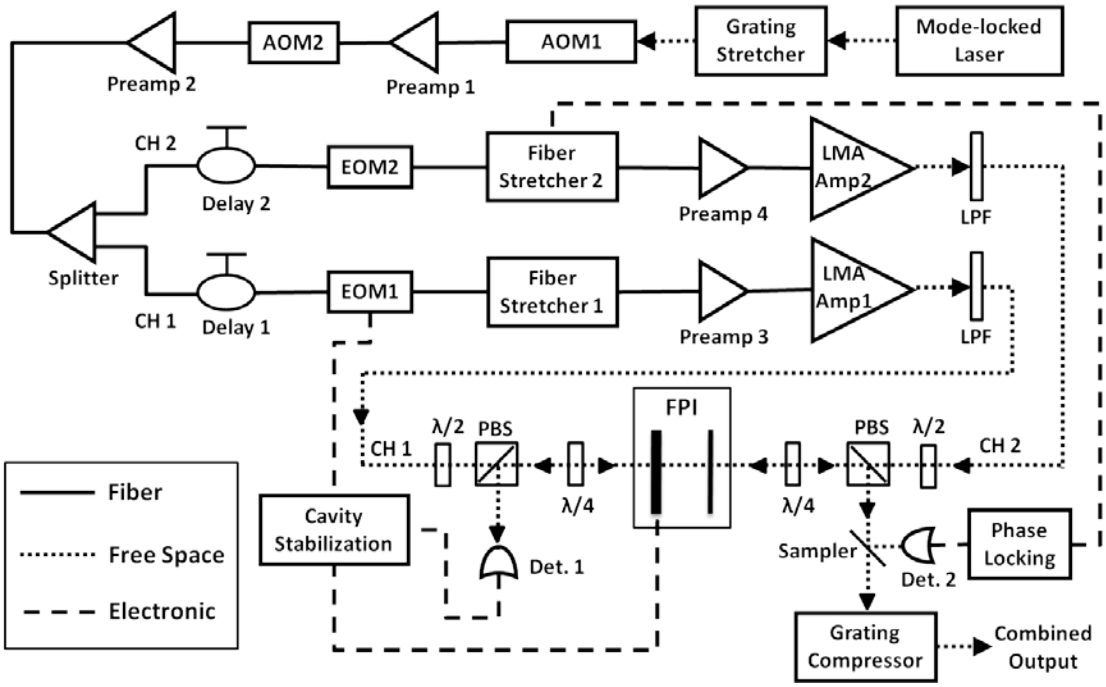

Fig. 5.6 Experimental N^2 coherent combining system. CH1/2: Channel 1/2; Preamp: pre-amplifier; LMA Amp.: large-mode-area fiber amplifier; LPF: long(wavelength)-pass filter; λ/2: half-wave plate; λ/4: quarter-wave plate; FPI: Fabry–Perot interferometer; Det.: detector.

The mode-locked laser operates at a central wavelength of 1059 nm, a repetition rate of 72 MHz, a spectral width of 12 nm, and an output power of 100mW. The diffraction-grating based pulse stretcher is arranged in a standard Martinez-type configuration, and it stretches output pulses from the mode-locked oscillator to a pulse width of ~900 ps. The stretched pulse sequence is then modulated by a free-space acousto-optic modulator

(AOM), so that the pulse repetition rate can be down-counted for achieving optimized fiber amplifier performances. The pulse sequence is afterwards coupled into polarization maintaining (PM) single-mode fiber (SMF), and amplified by two SMF pre-amplifiers before splitting into two parallel fiber amplifier channels. Amplification in each of the two SMF pre-amplifier stages is implemented using standard in-core pumped Yb-doped PM SMF and a standard telecom-grade single-mode pump diode. A monolithic AOM is inserted between the two pre-amplifiers, serving as an optical gate to suppress the unwanted amplified spontaneous emission (ASE) background between pulses. It also can be used to additionally down-count the pulse repetition rate for optimizing amplifier performances.

The pre-amplified pulse sequence is then split into two parallel fiber amplifier channels with a 50:50 single-mode fiber splitter. Parallel amplification channels consist of identical components with identical fiber lengths to ensure that each optical path is of equal length and with equal amount of linear and higher-order dispersion. In each parallel amplifier channel, the pulse sequence goes through a delay line, an electro-optic modulator (EOM), a fiber stretcher, a SMF pre-amplifier, and a large-mode-area (LMA) fiber amplifier before being coupled out. A compact precise adjustable delay line is used in each amplifier channel to achieve optical-path matching. The fiber-coupled electro-optic (EO) lithium niobate (LiNbO3) phase modulator EOM 1 in Channel 1 (CH1) is driven by the cavity-stabilization electronics to apply a frequency modulation to the CH1 pulse sequence, which is required for actively stabilizing the cavity length of the Fabry–Perot interferometer (FPI) combiner (discussed in Section 5.5). Meanwhile EOM 2 in Channel 2 (CH2) applies the required N^2 phase modulation/code to the CH2 pulse

sequence. The piezoelectric fiber stretcher based phase modulator in CH2 is used for correcting the phase drift between the two amplifier channels, which will be shown in Section 5.5. In each amplifier channel, the pulse sequence is further amplified by a SMF pre-amplifier and a subsequent co-pumped 25 μm large-mode-area (LMA) fiber amplifier. After the pulse sequence is coupled out from each amplifier channel, a long-pass filter (LPF) with its cutting-off wavelength tuned to 1045 nm is implemented to filter out the ASE background in the amplified signal.

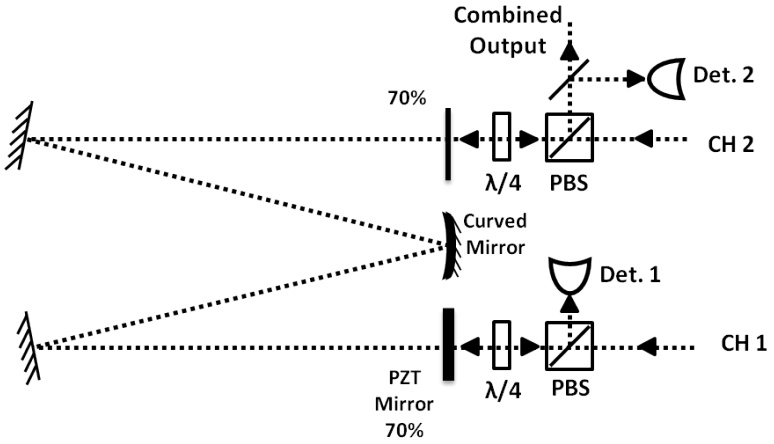

Fig. 5.7 The combiner part of the N^2 coherent combining setup. CH1/2: Channel 1/2; λ/2: half-wave plate; λ/4: quarter-wave plate; Det.: detector.

Fig. 5.7 shows the combiner part of the N^2 coherent combining setup, which includes a 5-mirror FPI cavity, two quarter waveplates, and two polarized beam splitters (PBS). The FPI cavity consists of two flat highly reflective mirrors (R=99.5%), a curved highly reflective mirror (R=99.5%), and two flat partially reflective cavity mirrors (R=70%). Here a curved mirror is implemented to make the FPI cavity q-preserving for better interferences at the partially reflective cavity mirrors. Two pulse sequences from CH1 and CH2 are incident to the FPI cavity from opposite sides of the cavity. A set of PBS and quarter waveplate is implemented on each side of the FPI cavity for beam guidance

while ensuring the same polarization for the two channels to interfere. The interference between the cavity transmission signal of CH1 and the cavity reflection signal of CH2 makes the combined output signal, and a small fraction of it is monitored by detector 2 for phase locking between the two channels. Meanwhile the output signal from the other side of the cavity is monitored by detector 1 for FPI cavity length stabilization. Both phase locking and cavity stabilization are required for N^2 coherent combining and will be discussed in Section 5.5. Finally the combined output pulse sequence is launched into a standard Treacy-type diffraction grating compressor.

5.5 System requirements for N^2 coherent combining

In this N^2 coherent combining experiment, the N^2 phase code is applied to the pulse sequence in CH2 through EOM2, so that every other pulse in the sequence is applied a π phase shift according to Eq. 2. In the frequency domain, this phase modulation shifts the frequency comb of the CH2 signal by half the repetition rate. Both the time domain and frequency domain pictures are shown in Fig. 5.8.

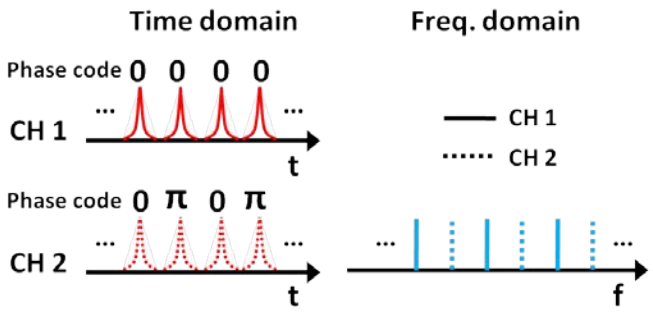

Fig. 5.8 The time domain and frequency domain pictures of the two input pulse sequences with the N^2 phase code.

From the discussion in Section 2.2, the FPI cavity length needs to be stabilized such that the free spectral range of the FPI cavity should be the same as the repetition rate of

the input pulse sequences, the transmission peaks of the FPI transfer function should be aligned with the frequency comb of the CH1 signal, and the rejection band centers should be aligned with the frequency comb of the CH2 signal. Here we develop a cavity stabilization scheme in the presence of both channel inputs, which is done by using Det. 1 to monitor the total average power signal ($\boldsymbol{S_{cs}}$) of the cavity transmission signal of CH2 and the cavity reflection signal of CH1. The simulation present in Fig. 5.9 shows the total average power signal $\boldsymbol{S_{cs}}$ on Det. 1 versus the frequency offset between the FPI transmission peaks and the frequency comb components of the pulse sequence in CH1, where the required cavity stabilization is achieved when the frequency offset vanishes. This is done by electronically minimizing the Det. 1 signal $\boldsymbol{S_{cs}}$, which in details is done by applying a ~2 MHz frequency modulation to EOM1, monitoring and demodulating the total average power signal $\boldsymbol{S_{cs}}$, and applying a proper feedback signal to drive the PZT cavity mirror after a series of signal processing.

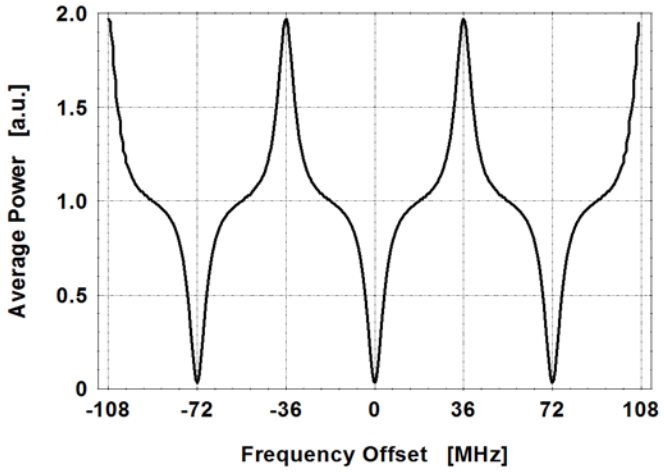

Fig. 5.9 The total average power signal Scs on Det. 1 versus the frequency offset between the FPI transmission peaks and the frequency comb components of the pulse sequence in CH1.

To achieve perfect interferences of the pulse sequences from different channels on the FPI cavity mirror, both group delay matching and pulse phase synchronization need to be satisfied. Accurate matching of the group delays between parallel channels is required so that the pulses are exactly overlapped in time when interfering. In practice, acceptable group-delay errors should be much smaller than the pulse duration, and for femtosecond pulses should be on the order of few micrometers. As shown in Fig. 5.7, the combining interferences happen on the non-PZT cavity mirror, thus the pulse sequences from CH1 and CH2 should travel the same optical path upon arrival at that mirror, which means prior to the FPI cavity CH2 should have an optical path which is longer than that of CH1 by a cavity single trip. Besides, the adjustable delay line in each channel is used to fine tune the optical path in micrometer precision to match the group delay of the two channels.

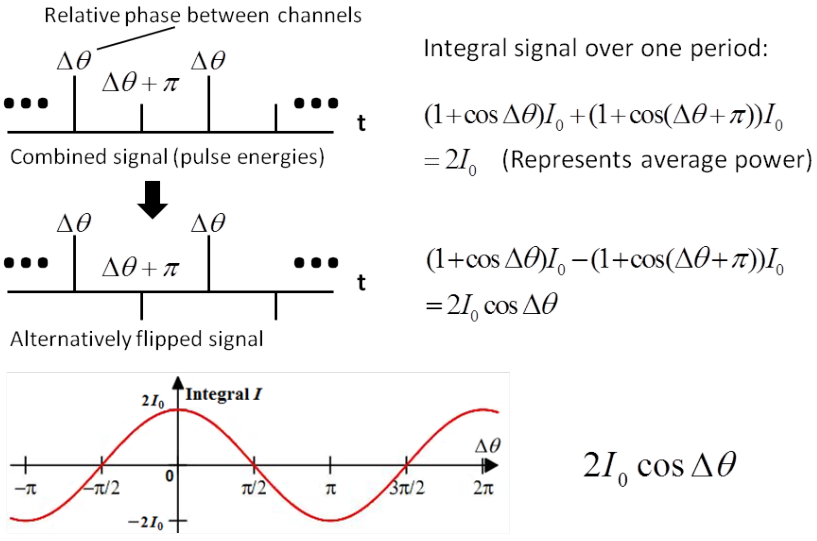

Fig. 5.10 Creating a phase-dependent integral signal for phase locking in N^2 coherent combining. Here I_0 is a constant integral value.

According to Eq. 4, to achieve N^2 coherent combining the carrier initial phases of all channels should be synchronized. For this 2-channel experiment, every other un-

modulated pulse in the CH2 pulse sequence should be in phase with the CH1 pulse upon interference. Unlike the case of phase locking in conventional coherent beam combining of short pulses [9], in this experiment the average power of the combined output signal does not depend on the relative phase between the two channels, which is shown in Fig. 5.10. Here we developed a phase locking scheme for N^2 coherent combining by electronically flipping every other combined pulse in the combined sequence by mixing it with a square wave whose frequency is half the repetition rate of the input pulse sequences, integrating the flipped combined pulse signal with a proper filter, thus creating a phase-dependent integral signal for phase locking. This process is shown in Fig. 5.10, where it is clear that the required phase locking can be achieved by maximizing the phase-dependent integral signal ***I***, which is done by applying a phase modulation to fiber stretcher 2, monitoring and demodulating the average power signal of a fraction of the combined output signal, and applying a proper feedback signal back to drive fiber stretcher 2 after a series of signal processing.

5.6 Experiment results and analysis

After the N^2 phase code is applied to the pulse sequence in CH2 (shown in Fig. 5.8) and the group delays of the two channels are matched, Det. 2 monitors the combined pulse sequence, as well as the FPI output for each individual input channel when the other channel is blocked, which are all shown in Fig. 5.11. Here the pulse sequences from individual channels are recorded without stabilizing the FPI cavity since in this experiment cavity stabilization is achieved with the presence of both channel inputs. Instead they are captured as their maximums received by Det. 2, since cavity stabilization maximizes those signals received by Det. 2. The combined pulse sequence is recorded

after the cavity is stabilized and the phases of the pulse sequences from the two channels are synchronized.

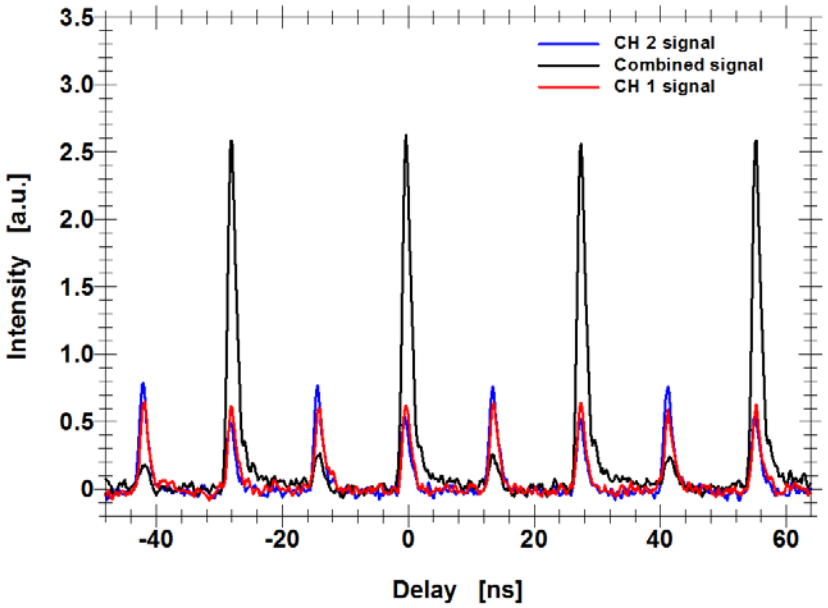

Fig. 5.11 The output coherently combined signal and the FPI output signal for each individual input channel (when the other channel is blocked).

From the data shown in Fig. 5.11, the pulse energy enhancement factor is measured to be ~ 3.5, which is defined as the peak power ratio between the combined pulses and the most intense pulses from individual channels. The combining contrast is measured to be 10.6 dB, which is defined as the peak power ratio between the combined pulses and the residual pulses in the combined pulse sequence. Here the pulse energy enhancement factor is smaller than theoretical 4, and the combining contrast is limited. The main contributing factor was the amplitude modulation in the FPI output signal for CH2, introduced by an imperfect N^2 phase modulation as well as an offset between the stabilized FPI transfer function and the input frequency comb.

Since cavity mirrors with a 70% reflectivity are used in this experiment, when the required cavity stabilization is achieved the FPI transmission for the CH1 pulse sequence

should be around 100%, while the FPI reflection for the CH2 pulse sequence should be around 97%. As a result, the absolute pulse energy enhancement factor, which is defined as the peak power ratio between the combined pulses and the most intense input pulses to the FPI combiner, should be around 97% of the measured pulse energy enhancement factor of 3.5, which is 3.4.

5.7 Summary

In this chapter we conceptually introduce and experimentally demonstrate N^2 coherent combining, a new multi-dimensional pulse multiplexing and beam combining technique based on resonant optical cavities, which can lead to orders of magnitude reduction in the coherently combined fiber amplifier array size for achieving very high energy (up to ~10 J) ultrashort pulses.

5.8 References

1. Strickland, D.; Mourou, G. Compression of amplified chirped optical pulses. *Opt. Commun.* **1985**, 55(6), 447-449.

2. Röser, F.; Eidam, T.; Rothhardt, J.; Schmidt, O.; Schimpf, D. N.; Limpert, J.; Tünnermann, A. Millijoule pulse energy high repetition rate femtosecond fiber chirped-pulse amplification system. *Opt. Lett.* **2007**, 32(24), 3495-3497.

3. Leemans, W.; Esarey, E. Laser-driven plasma-wave electron accelerators. *Phys. Today* **2009**, 62(3), 44-49.

4. Kienel, M.; Klenke, A.; Eidam, T.; Hädrich, S.; Limpert, J.; Tünnermann, A. Energy scaling of femtosecond amplifiers using actively controlled divided-pulse amplification. *Opt. Lett.* **2014**, 39(4), 1049-1052.

5. Zaouter, Y.; Guichard, F.; Daniault, L.; Hanna, M.; Morin, F.; Hönninger, C.; Mottay, E.; Druon, F.; Georges, P. Femtosecond fiber chirped-and divided-pulse amplification system. *Opt. Lett.* **2013**, 38(2), 106-108.

6. Jones, R. J.; Ye, J. Femtosecond pulse amplification by coherent addition in a passive optical cavity. *Opt. Lett.* **2002**, 27(20), 1848-1850.

7. Breitkopf, S.; Eidam, T.; Klenke, A.; von Grafenstein, L.; Carstens, H.; Holzberger, S.; ... Limpert, J. A concept for multiterawatt fibre lasers based on coherent pulse stacking in passive cavities. *Light: Science & Applications* **2014**, 3(10), e211.

8. Zhou, T.; Ruppe, J.; Zhu, C.; Hu, I.; Nees, J.; Galvanauskas, A. Coherent Pulse Stacking Amplification of Nanosecond and Femtosecond Pulses. In *Advanced Solid State Lasers (ASSL2014)*, Shanghai, China, 2014, pp. AW4A-7.

9. Siiman, L. A.; Chang, W. Z.; Zhou, T.; Galvanauskas, A. Coherent femtosecond pulse combining of multiple parallel chirped pulse fiber amplifiers. *Opt. Express* **2012**, 20(16), 18097-18116.

Chapter 6

Summary and discussions

This dissertation work is focused on coherent combining of ultrashort optical pulses from fiber amplifiers, to overcome the gap between current achievable fiber laser pulse energies (millijoule level) and required pulse energies for high energy industrial and scientific applications (up to tens of J). The combining of multiple amplified ultrashort pulses can be implemented in spatial, spectral, and time domains. This dissertation work consists of coherent beam combining in the spatial domain, coherent spectral combining in spatial and spectral domains, coherent pulse stacking amplification in the time domain, and N^2 coherent combining in spatial and time domains.

In the coherent beam combining work, we have demonstrated a multi-channel fiber femtosecond pulse combining system with 96.4%, 94.0%, and 93.9% relative combining efficiencies for two, three, and four channels respectively. The combined and compressed ~500fs pulses have identical shape to the compressed pulses from individual channels, indicating that pulse quality is preserved in a multi-channel pulse combining system. Furthermore, we established convenient experimental and theoretical metrics for characterizing combined system performance due to phase and amplitude errors in the parallel-channel array. It is based on a notion of relative combining efficiency, which can be experimentally determined using a straightforward measurement procedure. Inherent advantage of this “figure of merit” is that it directly relates to the efficiency of the

combined array, and can be easily calculated and measured. Although this metric was rigorously developed for a binary-tree type of combiner, it should be directly applicable to other types of beam combiners (e.g. holographic beam combiners). Our analysis of combining efficiency dependence on amplitude and phase errors shows that LOCSET feedback based combining systems should scale gracefully to very large numbers of channels. Although our interest here was primarily associated with ultrashort-pulse combining, these conclusions are of general nature and could be equally well applied to cw and pulsed systems. Of course, a full description of ultrashort-pulse combining scalability should also include consideration of pulse-dispersion effects. However, our experiment indicates if all the channels are identical these dispersion effects can be cancelled out, at least in the low-nonlinearity case. Coherent combining of femtosecond pulses in multi-channel parallel fiber CPA systems offers a possible path towards simultaneously generating high energy and high average power ultrashort laser pulses.

In the coherent spectral combining work, we have demonstrated coherent spectral combining of femtosecond optical pulses from multiple parallel fiber CPA channels. This technique enables ultrashort pulse amplification with an aggregate spectrum significantly exceeding amplification bandwidths of each individual amplifier, as well as allows scaling average power and pulse energy beyond single fiber limitations. Potentially, this technique could lead to fiber laser sources of tens of femtosecond duration multi-mJ pulses with high average powers. These experimental results show that, since coherent spectral combining of ultrashort pulses essentially constitutes a signal synthesis, combined-pulse temporal shape very strongly depends on individual-channel spectra. Generation of background-free pulses requires smooth combined spectrum, which can be

achieved using partially overlapping individual-channel spectra. Combining of separate, non-overlapping individual-channel spectra leads to significantly structured combined-pulse background. In addition, controlling the phase between the channels can be used to shape the temporal profile of the combined signal.

In the coherent pulse stacking amplification work, we have proposed and demonstrated a new technique of coherent pulse stacking (CPS) amplification to overcome limits on achievable energies of short optical pulses from optical amplifiers. We achieve CPS of amplified femtosecond and nanosecond pulses based on a single reflecting resonant cavity, with near-theoretical stacked peak-power enhancement factors of ~2.5 and high satellite-pulse contrast factors of ~16 dB. We experimentally demonstrate that this CPS technique is compatible with the chirped-pulse amplification (CPA) technique. We also show theoretically that large numbers of equal-amplitude pulses can be stacked using sequences of multiple reflecting resonators. Further work on cascading of multiple GTI cavities for attaining orders of magnitude higher peak-power enhancement factors is in progress. This CPS technique, when implementing together with CPA and coherent combining techniques, offers a potential path to achieving very high-energy pulses from ultrashort-pulse fiber-amplifier systems.

In the N^2 coherent combining work, we conceptually introduce and experimentally demonstrate N^2 coherent combining, a new multi-dimensional pulse multiplexing and beam combining technique based on resonant optical cavities. Its unique aspect is that in a N-channel system the combined pulse energy is enhanced by N^2 times while the combined average power is enhanced by N times. This technique can lead to orders of

magnitude reduction in the coherently combined fiber amplifier array size for achieving very high energy (up to ~10 J) ultrashort pulses.

Both the coherent pulse stacking amplification (CPSA) technique and the N^2 coherent combining technique achieve coherent pulse synthesis in the time domain using resonant optical cavities. It is important to note that the round-trip length of stacking cavities should match repetition period between the pulses that are being stacked, not the resulting "stacked" pulse train repetition period. This is due to causality constraint only requiring that pulse stacker response time cannot be shorter than temporal separation between adjacent pulses in the incident train. Therefore, when starting with a high repetition rate pulse train from a mode locked laser such stacking/combining cavities can be made very compact, particularly when using Herriott cell folding. At this point it is worth commenting that, while both presented techniques provide with useful avenues of increasing pulse energy per parallel amplification channel, it is the CPSA technique that is much better suited for significantly reducing fiber array size of extreme high pulse energy systems. Indeed, use of the N^2 technique is constrained by its applicability only to strictly periodic pulse trains. This leads to a certain trade-off, which can be highlighted by a particular example. Let's consider a 1 MHz repetition rate incident pulse train. The corresponding combiner round-trip length is 300 m. Let's assume that using Herriott cell this cavity can be folded hundreds times, into approximately 3 m long folded setup. This is feasible with existing state of the art dielectric mirror coatings. Implementation of N^2 scheme with 10 channels would reduce the repetition rate down to 100 kHz, and would increase pulse energy by 100 times. Assuming 1 mJ per pulse in the incident pulse train (1 kW average power) one would obtain 100 mJ per pulse in the combined beam, with

the corresponding average power at the output of 10 kW. Implementation of N^2 scheme with 100 channels would reduce the repetition rate down to 10 kHz, and would increase pulse energy by 10^4 times reaching up to 10J, with the total combined average power of 100 kW. However, this would be achieved at the expense of a rather complex and large beam combining/pulse stacking arrangement. In contrast, CPSA technique can be applied to equal-amplitude pulse bursts, where these bursts are produced at any arbitrary repetition rate (including a single shot operation). Consequentially, as it was shown earlier, a relatively small number of GTI-based pulse stackers (~10 - 15) is sufficient to achieve pulse stacking factors between 100 and 1000. Of course, in this case extractable pulse energy per channel is limited by the stored energy in a fiber, which for large-core state-of-the-art fibers reaches into 10mJ to 50mJ range. As a result of such high stacking factors it is possible to generate >10J pulses with array sizes as small as 100 to 1000 parallel channels, and with each individual pulse energy in a single-channel stacking burst <100 μJ, producing very low B-integral values and, therefore, negligible pulse distortions.

Appendix: List of publications on the dissertation work

Journal papers:

1. Tong Zhou, John Ruppe, Paul Stanfield, John Nees, Russell Wilcox, and Almantas Galvanauskas, "Resonant cavity based time-domain multiplexing techniques for coherently combined fiber laser systems," submitted to *European Physical Journal* (2015).

2. Tong Zhou, John Ruppe, Cheng Zhu, I-Ning Hu, John Nees, and Almantas Galvanauskas, "Coherent pulse stacking amplification using low-finesse Gires-Tournois interferometers," *Opt. Express* **23**, 7442-7462 (2015).

3. Wei-zung Chang, Tong Zhou, Leo A. Siiman, and Almantas Galvanauskas, "Femtosecond pulse spectral synthesis in coherently-spectrally combined multi-channel fiber chirped pulse amplifiers," *Opt. Express* **21**, 3897-3910 (2013).

4. *Leo A. Siiman, Wei-zung Chang, Tong Zhou, and Almantas Galvanauskas, "Coherent femtosecond pulse combining of multiple parallel chirped pulse fiber amplifiers," *Opt. Express* **20**, 18097-18116 (2012). (*All authors contributed equally to this paper.)

Conference papers:

1. Tong Zhou, John Ruppe, Cheng Zhu, I-Ning Hu, John Nees, Russell Wilcox, Wim Leemans, and Almantas Galvanauskas, "Coherent pulse stacking amplification using cascaded and multiplexed Gires-Tournois interferometers," accepted by *CLEO:2015*.

2. Tong Zhou, John Ruppe, Cheng Zhu, I-ning Hu, John Nees, Russell Wilcox, and Almantas Galvanauskas, "Coherent pulse stacking in fiber chirped-pulse amplification systems," in *SPIE Photonics West:2015*, paper 9344-46.

3. T. Zhou, J. Ruppe, C. Zhu, I. Hu, J. Nees, and A. Galvanauskas, "Coherent Pulse Stacking Amplification of Nanosecond and Femtosecond Pulses," in *Advanced Solid State Lasers*, (Optical Society of America, 2014), paper AW4A.7.

4. Tong Zhou, Cheng Zhu, John Ruppe, Paul Stanfield, John Nees, and Almantas Galvanauskas, "Coherent Pulse Stacking Amplification," *in the International Committee on Ultra-High Intensity Lasers:2014*.

5. W. Chang, T. Zhou, L. Siiman, and A. Galvanauskas, "Femtosecond pulse spectral synthesis using coherently combined multi-channel fiber chirped pulse amplifiers," in *CLEO:2012*, (Optical Society of America, 2012), paper CW1D.4.

6. W. Chang, T. Zhou, L. Siiman, and A. Galvanauskas, "Femtosecond pulse coherent combining and spectral synthesis using four parallel chirped pulse fiber amplifiers," in *Advanced Solid-State Photonics*, (Optical Society of America, 2012), paper AM4A.25.

7. Leo Siiman, Tong Zhou, Wei-Zung Chang, and Almantas Galvanauskas, "Active coherent combining of multiple parallel femtosecond-pulse CPA channels," in *SPIE Photonics West:2012*, paper 8237-39.

8. Tong Zhou, Leo Siiman, Wei-Zung Chang, and Almantas Galvanauskas, "Coherent Combination of fs Pulses from Fiber Amplifiers," *in the International Committee on Ultra-High Intensity Lasers:2012*.

9. L. Siiman, T. Zhou, W. Chang, and A. Galvanauskas, "Femtosecond pulses from coherently combined parallel chirped pulse fiber amplifiers," in *CLEO:2011* (Optical Society of America, 2011), paper CMD2.